A New Adiabatic Compressed Air Energy Storage System: Modeling, Design, Optimization, and Experiments

by

Shucheng Huang

A thesis
presented to the University of Waterloo
in fulfillment of the
thesis requirement for the degree of
Master of Applied Science
in
Mechanical and Mechatronics Engineering

Waterloo, Ontario, Canada, 2020

Author's declaration

I hereby declare that I am the sole author of this thesis. This is a true copy of the thesis, including any required final revisions, as accepted by my examiners.

I understand that my thesis may be made electronically available to the public.

Abstract

Wind farms and solar farms often face challenges in delivering consistent power output during peak demand due to the inconsistency of wind and solar resources. An adiabatic compressed air energy storage (ACAES) system based on the novel compression strategy is proposed to store and release energy when needed to reduce CO2 emission [1]. Compared to existing ACAES system designs, the main potential advantages of the proposed system are the reduced cost, space, and simplicity.

A prototype, originally developed for the air hybrid engine project at the University of Waterloo, was adopted for this project. Mathematical models were developed for the system under air compression (AC) and air motor (AM) mode. Simulations ran in GT-Suite yielded consistent results with mathematical models'. The previous prototype was thoroughly tested and evaluated. Design issues were addressed, and changes were incorporated into the new prototype design. The new experimental system models were developed in GT-Suite and evaluated through experimental analysis.

The ACAES system with a separate thermal energy storage (TES) was detailed. Specifically, a low-temperature ACAES was selected for practical reasons, and water was chosen as the heat transfer medium (HTM). Simulation results confirmed the TES system's ability to maintain high pressure (HP) tank temperature of 150°C. A mean value model was developed to predict engine brake power, and a throttle controller was used to regulate the engine brake power during the air expansion process.

Considering operational safety constraints and feasibility, system components were analyzed and optimized to improve the ACAES system roundtrip efficiency. Additionally, the genetic algorithm (GA) was used to optimize the valve timing, and simulation results showed that the optimized valve timing could improve the engine brake power by 13.38%. A comparison study was presented to analyze the roundtrip efficiency of the optimized ACAES system over the baseline system. It was observed that the AC/AM mode efficiency was improved by 108% and 70.3%, respectively.

Acknowledgements

First, I would like to thank my supervisor, Prof. Amir Khajepour for giving me the opportunity to work in the Mechatronics Vehicle Systems Lab (MVSL) and for his many hours of support and guidance throughout the project. Leading a very large research group, he also motivates and cares for every individual with genuine patience. Personally, the example he is setting goes beyond academia and his impact on me will last.

I want to acknowledge that without the design input and technical abilities of Jason Benninger, the project could not be what it is today. Jeff Graansma, thank you for all the hours you spent advising me during the design, testing, and troubleshooting phases of this project. I want to thank Timothy Er for setting up and testing the initial experimental system. I would also like to thank Martha Morales for the IT support and GT-Suite support team for their continuous technical support.

I want to thank my dear friends, Yanjun Huang, Yuecheng Li, Shiyi Yang, and my office friends Fernando Barrios, Yubiao Zhang, Lucas Botelho, Neel Bhatt, Yukun Lu, Ruihe Zhang and Chao Yu for their support and assistance to my research. Furthermore, I would like to thank all other friends and colleagues in the MVSL and the University of Waterloo.

Finally, I would like to thank my parents, Zhenzhong Huang and Jianhong Yao, who offered me unconditional support and encouraged me through the challenging days and weeks to get me to the end of this project.

Shucheng Huang
Waterloo, Canada
August 31, 2020

Table of Contents

List of Figures

List of Tables

Abbreviations

AC Air compressor

ACAES Adiabatic compressed air energy storage

AM Air motor

APE Air powered engine

ASMC Adaptive sliding mode controller

BDC Bottom dead centre

CA Crank angle

CAD Computer-aided design

CAES Compressed air energy storage

CAS Compressed air storage

CB Compression braking

CFD Computational fluid dynamics

CY Cylinder

DCAES Diabatic compressed air energy storage

Dyno Dynamometer

EPA Environmental protection agency

FMEP Frictional mean effective pressure

GA Genetic algorithm

GUI Graphical user interface

HP High pressure tank

HTM Heat transfer medium

HVVA Hydraulic variable valve actuation

IC Intercooler

ICAES Isothermal compressed air energy storage

ICE Internal combustion engine

IMEP Indicated mean effective pressure

LP Low pressure tank

MVM Mean value model

MVSL Mechatronics vehicle systems lab

NTU Number of heat transfer units

OEM Original equipment manufacturer

PHES Pumped hydroelectric energy storage

PLC Programmable logic controller

PTFE Polytetrafluoroethylene or Teflon

SMC Sliding mode controller

TDC Top dead centre

TES Thermal energy storage

VVT Variable valve timing

List of Symbols

a Connecting rod length [m]

A_{cyl} Cylinder exposed area [m^2]

A_T Throat area [m^2]

$\eta_{Elect\_to\_Ex}$ AC mode efficiency

$\eta_{Ex\_to\_Elect}$ AM mode efficiency

B Cylinder bore [m]

c_{cy} Speed of sound in cylinder [m/s]

c_{hp} Speed of sound in cylinder [m/s]

C_D Discharge coefficient

c_{hp} Speed of sound in HP tank [m/s]

$C_{in,i}/C_{out,i}$ Control volume inlet/outlet flow velocity [m/s]

$\dot{m}_{choked}$ Choked flow mass flow rate [kg/s]

$C_{p,cy}$ Specific heat of air under constant pressure [$J/kg \cdot K$]

$\frac{dE_{cv}}{dt}$ Rate of change of the total energy of the control volume [J/s]

η Mean value model efficiency

g Gravitational acceleration [m/s^2]

γ Heat capacity ratio

h_c Convective heat transfer coefficient $[W/m^2 \cdot K]$

$h_{in,i}/h_{out,i}$ Control volume inlet/outlet specific enthalpy [J/kg]

k Thermal conductivity $[W/m \cdot K]$

m Woschni correlative model exponent

M Molar mass [kg/mol]

$\dot{m}_{eng}$ Engine mass flow rate [kg/s]

$\dot{m}_{in,i}/\dot{m}_{out,i}$ Control volume inlet/outlet mass flow rate [kg/s]

$\dot{m}_{cy \to env}$ Mass flow rate from cylinder to environment [kg/s]

$\dot{m}_{hp \to cy}$ Mass flow rate from HP tank to cylinder [kg/s]

μ Dynamic viscosity $[N \cdot s/m^2]$

N Number of moles [mol]

Nu Nusselt number

ω Crankshaft rotational speed [Rad/s]

P_0 Orifice or upstream absolute pressure [Pa]

P_{brake} Engine brake power [W]

$\mathrm{P}_{cyl,peak}$ Peak cylinder pressure [bar]

P_{fric} Engine friction power [W]

P_{in} Cylinder inlet air pressure [Pa]

$P_{indicated}$ Engine indicated power [W]

P_{out} Cylinder outlet air pressure [Pa]

P_T Throat or downstream absolute pressure [Pa]

$\dot{Q}$ Heat generation rate [J/s]

R Ideal gas constant $[N \cdot m/mol \cdot K]$

Re Reynolds number

ρ Density $[kg/m^3]$

ρ_0 Orifice or upstream air density $[kg/m^3]$

$\overline{S}_p$ Mean piston speed [m/s]

$\dot{m}_{sub-critical}$ Sub-critical flow mass flow rate [kg/s]

T Temperature [k]

T_{inlet} Inlet air temperature [K]

$\frac{dT_{cy}}{dt}$ Rate of change of cylinder temperature [k/s]

θ Crank angle [deg]

$\frac{dT_{tank}}{dt}$ Rate of change of tank temperature [k/s]

$\frac{dU_{cy}}{dt}$ Rate of change of the internal energy of the control volume [J/s]

V Volume $[m^3]$

V_c Cylinder clearance volume $[m^3]$

V_{cyl} Cylinder volume $[m^3]$

$\dot{V}_{cyl}$ Rate of change of cylinder volume $[m^3/s]$

$z_{in,i}/z_{out,i}$ Control volume inlet/outlet elevation [m]

Chapter 1

Introduction

1.1 Motivation and Objectives

One of the major problems with wind farms is the inconsistency of the wind in producing electricity. Wind farms often restrict the electricity generation during hours of strong wind due to constraints of the power grid [8]. In order to operate wind farms at maximum capacity, it is essential to implement an energy storage system such that the excess electrical energy can be stored and recovered later when needed [9].

A compressed air energy storage (CAES) uses a compressor to generate high-pressure air, stores it in a tank and regenerates power by feeding compressed air into a turbine. The CAES is standing out due to its low environmental impact, low installed capital cost, and high reliability [10]. As a variation of CAES, the adiabatic CAES (ACAES) is attracting more attention from researchers due to its improved thermal efficiency. Essentially, the ACAES adopts a thermal energy storage (TES) system, which stores the thermal energy during the compression process and uses it to reheat the air during the expansion process. Compared to conventional CAES, ACAES shows higher efficiency and zero CO2 emission [11].

According to the literature, implementing an ACAES system into wind or solar farms results in higher overall energy storage efficiency, system flexibility, and more financial return. The ACAES plants can operate on electricity spot markets by storing energy when electricity prices are low and producing electricity when prices are high [12].

This project aims to model, design, and optimize a new ACAES system based on the novel double-tank compression strategy and the rotary valve design [1]. The following tasks have been conducted to meet the objective above:

- Model and simulate the air compression and expansion process, and compare to the simulation results from GT-Suite
- Verify the GT-Suite models through experimental analysis
- Design the ACAES system with a separate TES system
- Evaluate and optimize the cycle efficiency based on system constraints

1.2 Thesis Outline

The main objective of this project was to model, design and optimize the ACAES system. This thesis gives the background of the ACAES project, models the ACAES system in MATLAB/Simulink, validates the models experimentally, details the designs of the ACAES system, and presents the results from analysis and optimization. The thesis is divided into seven chapters. The first chapter gives the motivation for this research and the outline of the thesis. The remaining chapters are organized as follows:

Chapter 2 Literature Review and Background

In Chapter 2, the ACAES system background information and existing designs are presented. Additionally, the operating principles of the air hybrid as well as the design of the rotary valve proposed by previous grad students are detailed.

Chapter 3 ACAES Modeling and Simulations

Chapter 3 discusses the layout of the ACAES system. Mathematical modeling of the air compression and expansion process are presented. The models are evaluated using GT-Suite simulation results. The experimental system is modeled in GT-Suite. Specifically, a CFD analysis is used to convert the non-standard rotary valve to a model in GT-Suite.

Chapter 4 Experimental Studies

This chapter discusses the evaluation of the previous prototype and the design of a new prototype. The experimental setup is detailed, which includes the mechanical, electrical system and the development of software for data acquisition and condition monitoring. The experimental GT-Suite models developed in Chapter 3 are validated to be used for further analysis and optimization.

Chapter 5 ACAES System Design and Brake Power Control

The detailed design of the ACAES system with a separate TES system is included in Chapter 5. A mean value model is developed to predict the engine cranktrain brake power. A throttle controller based on the PID control and lookup table is added into the mean value model to achieve brake power control.

Chapter 6 Analysis and Optimization

Chapter 6 presents the analysis and optimization. The air compression and expansion process are analyzed and optimized separately. Genetic algorithms are used to optimize the rotary valve timings. Simulations are run to evaluate the TES system design under both modes. Finally, a comparison study of the baseline system and the optimized ACAES system is presented.

Chapter 7 Conclusions and Future Work

This chapter concludes the work presented in the previous chapters and directs potential future work and directions.

Chapter 2

Literature Review and Background

This chapter establishes a review on ACAES system concept, design, modeling, and optimization. The CAES concept and its variations are firstly introduced in Section 2.1. Then, Section 2.2 discusses the ACAES system classification and designs. In Section 2.3, TES system concept and designs are presented. Follow on this, ACAES system modeling, evaluation and optimization are summarized in Sections 2.4 and 2.5. Finally, Section 2.6 provides the necessary background and related work from previous graduate students.

2.1 General Concept of CAES

CAES is a low-cost technology to store excess electrical energy in the form of compressed air. Compared to other energy storage technologies such as battery storage, ultracapacitor storage, CAES has low capital cost, low environmental impact, high reliability, and is capable of delivering utility-scale power output [10,13]. When compared to pumped hydroelectric energy storage (PHES), CAES technology doesn't rely on large elevation difference nor water reservoir making it suitable for remote dry areas with flat terrain [14].

The concept of CAES is straightforward. Ambient air is compressed and stored in air reservoir/compressed air storage (CAS). When electricity needs to be generated, pressurized air enters the expansion turbine to release energy.

The first operational CAES plant was built in Huntorf, Germany, and it was designed to deliver rated output for two or three hours [15]. Later, due to the rising interest in renewable energy, the Huntorf plant shifted to help balancing the rapidly growing wind output from North Germany [16]. More recent researches examined combining renewable energy plant with CAES technologies [10, 17, 18].

According to the current literature, the CAES can be categorized into three types based on thermal energy management, namely the adiabatic, diabatic, and isothermal [19]. In diabatic CAES (DCAES) or conventional CAES, the heat generated during the compression process is discharged to the ambient environment. Therefore, to avoid icing of the expander machinery caused by large airflow, natural gas is burned to pre-heat the air before the expansion process [2]. The isothermal CAES (ICAES) intends to generate high-pressure compressed air while keeping a constant air temperature during the compression process. Despite some research efforts [20–22], standard devices cannot achieve/approximate isothermal compression/expansion process. The adiabatic CAES (ACAES) adopts heat exchangers and a thermal energy storage (TES) system to store thermal energy during the compression process and reuse it to pre-heat the compressed air before the expansion process. Compared to DCAES, ACAES has zero direct CO_2 emission and can be optimized to achieve higher efficiency. Compared to ICAES, ACAES is more feasible and capable of storing more energy at a higher temperature. The simplified ACAES plant under charging and discharging mode is shown in Figure 2.1.

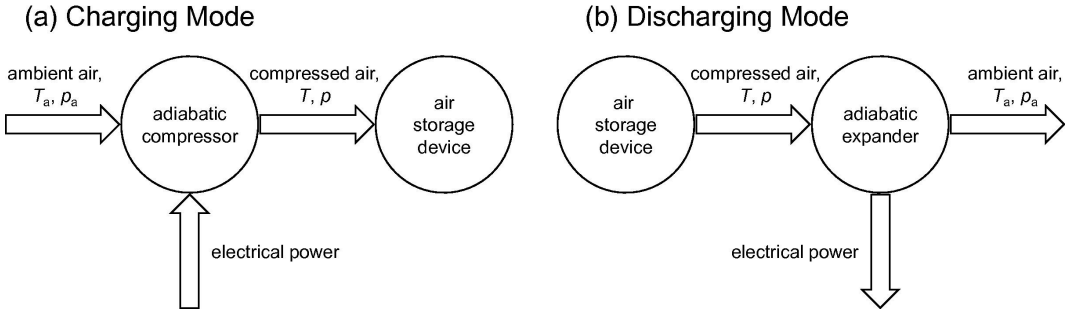

Figure 2.1: Simplified system of (a) charging and (b) discharging mode of an ACAES plant [2]

2.2 ACAES Classification and Designs

2.2.1 Classification

The ACAES system can be classified depending on the final air storage temperature. For the high-temperature process (air storage temperature is above 400°C), the desired air storage temperature requires a very high compressor outlet temperature. In general, this is technically feasible, but a lot of effort is needed to engineer the electrically driven compressor. For example, a high-temperature ACAES plant with compressor discharge

temperature ranging from 700 to 1500°F was studied by Biasi in [23]. A compressor discharge temperature of 371.111-815.55°C means that a significant amount of cooling and heat loss protection must be placed to avoid energy loss due to a large thermal gradient.

For medium temperature process (air storage temperature is between 200 to 400°C), the off-the-shelf compressor and TES media like molten salt or thermal oil can be utilized. In a medium-temperature ACAES plant, as shown in Figure 2.2, compression process consists of three compressors and two TES devices. The expansion stage consists of two turbines, and air enters the TES twice in order to obtain higher efficiency [2, 24].

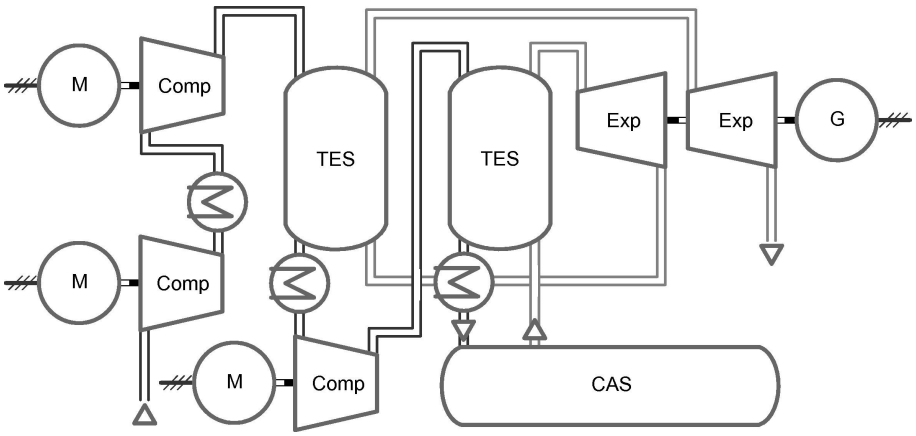

Figure 2.2: Layout of a medium-temperature ACAES plant [2]

Finally, for the low-temperature process (air storage temperature is below 200°C), the main advantages are the applicability of pumpable liquid HTM and standard heat exchangers as well as off-the-shelf compression and expansion devices [2]. The low-temperature plant layout is shown in Figure 2.3. In total, there are five compression and expansion stages with heat exchangers connected between them. The system contains two TES devices for cold HTM and hot HTM. During the compression stage, the liquid stored in the cold TES tank is pumped through the heat exchangers to cool the air. At the end of the compression stage, the liquid with heat extracted is stored in the hot TES tank. During the expansion stage, the liquid stored in the hot TES tank is pumped through the heat exchangers to preheat the air.

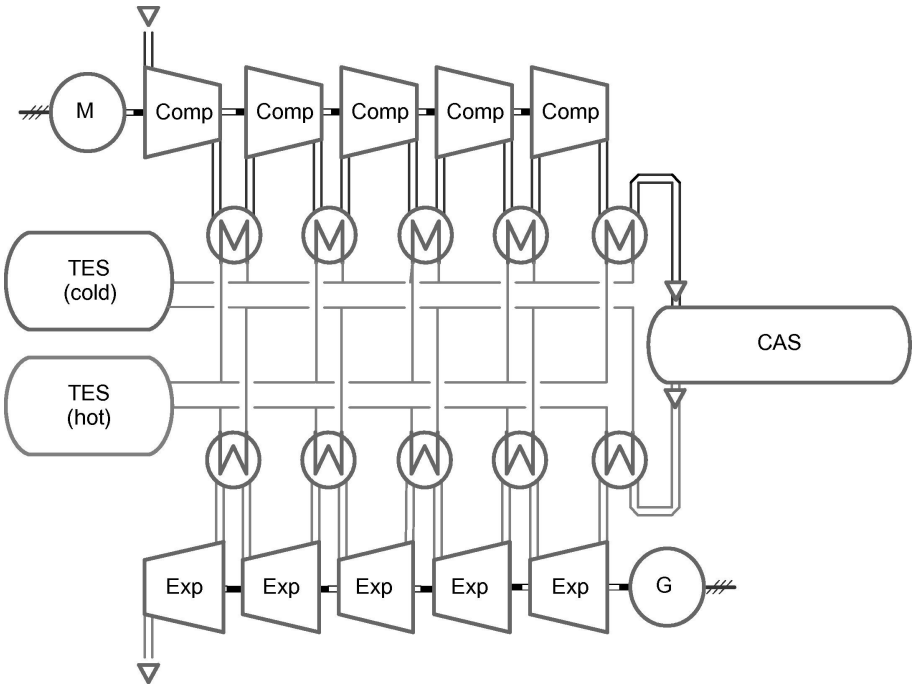

Figure 2.3: Layout of a low-temperature ACAES plant [3]

2.2.2 Low-temperature ACAES Design/ Prototype

There are many low-temperature ACAES designs or proposals available. Two selected designs are reviewed here.

TICC-500

TICC-500 is a 500-kW non-supplementary fired CAES or ACAES demonstration system [25, 26]. This system can be classified as a low-temperature ACAES system since the final compressor outlet temperature is 117°C. The compression stage consists of five compressors with heat exchangers connected between them. The air storage devices are two steel 50 m^3 tanks manufactured with phase change material, making the air storage process near-isothermal or isothermal. The air storage pressure is 1450.4 psi,a. The expansion process consists of three turbines with an expansion ratio of ∼3 connected in series. The air enters the first turbine at 450 psi,a and 100 °C. The exhaust air from the first turbine drops to 11.68°C. The cold air enters the heat exchanger and heats up to 100 °C before entering

the next turbine. The exhaust air from the last turbine is discharged into the atmosphere. The overall E-E efficiency of TICC-500 is 41.03%.

LTA-CAES

The overall structure of the LTA-CAES is similar to what is shown in Figure 2.3. However, in LTA-CAES, there are ten radial turbocompressors in total with intercoolers (IC) and main heat exchangers connected between them [27]. The compressor outlet temperature is limited to 200°C, and the air storage temperature is designed at 150°C. Water is selected as the TES medium, and water is compressed once the water temperature is above 95°C. The overall cycle efficiency (AC-AC) of LTACAES is in the range of 52-60%. One of the main advantages of LTACAES is the fast plant start-up within five minutes.

2.3 Thermal Energy Storage Design

The Thermal Energy Storage (TES) system can be classified into active/passive, direct/indirect storage system. For an active TES system, convection heat transfer is forced to bring the heat into the storage material. For a passive TES system, the storage medium is not circulated, and a heat transfer medium (HTM) is used to bring heat into or out of the storage material. The direct storage system means that the heat is directly stored in the HTM while the heat is stored in a secondary storage material for the indirect storage system [28].

For the passive storage system, the heat transfer is relatively low since there is no direct contact between the storage medium and HTM as the heat is transferred using a heat exchanger. An active indirect storage system typically uses oil as the heat storage material, and the oil temperature can reach 307°C, which leads to difficulties in sealing and leakage prevention [29, 30]. For the active direct system, there exists a single-tank system configuration as well as a two-tank system configuration.

The single-tank system stores the hot and cold HTM in the same storage device. Due to stratification, the hot HTM rises to the top while the cold HTM stays on the bottom. Based on this idea, during the heat storage process, cold HTM leaves the storage device from the bottom and enters from the top to bring the heat into the storage device. During the heat extraction process, hot HTM leaves the storage device and brings heat into the system.

The two-tank system stores the hot and cold HTM in two separate storage devices. During the heat storage process, cold HTM enters the system to carry out excessive heat

and stores it in the hot HTM storage. During the heat extraction process, the hot HTM in the hot HTM storage enters the system to extract the heat and returns to the cold HTM storage device. Compared to the single-tank system, the two-tank system has the disadvantages of the high cost of the extra tank and connecting pipelines; extra cost for the HTM (No circulation of HTM in double-tank system configuration); large space needed to host the extra facilities; and small temperature difference between the hot and cold fluid in the storage system.

2.4 ACAES Modeling

In general, modeling the ACAES system is done by separating the overall system into components. For compressors and turbines, some researchers modeled the compressor and turbine as a polytropic/isentropic compression/expansion process and calculated the power input/output based on the mass flow rate, pressure ratio as well as the polytropic efficiency [31, 32]. Transient models were used to model the air compressor and turbine in [25].

For the heat exchanger modeling, a constant heat exchanger efficiency of 0.95 was used in [32]. Since the heat exchanger performance is governed by the inlet mass flow rate, pressure, and temperature of the air and HTM, the number of heat transfer units (NTU) method was used in [33] to take into account these effects.

2.5 ACAES Evaluation and Optimization

Evaluation

According to the current literature, the ACAES system drive cycle analysis often assumes constant compressor and expander power [31,33,34], which is reasonable for the large-scale system. To evaluate the exergy destruction associated with compression or expansion, the change of exergy in an open system was used in [34]. By further neglecting the change of potential and kinetic energy, the formula to calculate the exergy destruction was presented.

There exists many expression to evaluate the ACAES system efficiency, which leads to difficulties when comparing the overall efficiency of ACAES systems with different layouts and parameters. Therefore, many researchers adopted the definition of E-E efficiency (also called the cycle or round-trip efficiency), which is the ratio of electricity generated over the sum of input energy [25, 34].

Optimization

Since the ACAES system cycle efficiency is governed by the compressor, turbine, and TES performance, the research of optimization of the ACAES system efficiency primarily focuses on the ACAES system structure and material design of the TES, air tank, and heat transfer fluid [35–38].

Guo et al. [39] added an ejector into the ACAES system. An ejector is a nozzle, and high-pressure air is accelerated into the contractible nozzle to obtain higher exit velocity and lower out pressure. The effect of the ejector was evaluated by comparing two ACAES systems. In the first system, the air pressure was reduced directly from 6.4 MPa to 2.5 Mpa. For the second system, the air pressure was reduced to 5 MPa and was later adjusted using the ejector to obtain higher flow velocity. A TES system was used to heat up the air before the expansion process. From the comparison study, it was concluded that the ejector improved the energy conversion efficiency by 3.41% (from 65.36% to 61.95%)

2.6 ACAES Project Background

This project benefited from concepts and designs proposed or made by previous graduate students in MVSL. Brief background and related work are introduced in the following sections.

2.6.1 Air Hybrid

An air hybrid vehicle is a vehicle with the modified engine, intake/exhaust manifolds, and valve train to work as an air compressor (AC) and air motor (AM). AC mode is activated when the vehicle is braking, and the modified engine behaves like an air compressor. In this mode, the vehicle's kinetic energy is converted into pressurized air stored in the air reservoir. In AM mode, the modified engine behaves like an air propulsion system, and the pressurized air enters the cylinder and pushes the piston down during the first subsequent acceleration [40, 41]. Through the AC and AM mode, an air hybrid vehicle can regenerate kinetic energy lost during braking known as regenerative braking (RB).

Some researchers adopted the air hybrid concept and extended it further [42,43]. Specifically, Andersson et al. added a second air tank to the system in order to achieve higher indicated mean effective pressure (IMEP) [42]. Based on GT-power simulation results, they claimed that they achieved 55% regenerative efficiency and a 23% reduction in fuel consumption. Liu et al. [43] replaced the conventional cam with a new rotary intake/exhaust

system. Based on their experimental results, they reported that the rotary system achieved higher efficiency under low rotational speed and higher maximum torque compared to the cam-based intake/exhaust system.

Other researchers focused on modeling and control of the air propulsion system [44–46]. Hung et al. [44] developed a real-time model for the light-duty automotive air propulsion system. The system model was simulated and validated experimentally. Xu et al. [45] developed a complete dynamic model of the air-powered engine (APE) to predict temperature drops during the operation. Based on their experimental results, their model was able to accurately predict the intake air temperature and exhaust air temperature. Then, they proposed the practical APE system and the corresponding heat exchanger system. Shen and Hwang [46] built a prototype air-powered motorcycle with a vane-type air motor. Using a fuzzy logic with PI (proportional integral) controller, they concluded that the speed error is within 1 km/h, and the efficiency is about 70% when the speed is over 20 km/h.

In order to achieve higher efficiency, Andersson optimized the valve timing to maximize air mass flow from LP to HP tanks in AC mode and minimize airflow from HP to LP tank in AM mode [42]. Li et al. [47] presented the optimal trade-off between system efficiency and power, given the heat transfer capability and ambient temperature. Their later work [48] presented the optimal pressure-volume trajectories. By employing the optimized trajectories for the simple case, 5-15 times power gains were predicted over sinusoidal and linear trajectories at 90% efficiency.

2.6.2 Novel Air Hybrid Engine

Fazeli proposed the novel air hybrid engine and laid the foundation for this project [1]. His work is summarized in the following sections.

Double-tank Compression Strategy

Fazeli proposed the double-tank compression strategy as shown in Figure 2.4.

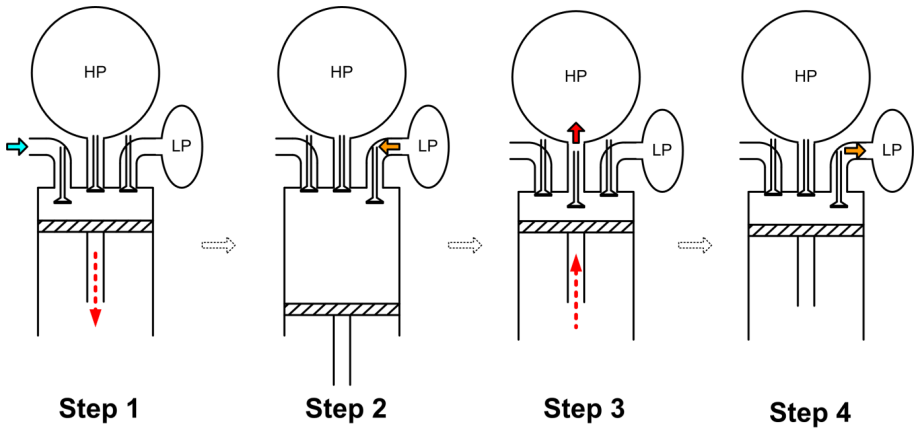

Figure 2.4: Fazeli's double-tank compression strategy [4]

The double-tank compression strategy for each cycle can be separated into four steps:
Step 1: After TDC, the piston goes down and atmosphere air enters the cylinder.
Step 2: Near BDC, the pressurized air from the LP tank enters the cylinder.
Step 3: The piston goes up and air in the cylinder gets compressed and enters the HP tank. The flow into HP tank stops near TDC.
Step 4: Near or after TDC, the airflow from cylinder to HP tank stops, and the remaining pressurized air enters the LP tank. The airflow from cylinder to LP tank stops when the piston goes down, and the cylinder pressure starts dropping.

To verify his proposal, he modeled the single-tank and double-tank compression strategy using mathematical models and GT-power. Based on the simulation results, he concluded that the final temperatures using both approaches were in the same range but the final pressures were significantly different, meaning that the double-tank compression strategy was capable of storing twice as much energy as the single-tank system.

Proposed Valve Timing

Based on the double-tank compression strategy and cam-based valve train, Fazeli provided the system layout and corresponding valve timing for the AC and AM mode, as shown in Figure 2.5, 2.6 and Table 2.1. The check valves were used to block backflow while the three-way solenoid valves were used to switch between AC and AM mode.

Under AC mode, as mentioned before, the main tank served as the HP tank to store compressed air while the auxiliary tank served as the LP tank. Under AM mode, the system behaves as an expander and the main tank serves as the pressurized air supply.

The high pressure air enters the cylinder near TDC and pushes the piston down in order to generate power. The air is then expelled through the intake manifold to avoid cooling down the exhaust after treatment system.

In Table 2.1, there is no flow throw solenoid valve 3 and 4 in AM mode due to the presence of check valves, shown in Figure 2.6.

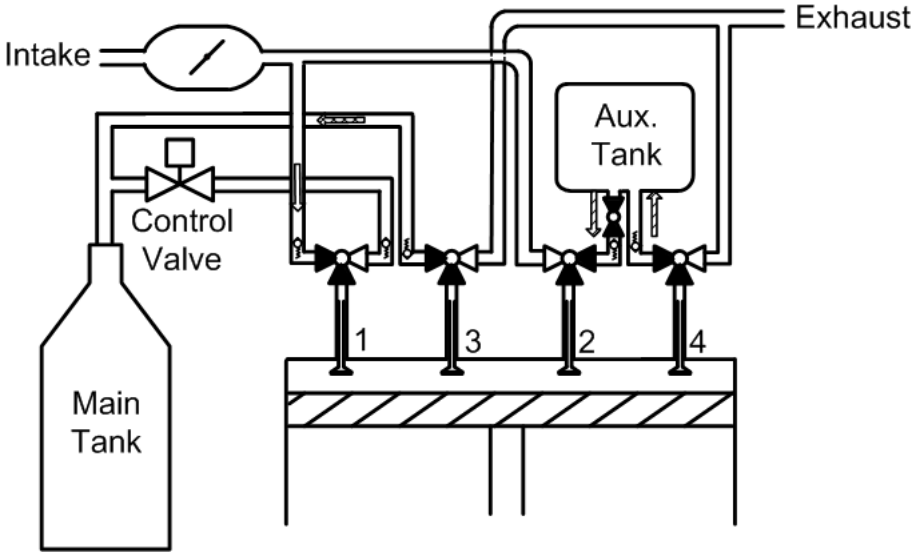

Figure 2.5: System layout in AC mode [4]

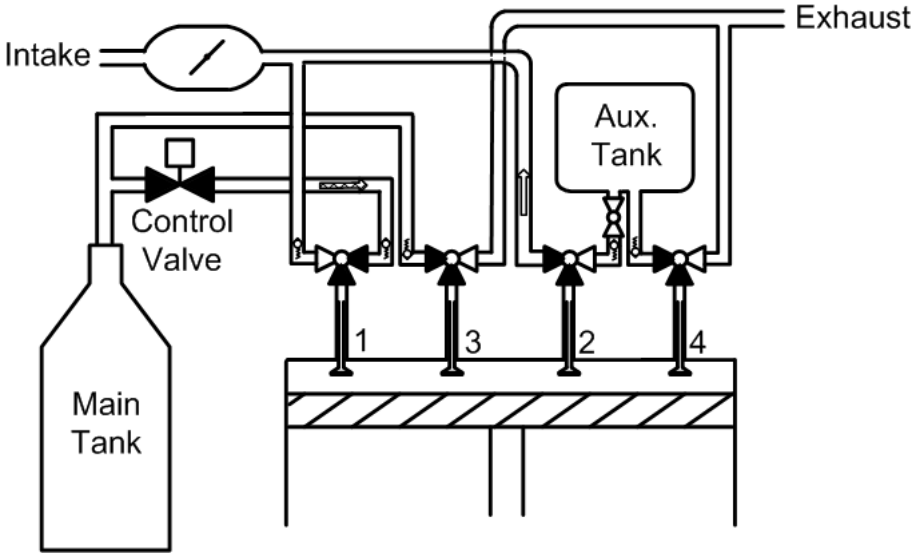

Figure 2.6: System layout under AM mode [4]

Table 2.1: Valve timings under AC and AM mode [4]

Solenoid Valve	Operating Angle [CAD]	Operating Angle [CAD]
	AC	AM
1	0-180 °	0-180 °
2	180-350 °	180-360 °
3	180-350 °	No flow
4	350-170 °	No flow

Experimental Setup

Since the switchable cam-based valve train was not available, Fazeli utilized high speed solenoid valves to represent the cam-based valve train timings, shown in Figure 2.7.

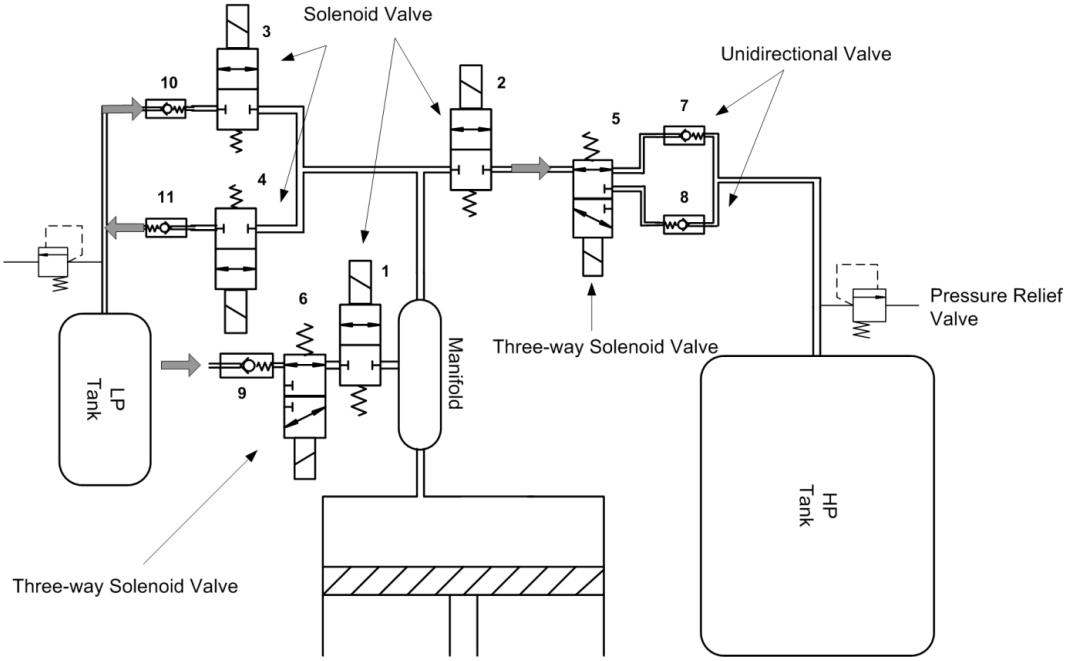

Figure 2.7: Fazeli's experimental setup [4]

Based on the HP tank pressure obtained from the air compression experiment, Fazeli concluded that the double-tank compression strategy improved 55% in storing pressure and 87% in energy storage capacity when compared to the single-tank compression strategy at an engine speed of 82 RPM. The experimental result of the air motor mode indicated 19% efficiency based on the exergy analysis.

2.6.3 Rotary Valve

Poumazeri's Work

The initial rotary valve concept was proposed by Poumazeri in his hydraulic variable valve actuation (HVVA) system project [5]. The concept was designed to eliminate the camshaft from an internal combustion engine (ICE) and replace it with a fully flexible hydraulic system.

His design, as shown in Figure 2.8, consists of the rotary spool and the valve ports. When the valve port is aligned with the port on the rotary spool, the valve is open and hydraulic fluid can flow. Pournazaeri provided detailed expression for the flow opening area

and utilized an orifice model to determine the flow rate through the rotary spool valve. In addition, his mathematical model gave initial sizes for his prototype, and his spool valve leakage calculations were used to size the clearance between the spool valve and the spool valve casing [49].

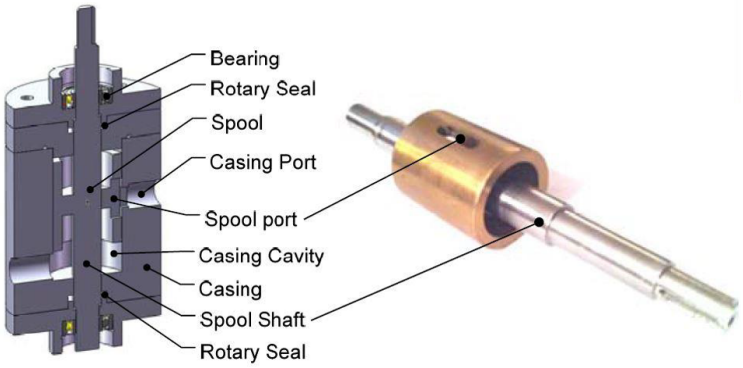

Figure 2.8: Pournazeri's spool valve [5]

Chermesnok's Work

Chermesnok extended Pournazeri's prototype to work with multiple cylinders [6]. He added ports to a hollow spool shaft to feed multiple engine cylinders as shown in Figure 2.9. The input ports were connected to the high pressure supply line and the reservoir. By attaching this spool shaft to the spool valve housing, shown in Figure 2.10, this design laid the foundation for the rotary valve designed by Soheli and the one used in current project.

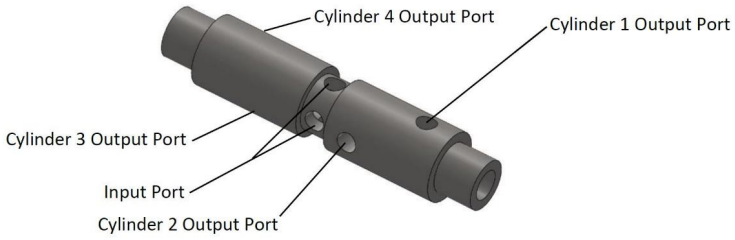

Figure 2.9: Multi cylinder spool shaft design [6]

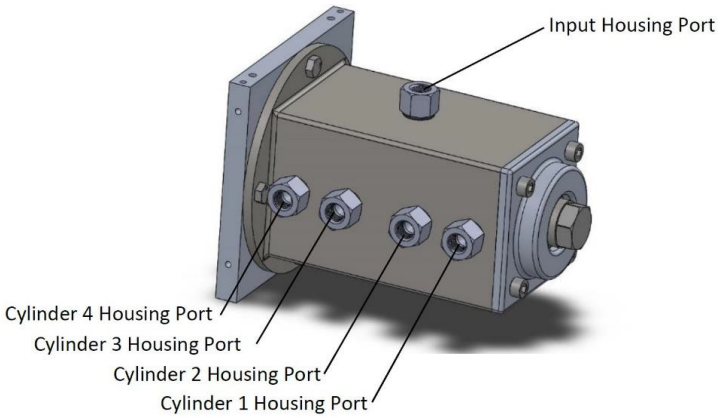

Figure 2.10: Chermesnok's spool valve housing [6]

Soheli's Work

Soheli adopted Chermesnok's concept and modified it for the novel air hybrid engine system project. Instead of using solenoid valves, all the valve timings were directly controlled by the rotary valve attached to the cylinder head, as shown in Figure 2.11. Once the rotary valve port is aligned with the port on the cylinder head, the valve is open and air can flow through the valve. Soheli designed the rotary valve as a hollow shaft such that air flows could enter or exit the cylinder through the hole on the bottom of the cylinder head.

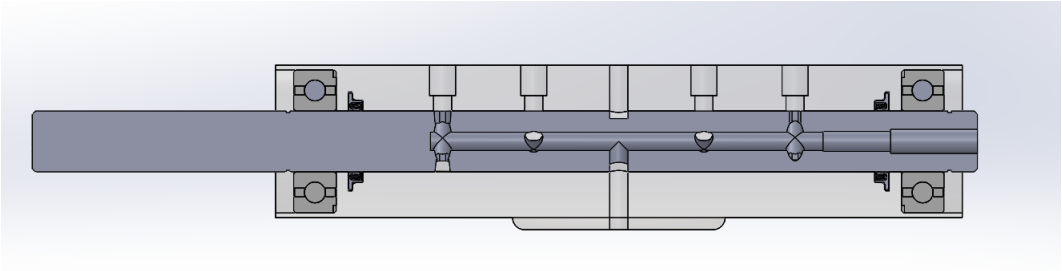

Figure 2.11: Soheli's rotary valve and cylinder head housing

In this design, two rotary seals were used to prevent air leakage and a screw was used to seal the end of the hollow shaft. This design and the rotary seals were adopted in the current system.

2.7 Summary

In this Chapter, the concept of CAES and necessary background information of the ACAES system were included. Since this project benefited from the novel air hybrid engine project and the rotary valve design, a brief literature review and system explanation were also included.

Chapter 3

ACAES Modeling and Simulations

In this chapter, the ACAES system under AC and AM mode is modeled to understand the system behavior. The chapter is organized as follows: Section 3.1 begins with an introduction to the system layout. Detailed system modeling is presented in Section 3.2. In Section 3.3, the mathematical models are evaluated by comparing to the GT-Suite models developed. The experimental system, which consists of the rotary valve and a custom-designed cylinder head, is modeled in GT-Suite in Section 3.4.

3.1 System Layout

The proposed system has the layout shown in Figure 3.1.

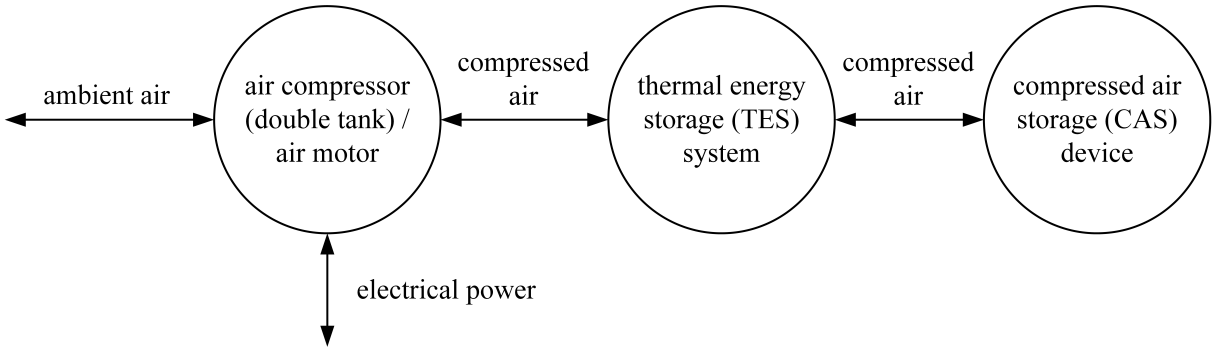

Figure 3.1: System layout with a separate TES

Under the air compression mode, ambient air enters the novel double tank compressor, and the compressed air enters the heat storage device or the TES system. After the TES system, air enters the compressed air storage (CAS), and it is kept at the desired storage temperate. During the expansion process, the air inside the CAS returns to the TES device and absorbs heat before entering the expander to generate electricity. The TES system is designed and modeled later in Chapter 5.

3.2 Mathematical Modeling

The aforementioned system converts electricity into exergy of the compressed air under AC mode and converts exergy back into electricity under AM mode. The system under both modes can be modeled using equations of mass transfer, fluid flow, and energy balance. In this section, a detailed model for the ACAES system is provided.
Figure 3.2 shows the cylinder geometrical parameters [7].

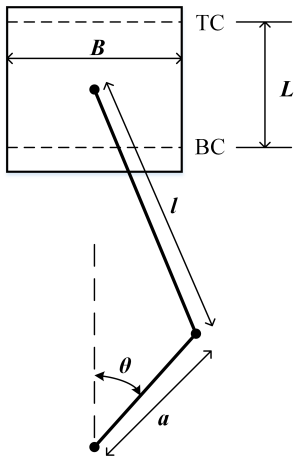

Figure 3.2: Geometry of cylinder, piston, connecting rod, and crankshaft [7]

Based on these parameters, the rate of change of cylinder volumes can be expressed as a function of engine speed and crank angle, as shown below:

$$\dot{V}_{cyl}(\omega,\theta) = \frac{\pi B^2}{4}\left[a\sin\theta + \frac{a^2\sin\theta\cos\theta}{\sqrt{l^2 - a^2\sin^2(\theta)}}\right]\omega \tag{3.1}$$

The volume of the cylinder, at any crank angle, can be calculated as:

$$V_{cyl}(\omega,\theta) = \int \dot{V}_{cyl}dt + V_c \tag{3.2}$$

where V_c is the cylinder clearance volume.

Mass Flow Calculation

For simplicity and convenience, the flow calculation of the AC/AM system neglects the friction loss and heat transfer of the pipelines or the connections between components [1]. The simplified system under AC and AM mode is shown below in Fig. 3.3.

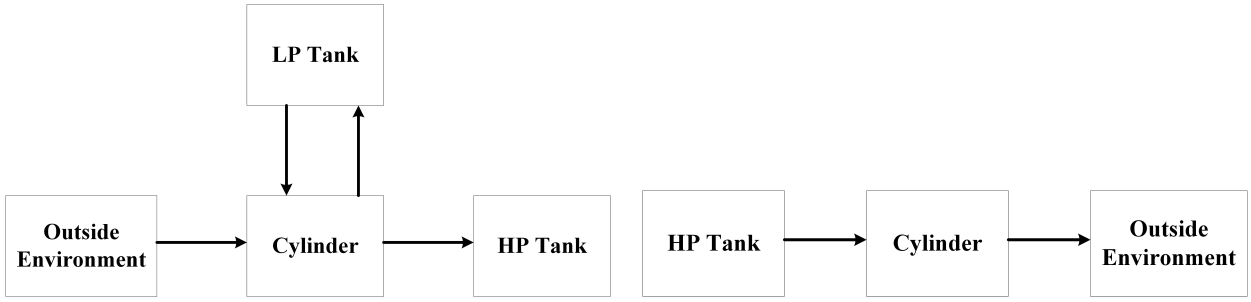

(a) Simplified system under AC mode (b) Simplified system under AM mode

Figure 3.3: Simplified system under AC (a) and AM mode (b). The arrows indicate the actual flow direction due to the check valves installed.

The mass flow rate is thus calculated as flow through an orifice [7] and the critical pressure ratio is calculated as:

$$\frac{P_T}{P_0} = (\frac{2}{\gamma+1})^{\gamma/\gamma-1} \tag{3.3}$$

where subscript T stands for throat or downstream; 0 stands for orifice or upstream; and γ stands for the heat capacity ratio. If the pressure ratio is less than the critical pressure ratio, the flow is sub-critical and the mass flow rate is [50]:

$$\dot{m}_{sub-critical} = \frac{C_D A_T P_0}{R\sqrt{T_0}} \left(\frac{P_T}{P_0}\right)^{1/\gamma} \sqrt{\frac{2\gamma}{\gamma-1}\left[1-\left(\frac{P_T}{P_0}\right)^{\gamma-1/\gamma}\right]} \tag{3.4}$$

Otherwise, if the pressure ratio is higher than the critical pressure ratio, the flow is choked and the mass flow rate is calculated as:

$$\dot{m}_{choked} = \frac{C_D A_T P_0}{\sqrt{RT_0}} \gamma^{1/2} \left(\frac{2}{\gamma+1}\right)^{\frac{\gamma+1}{2(\gamma-1)}} \tag{3.5}$$

[1] Their effects are taken into account later in GT-Suite/Power modeling section 3.3.

Pressure and Temperature Calculation

Even though detailed modeling was done for the AC mode in [1, 51], a different approach based on the ideal gas law and open system energy balance is used here. Assuming air behaves as ideal gas, the ideal gas law can be re-written as:

$$P = \frac{nRT}{V} = \frac{mRT}{MV} \tag{3.6}$$

Due to the reciprocating motion of the piston, the air pressure inside the cylinder can be modeled as:

$$\frac{dP}{dt} = \frac{RT}{MV}\dot{m} + \frac{mR}{MV}\dot{T} - \frac{mRT}{MV^2}\dot{V} \tag{3.7}$$

The mass flow rate and mass inside the cylinder are:

$$\dot{m}_{cyl} = \sum \dot{m}_{in} - \sum \dot{m}_{out} \tag{3.8}$$

$$m_{cyl} = \int \dot{m}_{cyl} + \ m_{cyl,0} \tag{3.9}$$

where the mass flow rates are calculated using Equation 3.4 and 3.5. The term $\dot{T}$ is derived based on energy balances. The rate of change of total energy of the control volume (cylinder volume), taking into account of kinetic and potential energy of air, is [52]:

$$\frac{dE_{cv}}{dt} = \sum \dot{m}_{in,i}(h_{in,i} + \frac{{C^2}_{in,i}}{2} + gz_{in,i}) - \sum \dot{m}_{out,j}(h_{out,j} + \frac{{C^2}_{out,j}}{2} + gz_{out,j}) + \dot{Q} \tag{3.10}$$

Compared with the change of system internal energy, the change of air kinetic energy in the cylinder is relatively small and can be considered to be zero. Since the cylinder inlets and outlets are at the same level, the potential energy change can be neglected. Therefore, $\frac{dE_{cv}}{dt}$ can bve simplfied into:

$$\frac{dE_{cv}}{dt} = \sum \dot{m}_{in,i}h_{in,i} - \sum \dot{m}_{out,j}h_{out,j} + \dot{Q} \tag{3.11}$$

which is equal to the internal energy change rate of gas in the cylinder:

$$\frac{dU_{cy}}{dt} = \dot{m}_{cyl}(h_{cy} - RT_{cy}) + \frac{P_{cy}V_{cy}}{RT_{cy}}(C_{p,cy} - R)\frac{dT_{cy}}{dt} \tag{3.12}$$

This yields the differential equation for cylinder air temperature:

$$\frac{dT_{cy}}{dt} = \frac{RT_{cy}}{P_{cy}V_{cy}(C_{p,cy} - R)}\left[\sum \dot{m}_{in,i}h_{in,i} - \sum \dot{m}_{out,j}h_{out,j} + \dot{Q} - \dot{m}_{cyl}(h_{cy} - RT_{cy})\right] \tag{3.13}$$

The cylinder pressure dynamics is derived after inserting Equations 3.1, 3.2 and 3.13 back into Equation 3.7. Using similar approach and set $\dot{V}$ to zero, the pressure dynamics for HP/LP tank is:

$$\frac{dP}{dt} = \frac{RT}{MV}\dot{m} + \frac{mR}{MV}\dot{T} \tag{3.14}$$

The temperature dynamics for HP/LP tank is:

$$\frac{dT_{tank}}{dt} = \frac{RT_{tank}}{P_{tank}V_{tank}(C_{p,tank} - R)}\left[\sum \dot{m}_{in,i}h_{in,i} - \sum \dot{m}_{out,j}h_{out,j} + \dot{Q} - \dot{m}_{tank}(h_{tank} - RT_{tank})\right] \tag{3.15}$$

Next, the sytem under AM mode is modeled. The cylinder in Fig. 3.3(b) is modeled as a control volume as shown in Figure 3.4 and the flow directions are indicated by the assigned arrows due to the presence of check valves. Thus, assuming that the process is isentropic and air behaves as ideal gas, the cylinder pressure can be derived from the first law of thermodynamics [53] as:

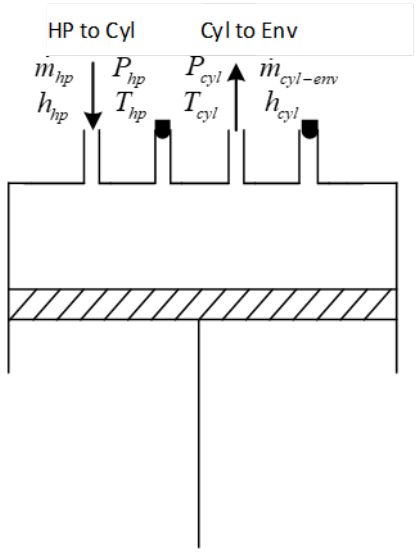

Figure 3.4: Cylinder modeled as a control volume under AM mode

$$\dot{P}_{cy} = \frac{1}{V_{cy}}\left[c^2{}_{hp}\dot{m}_{hp\to cy} - c^2{}_{cy}\dot{m}_{cy\to env} - \gamma P_{cy}\dot{V}_{cy}\right] \tag{3.16}$$

where c stands for the speed of sound which is calculated by:

$$c_{hp} = \sqrt{\gamma RT_{hp}} \quad c_{cy} = \sqrt{\gamma RT_{cy}} \tag{3.17}$$

Based on energy balance, the cylinder temperature equation [11] can be modified as :

$$\dot{T}_{cy} = \frac{1}{C_p m_{cy}} \left[V_{cy}\dot{P}_{cy} + \dot{Q}_{cy} + \dot{m}_{hp\to cy}(h_{hp} - h_{cy}) - \dot{m}_{cy\to env}(h_{cy} - h_{env}) \right] \tag{3.18}$$

where $\dot{Q}_{cy}$ stands for the heat transfer to the cylinder; c_p stands for the specific heat capacity under constant pressure; and h stands for the specific enthalpy [2]. The heat transfer from the cylinder is modeled as convective heat transfer using the Woschni correlative model [54]. Woschni assumed a correlation of the form:

$$Nu = 0.035\mathrm{Re}^m \tag{3.19}$$

Assuming

$$k \propto T^{0.75} \quad \mu \propto T^{0.62} \quad p = \rho RT$$

the convective heat transfer coefficient can be re-written as:

$$h_c = CB^{m-1}p^m w^m T^{0.75-1.62m} \tag{3.20}$$

Taking the exponent m= 0.8, then the Woschini model can be simplified into [50]:

$$h_c = 3.26B^{-0.2}p^{0.8}T^{-0.55}w^{0.8} \tag{3.21}$$

This model assumes simple heat transfer from a confined volume surrounded on all sides by walls representing the cylinder head, piston face and cylinder walls exposed to the combustion chamber. The average cylinder gas velocity,w, is calculated as:

$$w = 2.28\overline{S}_p \tag{3.22}$$

The mean piston speed. $\overline{S}_p$, is defined as:

$$\overline{S}_p = 2LN \tag{3.23}$$

The term $\dot{Q}_{cy}$ can be written as:

$$\dot{Q}_{cy} = h_c A_{cyl}(T_{env} - T_{cyl}) \tag{3.24}$$

The exposed area, A_{cyl}, is a funciton of the crank angle:

$$A_{cyl} = \frac{\pi B^2}{2} + \pi B \left[l + a - \left(a\cos\theta + \sqrt{l^2 - a^2\sin^2\theta} \right) \right] \tag{3.25}$$

[2]Detailed equations for air properties calculation are included in Appendix A .

The engine friction is estimated using Chen-Flynn engine friction model and the Frictional Mean Effective Pressure (FMEP) is a function of mean piston speed, $\overline{S}_p$, and peak cylinder pressure, $\mathrm{P}_{cyl,peak}$, [7]:

$$FMEP = 0.97 + 0.005\ \mathrm{P}_{cyl,peak} + 10^{-5}\overline{S}_p \tag{3.26}$$

Similarly, the pressure and temperature of the HP tank can be modeled as:

$$\dot{P}_{hp} = -\frac{1}{V_{hp}} c^2{}_{hp} \dot{m}_{hp\to cy} \tag{3.27}$$

$$\dot{T}_{hp} = \frac{1}{C_p m_{hp}} \left[V_{hp}\dot{P}_{hp} + KA_{hp}(T_{sur} - T_{hp}) - \dot{m}_{hp\to cy}(h_{hp} - h_{cy}) \right] \tag{3.28}$$

3.3 GT-Suite/Power Modeling

GT-Suite/Power is the standard engine performance simulation software, used by all major engine manufacturers and vehicle OEMs. The software is based on 1-D gas dynamics and can be used to analyze heat transfer, combustion, and vibration. In this section, the mass flow rate equations used in Section 3.2 are evaluated using GT-Suite steady-state simulations. The mathematical models developed in Section 3.2 are compared with GT-Suite models in Section 3.3.2.

3.3.1 Flow Rate Equation Evaluation

In order to verify the flow equations 3.4 and 3.5, simulations are run in GT-Suite and compared with the results from mass flow equations. For the sub-critical flow, the upstream/downstream temperature, downstream pressure are fixed and the inlet pressure are increased from 1.1 bar to 2 bar. Similarly, for the choked flow, the inlet pressure are increased from 3 bar to 12 bar. The same orifice diameter and discharge coefficient, C_d, are applied to the flow equations and GT-Suite model. The steady-state mass flow rates obtained in GT-Suite simulations are recorded and compared with the values obtained from flow equations 3.4 and 3.5 in Figure 3.5 and 3.6.

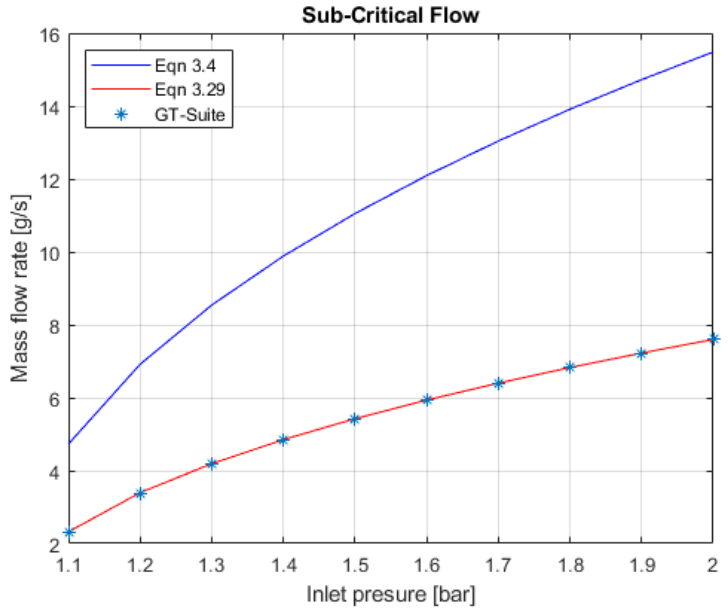

Figure 3.5: Sub-critical flow equations and GT-suite results

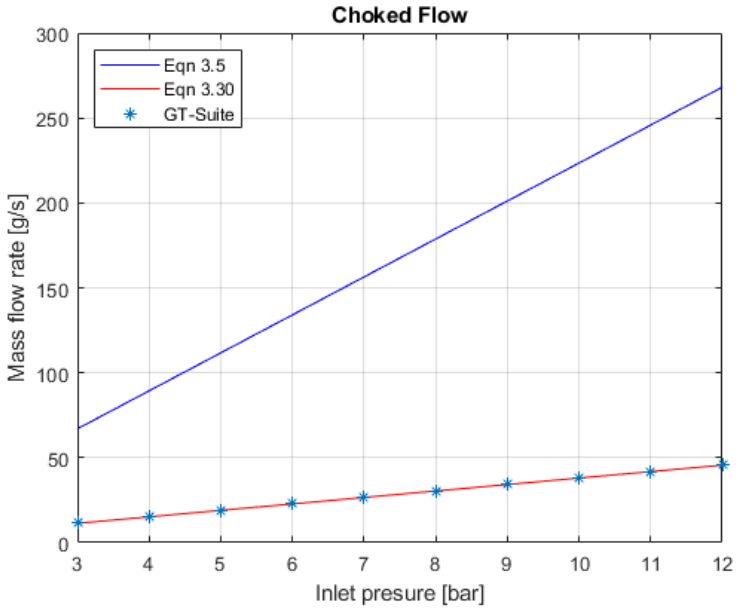

Figure 3.6: Choked flow equations and GT-suite results

From the figures above, it is clear that the results from equations 3.4 and 3.5 are significantly different from GT-Suite's. Therefore, the new mass flow rate equation for sub-critical flow is,

$$\dot{m}_{sub\_critical} = C_D A_T \sqrt{2\rho_0 P_0 \frac{\gamma}{\gamma - 1} \left[\left(\frac{P_T}{P_0}\right)^{2/\gamma} - \left(\frac{P_T}{P_0}\right)^{(\gamma+1)/\gamma} \right]} \tag{3.29}$$

And, the mass flow rate equation for choked flow is [55]:

$$\dot{m}_{choked} = C_D A_T \sqrt{P_0 \rho_0} \gamma^{1/2} \left(\frac{2}{\gamma + 1} \right)^{\frac{\gamma+1}{2(\gamma-1)}} \tag{3.30}$$

Equation 3.29 and 3.30 yield very accurate air flow mass flow rate results when compared to the average mass flow rates obtained from GT-Suite simulations.

3.3.2 GT-Suite Modeling of the Simplified System

A single-cylinder engine with combustion turned off is modeled in GT-Suite. The compression ratio was reduced from 8.5 to 7.2 due to the volume of valves and pipe fittings added to the system. Detail engine specifications can be found in Appendix B.1. The mathematical models derived in Section 3.2 are built in Simulink. Under AC mode, mathematical model and GT-Suite simulation results for tank pressures are shown and compared in Fig 3.7.

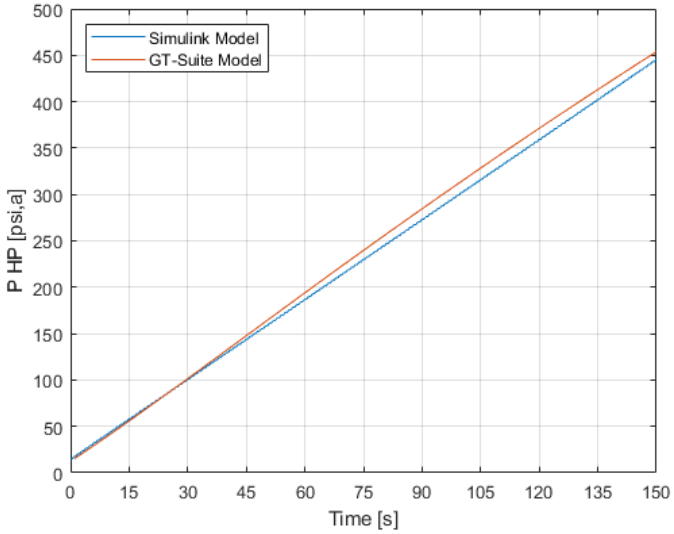

Figure 3.7: HP tank pressures under AC mode

The error, defined as the difference between $P_{hp,gt}$ and $P_{hp,simulink}$, is calculated and the descriptive statistics is shown in Table 3.1.

Table 3.1: P_{hp} $[psi]$ error descriptive statistics

Descriptive statistics	Value
Mean:	6.640
Median:	8.744
Min:	-2.909
Max:	12.154
Standard deviation:	5.253

Similarly, the HP tank pressures under AM mode are shown and compared in Fig 3.8.

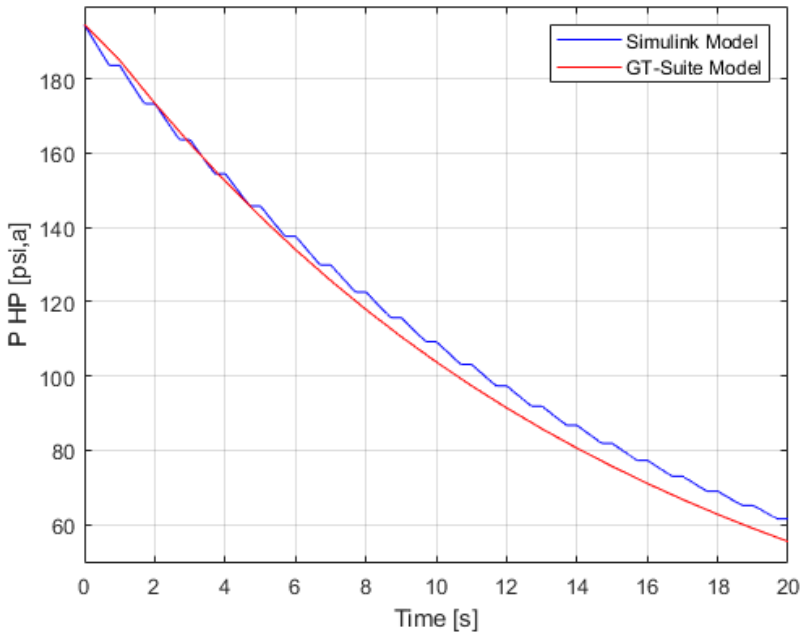

Figure 3.8: HP tank pressures under AM mode

These figures indicate that the mathematical models simulated in Simulink are consistent with GT-Suite models. The differences between the mathematical model and GT-Suite model are due to the following assumptions of the mathematical model:

- Constant γ of 1.38 (In GT-Suite, this value is changing based on upstream and downstream pressures and temperatures).
- Ideal gas model (Effects of pressure on C_p and h are neglected in the mathematical models but are taken into account in the GT-Suite models).

3.4 GT-Suite Modeling of the Experimental System

The cylinder head and rotary valve, shown in Figure 2.11, are simplified and modelled in the following sections:

3.4.1 Modeling of Cylinder Head and Rotary Valve

Since the exact valve model is not available in GT-Suite, the cylinder head and rotary valve, are modeled as a system of pipes, solenoid valves, and orifices, as shown in Figure 3.9. The rotary valve's valve timing in Table 2.1 is converted into the equivalent solenoid valve timing while the solenoid valve opening/closing profile is calculated based on rotary valve's geometry and rotational speed of the crankshaft[3]. Detailed rotary valve specifications are included in Appendix B.2.

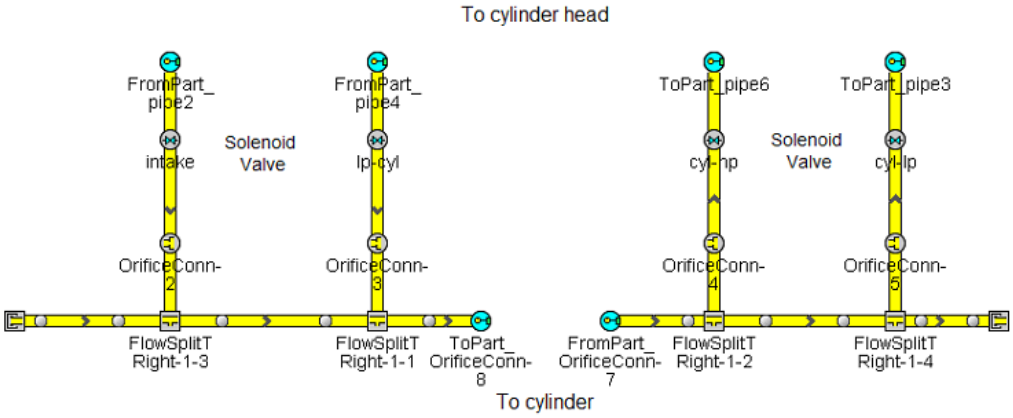

Figure 3.9: Rotary Valve GT-Suite/Power model

[3]Due to the gear ratio of 2:1, the rotary valve rotates at half of the crankshaft speed.

CFD Analysis

The solenoid model developed in GT-Suite requires the solenoid valve discharge coefficient C_D as a function of the valve lift L. $C_D(L)$ is obtained by running CFD analysis in ANSYS Fluent. The flow volume of the cylinder head is extracted in ANSYS SpaceClaim and the excess volume occupied by the ball bearings, rotary seals and support structures is trimmed. The rotary valve is imported as a solid and placed inside the cylinder head volume with a clearance of 0.1 mm, as shown in Figure 3.10.

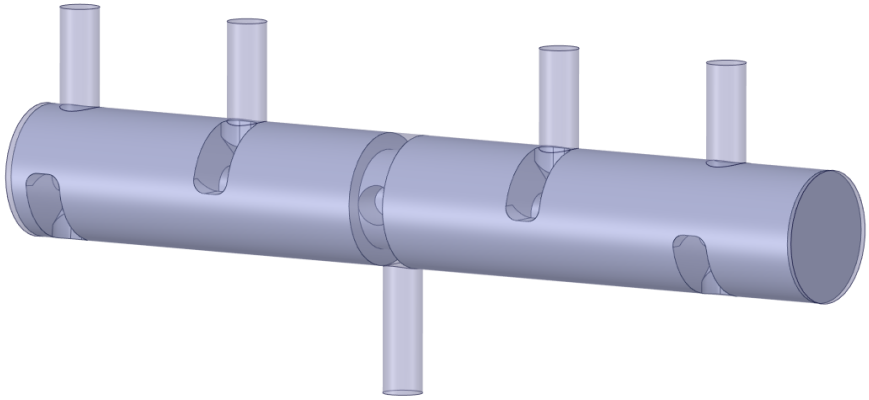

Figure 3.10: Rotary Valve and extracted Cylinder head volume in ANSYS SpaceClaim

For the meshing, default meshing is used and the mesh near the valve ports are refined such that the maximum skewness is reduced from 0.9454 to 0.8457 (triangle cells was used) and the average skewness is 0.2242 with a standard deviation of 0.1212.

The CFD setup is done in ANSYS Fluent. For the solver settings, steady state pressure and temperature are imposed on all ports of the cylinder head volume and the rotary valve is set to rotate at 250 RPM. The velocity streamline of port 1 (inlet) is shown in Figure 3.11. Using the flow velocities obtained and boundaries conditions imposed, the $C_D(L)$ is calculated based on equation 3.29 and 3.30.

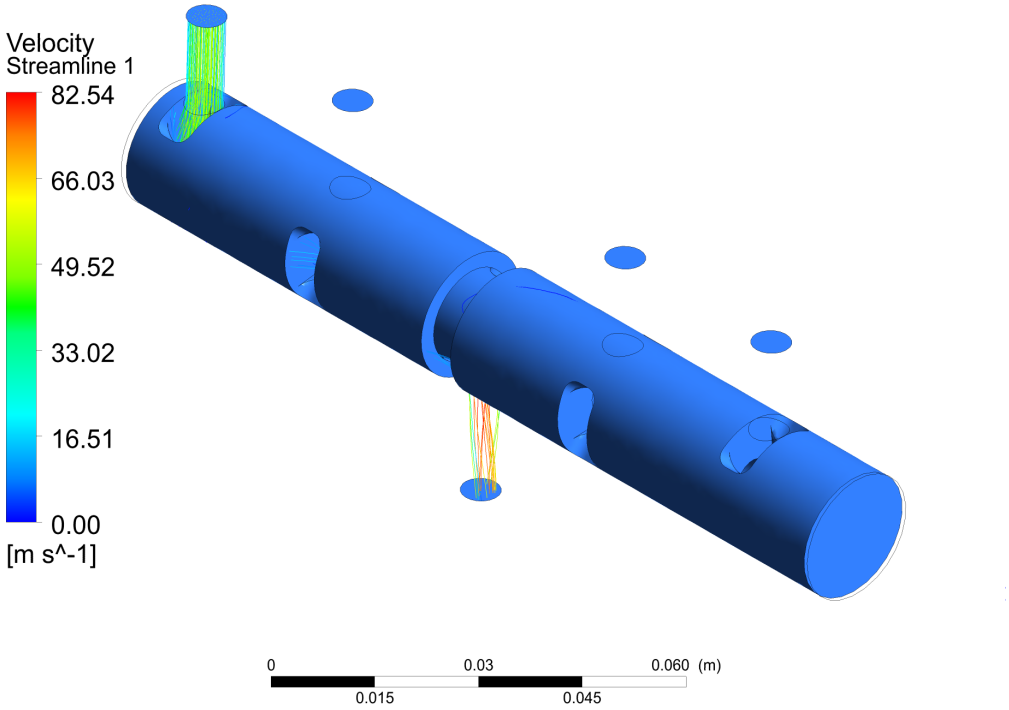

Figure 3.11: Velocity streamline of port 1 (inlet) obtained from CFD analysis.

Air Compression/Motor Modeling

Under AC mode, the rotary valve and the novel double-tank compression strategy are added into the base-line engine with combustion turned off. The LP tank, HP tank, pipes, check valves, and orifices are added into the model.

Under AM mode, the LP tank is removed and valve 2 and 4 [4] are connected to end seals since there is no flow through them as mentioned in Table 2.1. The final GT models for the system under AC and AM mode are shown in Figure 3.12.

[4]Since valve 2 and 3 have the same valve timing, valve 2 and 4 are sealed instead of valve 3 and 4. Valve 3 is connected to the outside environment for convenience such that there is no need to change the rotary valve connection in Figure 3.9 (The arrow in GT-Suite indicates the assumed flow direction).

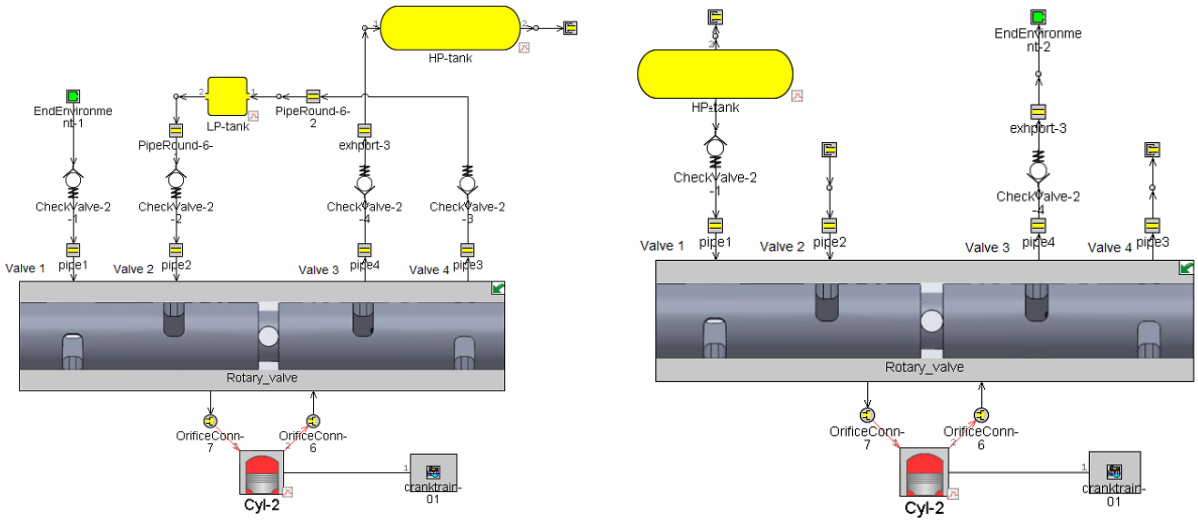

(a) Air Compression GT-Suite/Power model

(b) Air motor GT-Suite/Power model

Figure 3.12: GT-Suite/Power model under AC (a) and AM mode (b).

3.5 Summary

In this chapter, the mathematical model of the system was developed. Simulations ran in GT-Suite yielded consistent results with mathematical models'. The experimental system, which consists of the rotary valve and cylinder head, was modeled in GT-Suite. In the following chapter, the GT-Suite models were evaluated and verified by experimental studies.

Chapter 4

Experimental Studies

4.1 Previous Prototype Evaluation

The previous prototype, shown in Figure 4.1, was tested to evaluate the valve timing proposed by Fazeli [1]. The results of this evaluation are summarized below:

Figure 4.1: Previous Prototype

Rotary Valve

The valve timing is calculated based on the CAD file and converted to the equivalent valve timings in Figure 4.2 (a). The rotary valve opens at the correct CA but only opens for 112 ° instead of 180°, as shown in Figure 4.2 (b). This leads to low tank pressures when running the AC mode at 500 RPM, as shown in Figure 4.3.

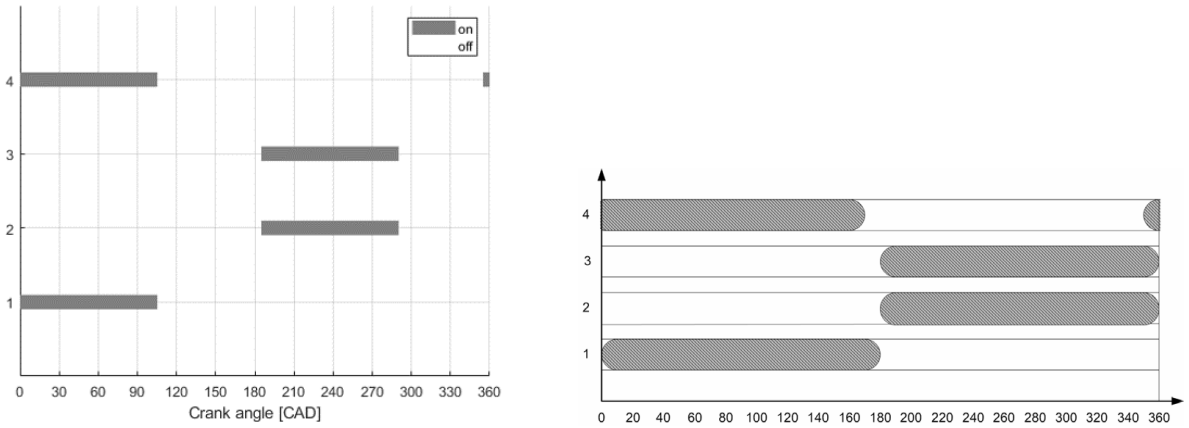

(a) Equivalent valve timing

(b) Fazeli's proposed valve timing

Figure 4.2: Rotary valve (a) Equivalent valve timing (b) Fazeli's proposed valve timing

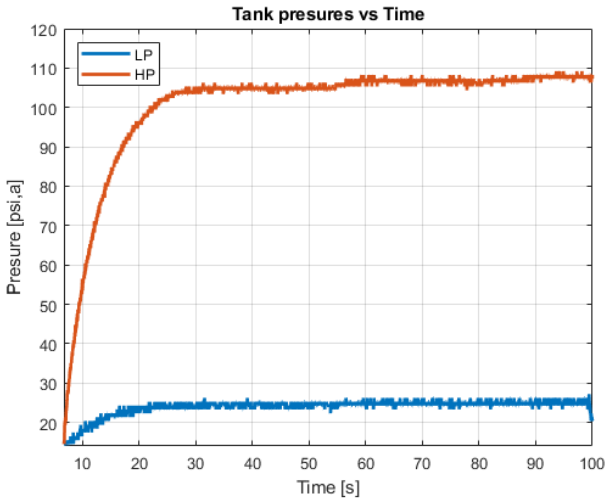

Figure 4.3: HP/LP tank Pressure vs t

Mechanical Connection and Sealing

In the original prototype, all connections between pipe fittings were sealed using standard PTFE (Teflon) tape. This could cause leakage if the tape was not applied correctly or too much tape was applied. For the engine, the cylinder head was mounted to the cylinder using bolts, and a head gasket was used to seal the gap between them. Air could leak through the gap between the bolts and the mounting holes, even if enough torque was applied to the bolts.

4.2 Experimental Setup

The new experimental setup under AC mode is shown in Figure 4.4. The rotary valve was installed and connected to the crankshaft with a timing belt. The engine crankshaft is coupled to a dynamometer (dyno) used to spin the engine for testing. The new experimental setup is summarized below. A detailed parts lists can be found in Appendix C.

Figure 4.4: Final Prototype under AC mode

4.2.1 Mechanical Setup

Rotary Valve

A new rotary valve is manufactured from 20mm precision ground 416 stainless steel shaft, and the ports are widened to 90 °with necessary fillets. The new rotary valve's equivalent valve timing is identical to the valve timing proposed by Fazeli. Fillets are added to both ends of the rotary valve to simplify the seal installation process and reduce the damage to the seals. The old and new rotary valves are compared in Figure 4.5.

Figure 4.5: Old (bottom) and new (top) rotary valve comparison

Mechanical Connection and Sealing

For the new experimental setup, metal tubes, silencer, pressure relief valves (set at 300 psi for HP tank and 200 psi for LP tank), and ball valves are added to improve safety during regular operation and mode switching. The system layout under AC mode is shown in Figure 4.6. When switching from AC to AM mode, the high-pressure ball valves installed are used to isolate the HP/LP tanks from the rest of the system such that the mechanical connections can be changed safely. As mentioned before, the LP tank and associated pipes, valves are removed from the experimental setup under AM mode.

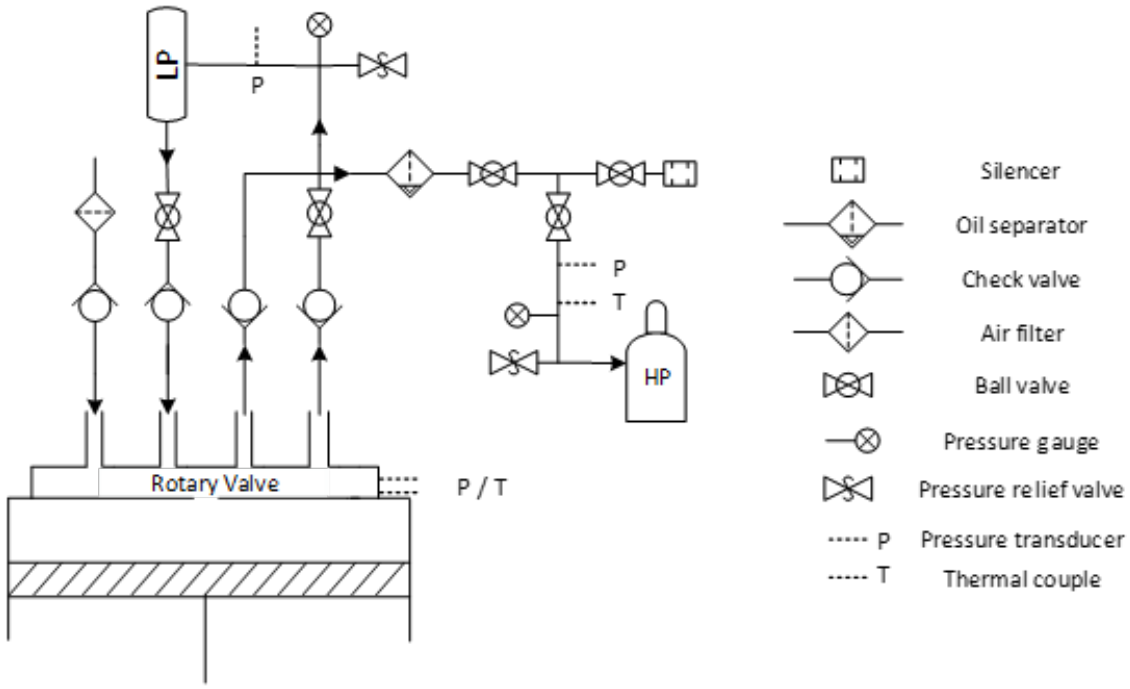

Figure 4.6: Experimental setup layout under AC mode

Rather than using the Teflon tape, high-temperature thread sealants are used to seal all metal pipe fittings and connections. For the cylinder and cylinder head gasket connection, the bolts are wrapped with Teflon tape, and fluorine rubber O-rings are placed to seal the mounting holes. Also, the rotary valve's end screw is sealed with Teflon tape and an O-ring.

Parameter Identification/Verification

For the engine component, the connecting rod length is measured based on the stroke and distance between the crankshaft and the rotary valve. The TDC clearance height is estimated using the cylinder head CAD model and the distance measured between the piston TDC position and the cylinder top surface. Parameters such as piston and connecting rod masses are approximated based on parts data listed online. The crankshaft inertia is calculated by approximating the universal coupler and crankshaft as a single rod with a non-uniform diameter. The calculated crankshaft inertia is verified by comparing to crankshaft inertia used in a standard compressor/engine.

For flow components, the check valve is modeled using the volumetric flow rate vs. pressure difference table published by the manufacturer. The HP/LP tank volumes are verified by pouring water into the tanks and measuring the differences between dry and wet weight.

4.2.2 Electrical Setup

Figure 4.7 (a) shows the physical layout of the electrical system. The digital acquisition is achieved through the dSPACE data acquisition and control system. Raw data from sensors is processed through analog and encoder input boards.

The system sensors are routed through the electrical control panel, shown in Figure 4.7 (b), which contains the power supplies, dSPACE terminal blocks for each dSPACE board, fuses and relays.

Table 4.1 and 4.2 describe all the sensor connections and inputs.

(a) Electrical panel and dSpace setup

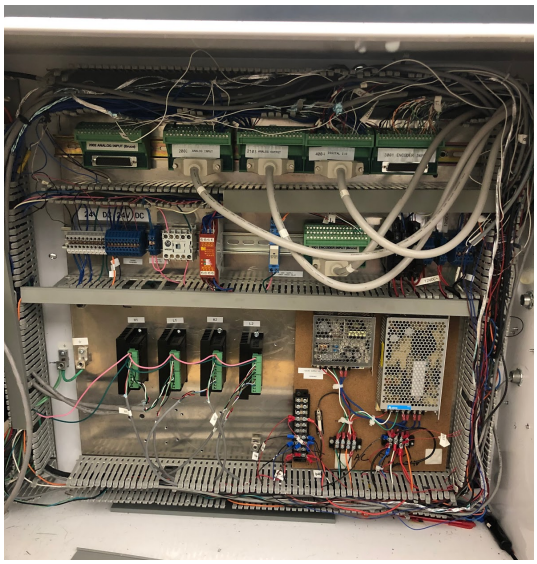

(b) Control panel internal layout

Figure 4.7: (a) Electrical panel and dSpace setup (b) Control panel internal layout

Table 4.1: dSPACE Board Descriptions

dSPACE Board	Description
DS 2002	Multi-Channel Analog-to-Digital Board
DS 3001	Incremental Encoder Interface Board

Table 4.2: System Inputs

Input	Sensor Type	Description	dSPACE Board
Engine Torque	Torque Transducer	Engine Torque	DS 2002
HP Tank Pressure	Pressure Transducer	P_{hp}	DS 2002
LP Tank Pressure	Pressure Transducer	P_{lp}	DS 2002
Cylinder Pressure	Pressure Transducer	$P_{cy,abs}$	DS 2002
HP Tank Temperature	Thermocouple	T_{hp}	DS 2002
Cylinder Head Temperature	Thermocouple	T_{cy}	DS 2002
Crankshaft Angle	Incremental Encoder	CA	DS 3001

Sensor Initialization

At the beginning of every test, the piston is brought to TDC position, which was marked on the crankshaft when the piston reached the TDC postion during the assembly process. Therefore, the initial incremental encoder reading is set to 0 °. For the pressure transducers, all initial values are set to be 0 psi for gauge pressure sensors while the initial value for the absolute pressure transducer, $P_{cy,abs}$, is set to be 14.696 psi. For the thermocouples, the room temperature is measured and set to the initial sensor readings.

4.2.3 Software Setup

The digital acquisition runs on a Simulink model deployed to the dSPACE hardware. During testing, a Graphical User Interface (GUI) designed in dSPACE ControlDesk is used to view live data and record data.

Simulink Model and Data Filtering

The Simulink model, shown in Figure 4.8, consists of the data acquisition, filtering and recording. The raw sensor data in dSPACE, normalized between -1 to 1, is scaled. A pre-test (all sensors on, no motoring) is run to calibrate the torque sensor. A moving average filter is designed, and the filtered torque sensor data is compared with the scaled sensor data shown in 4.9. The offsets, obtained from this pre-test and sensor initialization, are added to the filtered data before data recording.

dSPACE ControlDesk GUI

The GUI was designed in dSPACE ControlDesk and it interfaces with the Simulink model deployed to the dSPACE hardware. The user can visualize real time sensor data, record data, and adjust settings using the interface shown in Figure 4.10.

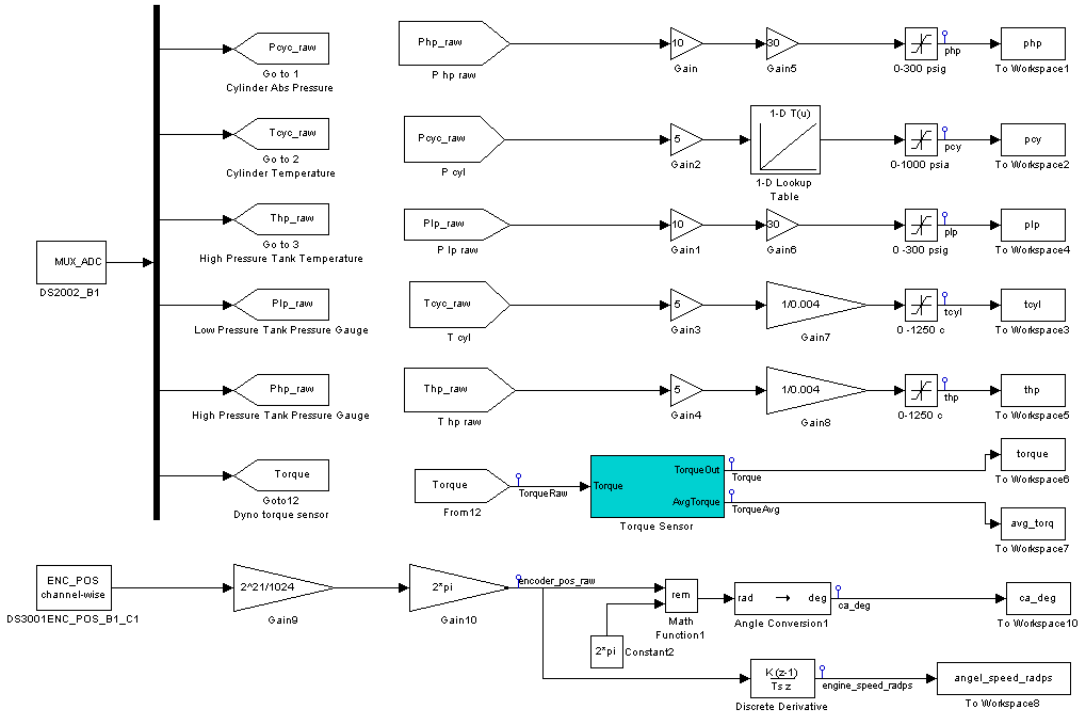

Figure 4.8: Simulink model deployed to dSPACE hardware

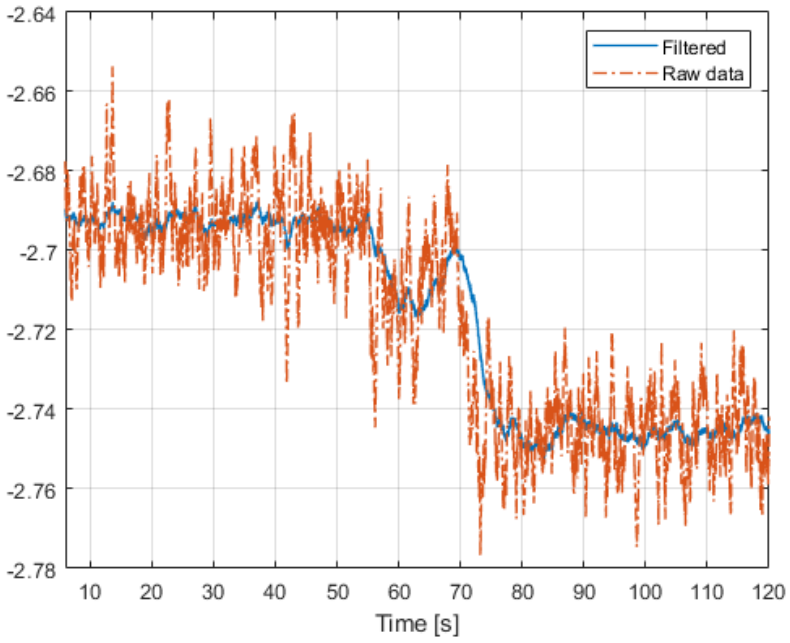

Figure 4.9: Torque sensor data filtering

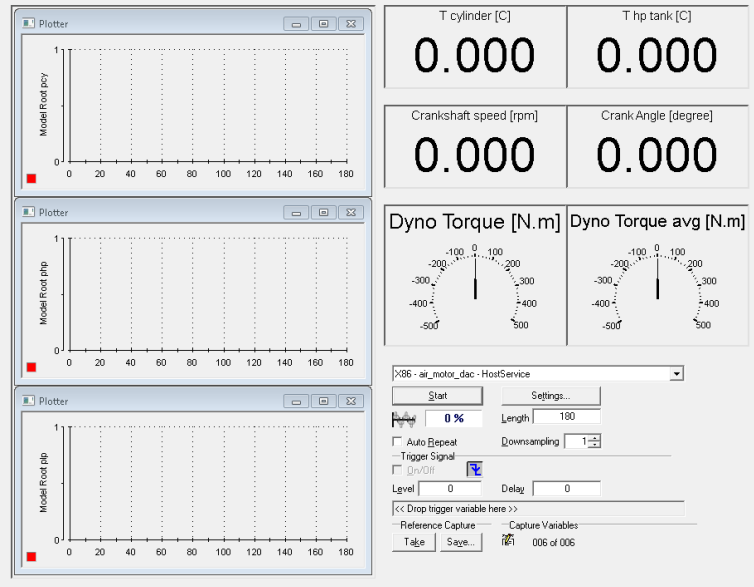

Figure 4.10: dSPACE ControlDesk GUI

4.2.4 Safety Measures

In the experimental system, there are many physical and software safety measures implemented to prevent damage to the system and the operator. The safety measures are listed below:

- Dyno is set to speed mode to prevent excess torque/speed under torque and power mode. In addition, dyno can only rotate up to 500 RPM.
- Dyno emergency stop and coast button.
- The pressure relief valve opens at 300/200 [psi,g] for HP/LP tank. All the air tanks are equipped with silencers to reduce the noise during the discharge process.
- Two digital thermometers are placed on the top and side of the cylinder head to monitor the surface temperature to prevent damaging pressure transducers. Furthermore, the system under AC mode can only run up to 10 minutes consecutively, after which the system needs to be cooled.

4.3 Experimental Results and Model Calibration

Using the experimental setup, different experiments are conducted to validate the GT-Suite models developed in Section 3.4.

4.3.1 AC mode

Based on the experimental result in Figure 4.11, under AC mode, the LP tank pressure experiences significant oscillations even after applying the moving average filter. The oscillations are due to the airflow from or into the cylinder. In GT-Suite, the LP tank pressure value is averaged, and the instantaneous pressure changes won't be reflected. Therefore, the LP tank pressure cannot be used to evaluate the model accuracy. Instead, HP tank pressure and dyno torque are used to verify the models developed in GT-Suite.

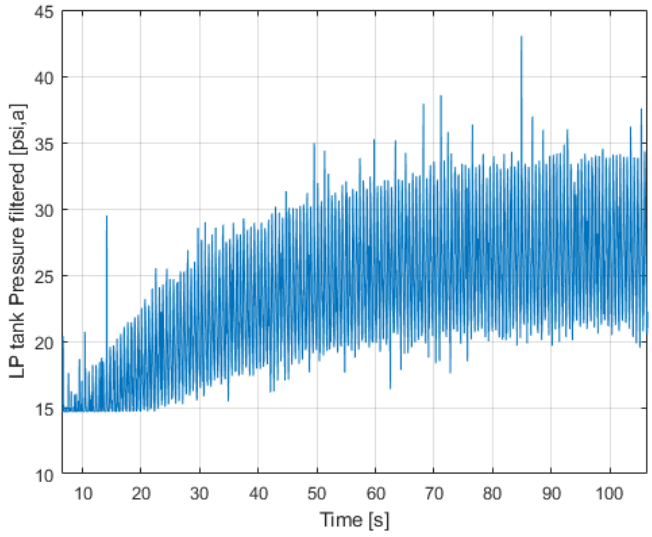

Figure 4.11: Filtered LP tank pressure collected at 100 RPM air compression

In the initial experiments, cylinder head and HP tank leakage caused the system to work far below its ideal performance. The HP tank pressure recorded in one of the experiments is shown in Figure 4.12. After the air compression stops at t= 100 [s], the HP tank pressure drops from 102.242 [psi,a] to 86.722 [psi,a] at t=113.23 [s] which corresponds to a rate of 1.098 psi/s. The leakage problem was later solved by replacing the cylinder head gasket, o-rings, and re-assembling all the pipes, valves, pipe fittings.

After running several experiments, some issues have been noticed that could cause the experimental system to differ from the GT-Suite model. First, in the experimental system, the crankshaft is connected to the dyno via a universal coupler, and there exists a 2-3° angle with respect to the steel table plane (parallel to the ground). This small angle causes the actual rotational speed to be slightly lower than the constant engine speed imposed in GT-Suite models. In addition, in GT-Suite simulation, it is assumed that the engine rotates at constant RPM starting at t=0 [s]. In reality, the dyno needs a few seconds to accelerate the universal coupler/ crankshaft assembly to the commanded rotational speed.

For the first problem, the angle between the universal coupler and the steel table is measured and entered into the GT-Suite model. For the engine speed problem, a ramp signal is generated to compensate for the acceleration and deceleration process based on the dyno's datasheet and controller settings.

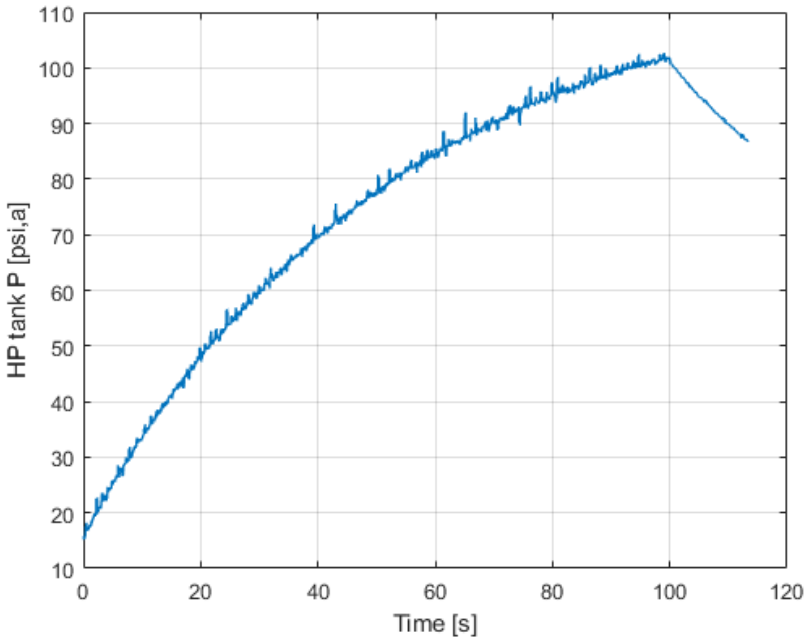

Figure 4.12: Filtered HP tank pressure collected at 300 RPM air compression

Next, the GT-Suite model is validated by comparing to the experimental results. Since the dyno is constrained to rotate up to 500 RPM due to safety concerns, the HP tank pressures obtained from the GT-suite model and experiment run at 500 RPM under AC mode are compared below.

In Figure 4.13, the raw experimental HP tank pressure is compared with the filtered experimental HP tank pressure. The moving-average filter designed previously is able to filter out the excessive electrical noise or spikes as desired. The HP tank pressure reaches 180 [psi,a] after 150 s, which is a 28.85% increase compared to the HP pressure obtained by Fazeli in [1]. This might be insignificant at first glance, but the new system intake diameter is only 6 mm, while Fazeli's prototype intake diameter was over 20 mm.

Figure 4.14 compares the filtered experimental result to the GT-model result. Based on the figure below, the GT model is able to accurately predict the HP tank pressure over the duration of 150 seconds. Since the experimental result is sampled at 1 KHz, in order to compute the pressure error, the experimental data is reduced to 12 Hz to match the sampling frequency of the GT-Suite result. The HP tank pressure error is computed and the descriptive statistics is used to quantify the pressure error, as listed in Table 4.3.

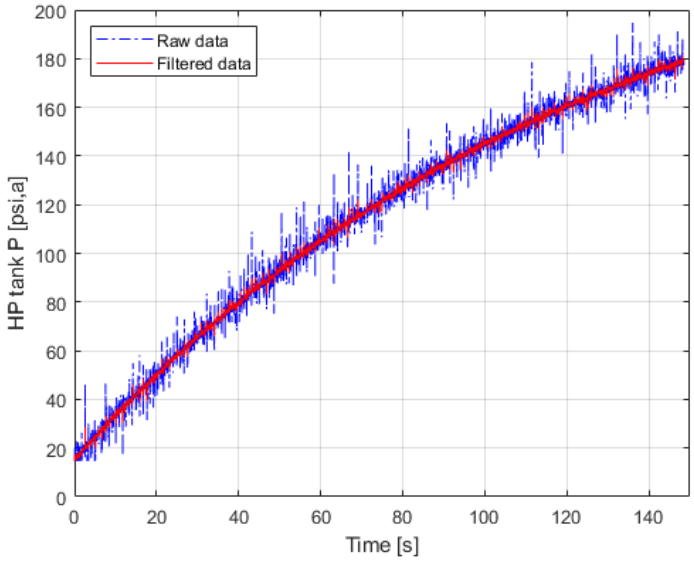

Figure 4.13: Raw V.S Filtered experimental HP tank pressure

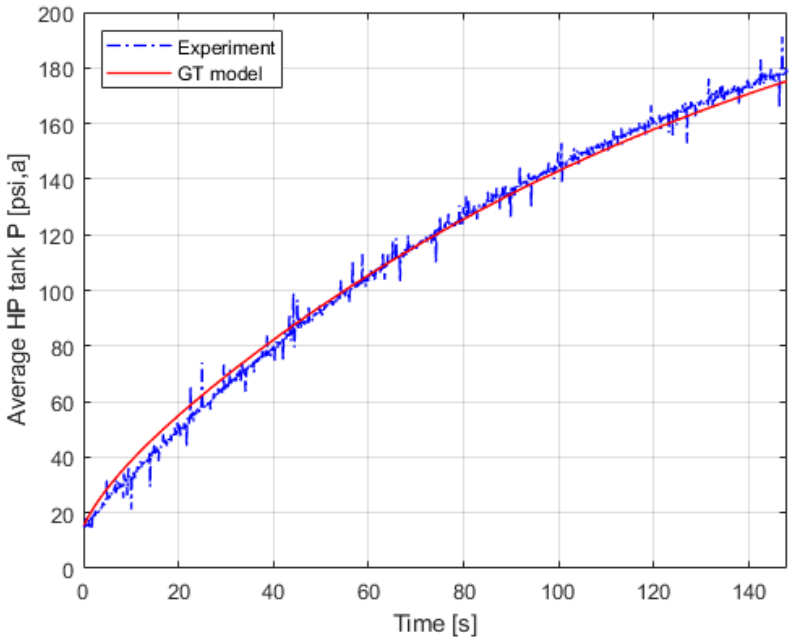

Figure 4.14: Filtered HP tank pressure V.S GT-Suite result

Table 4.3: P_{hp} $[psi]$ error descriptive statistics

Descriptive statistics	Value
Mean:	-0.292
Median:	0.322
Min:	-10.838
Max:	6.193
Standard deviation:	3.008

The HP tank error has a mean of -0.292 and a median of 0.322 over 150 seconds. The minimum value of -10.838 seems large, but this value is mostly due to the electrical noises generated from motor controllers, PLCs, and dyno. This noise can be further reduced by using a moving-average filter with a longer span or adding an extra pressure transducer. Similarly, the engine torque obtained from the experiment is compared to the brake torque from GT-Suite simulation, as shown in Figure 4.15. The initial engine torque matches the brake torque reported in [1], and engine torque increases as a result of higher tank pressure. Overall, the torque recorded in the experiment matches the brake torque reported in GT-Suite simulation.

Using the same approach, the brake torque error is calculated by matching the sampling rate and the error descriptive statistics is shown in Table 4.4.

The brake torque error mean and median are in the range of 0.372-0.393 which corresponds to a error of 7.6% when brake torque is -5 [N.m] or 1.42% when the brake torque is -27 [N.m]. The error is mostly due to the following factors:

- The engines specifications identified/verified in Section 4.2.1 are used for GT-Suite simulations. These data could be slightly different from the actual value due to observational error causing the brake torque to be slightly different.
- In GT-Suite, the brake torque is averaged which means instantaneous brake torque fluctuations won't be reflected. For the experimental torque, as mentioned in Section 4.2.3, the data (raw or filtered) contains some level of noise.

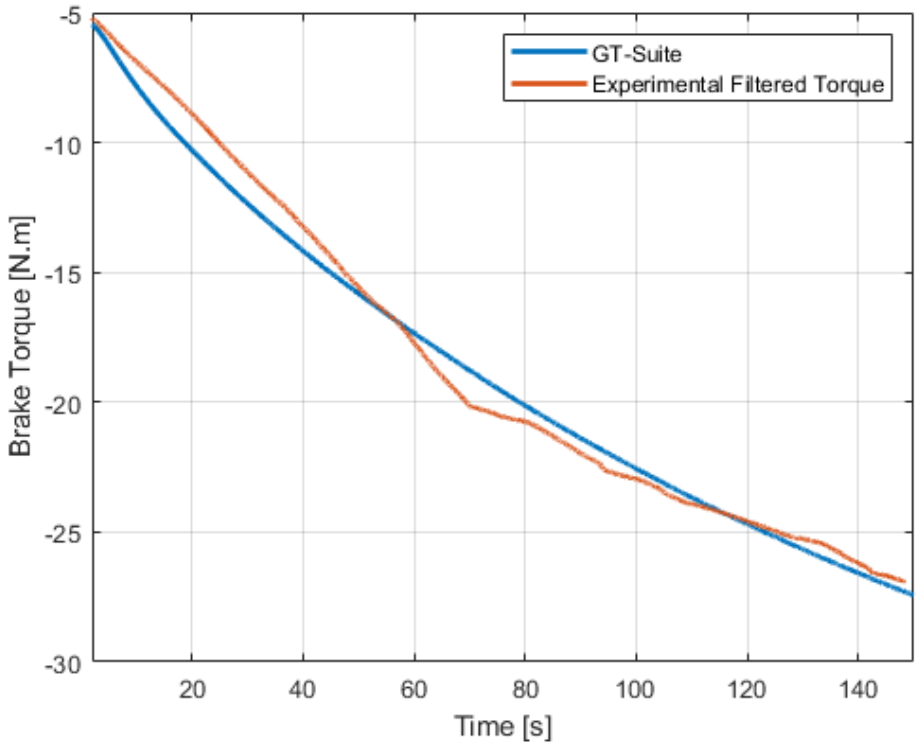

Figure 4.15: Filtered engine torque V.S GT-Suite result

Table 4.4: Brake Torque error descriptive statistics

Descriptive statistics	Value
Mean:	0.393
Median:	0.373
Min:	-1.169
Max:	1.747
Standard deviation:	0.785

4.3.2 AM mode

For the AM mode, the HP tank is charged to 180 [psi,a] by running the system under AC mode. The experimental system is set to 100 RPM, and the AM mode is activated 5

seconds later. The filtered HP tank pressure, shown in Figure 4.16, drops from 180 [psi,a] to 20 [psi,a] in 25 seconds. This is expected since the HP tank volume is less than 3 L. The experimental result is consistent with the HP tank pressure obtained from GT-Suite simulation.

To prolong the AM mode duration , AM mode with an HP tank of 30 L is simulated in GT-Suite with the same parameters used in GT-Suite models developed for AC mode. The HP tank pressure and engine indicated power are shown in Figure 4.17 and 4.18, respectively. With a HP tank of 30 L, in Figure 4.17, the HP tank pressure drops from 180 [psi,a] to 55 [psi,a] in 120 seconds. Increasing the HP tank size allows more compressed air (or energy) to be stored and reduces the pressure dropping caused by discharging air. In Figure 4.18, the engine indicated power decreases with the HP tank pressure.

Compared to the experimental result in [1], at the same tank pressures, the new experimental system's indicated power is slightly lower. This is due to the smaller inlet diameter used in the new experimental system. When removing the rotary valve, the side seals are damaged (see Figure 4.19), and the V-shape metal spring leaves the scratches on the rotary valve and cylinder head inner surface as shown in Figure 4.20. These scratches result in minor air leakage between the rotary valve and the cylinder head.

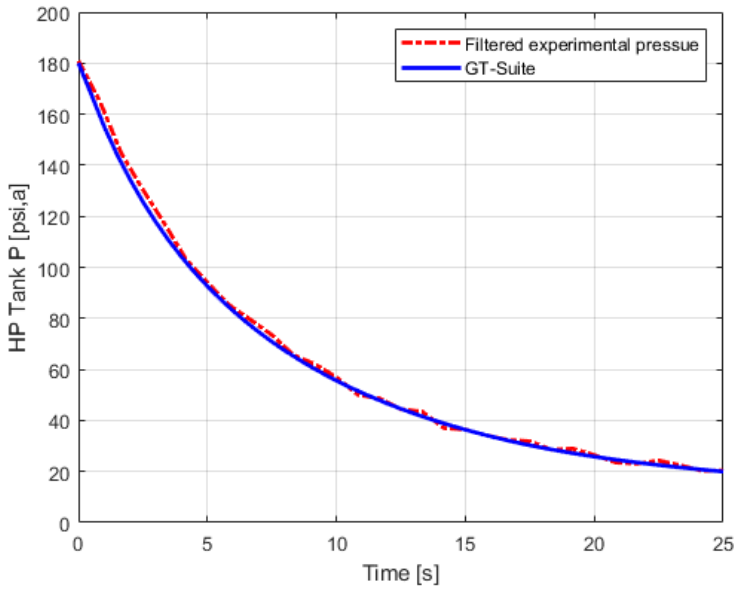

Figure 4.16: HP tank pressure

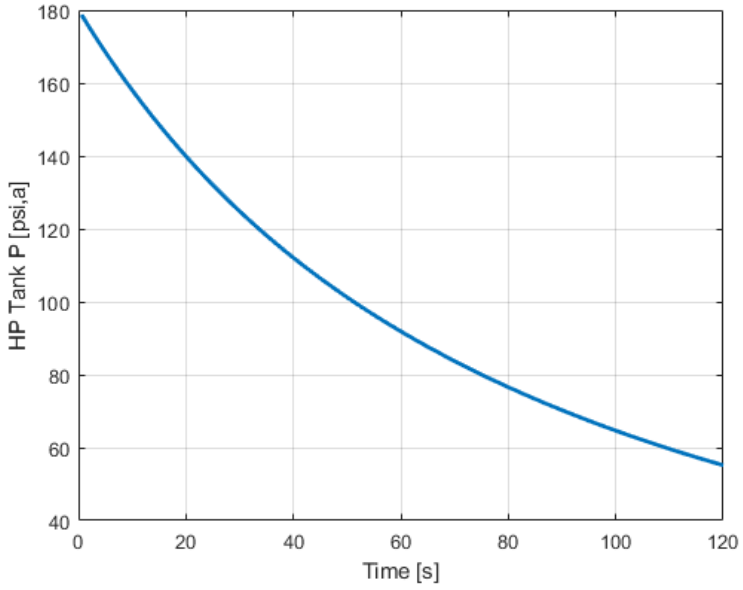

Figure 4.17: HP tank pressure

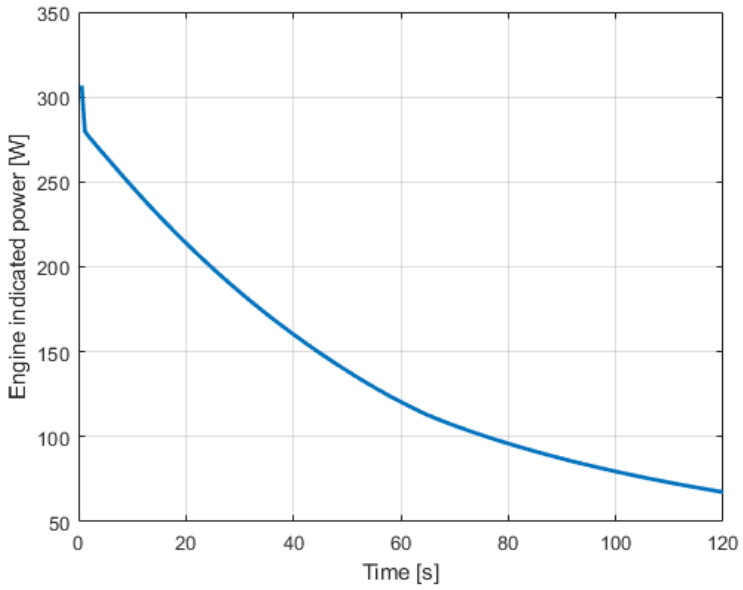

Figure 4.18: Engine indicated power

Figure 4.19: Damaged side seals with the metal V-shape spring

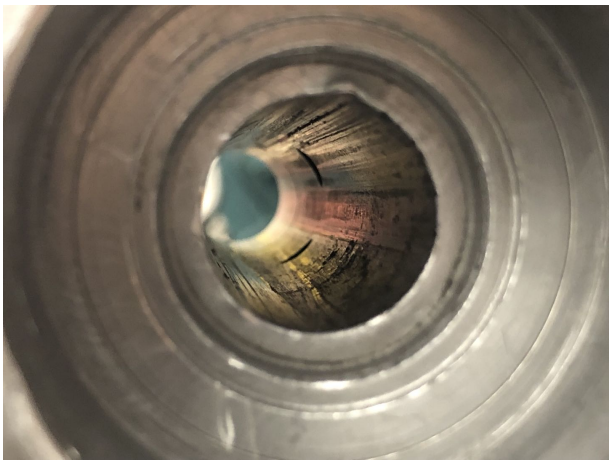

(a) Cylinder head inner surface

(b) Rotary valve

Figure 4.20: Damaged (a) cylinder head inner surface (b) rotary valve

Noise and Sensor Accuracy

Due to the motor drivers, motor power supplies, sensor power supplies installed in the electrical panel, there exists a ∼0.1 V electrical noise in all the sensor readings. The electrical noise had a significant impact on the thermal couples and pressure transducer (cylinder). For the cylinder pressure transducer, the measuring range is 0-1000 [psi,a] with

a sensor output of 0-5V. For this pressure sensor, the electrical noise could yield to a maximum error of 20 [psi].

Using the low-pass filter and the moving-average filter, all these sensors are adequate for the experimental analysis mentioned in this chapter. Further calibration of the system model (cylinder pressure calibration within a crankshaft revolution) would require reducing system noise by electrically separate sensors and drivers or purchasing sensors with smaller ranges.

4.4 Summary

In this chapter, the previous prototype was evaluated in Section 4.1. The experimental setup was documented in detail and separated into mechanical, electrical, and software setup subsections. Pre-tests were run to obtain sensor readings offsets and to design a filter for the torque sensor data. The experimental data, collected using the dSPACE system, was used to verify and calibrate the GT-Suite models in Section 4.3.

Chapter 5

ACAES System Design and Brake Power Control

5.1 ACAES System Design

The energy stored in the exergy of compressed air can be calculated using the function below [2]:

$$P_{el} = \dot{m}\left[T_a C_{p^o}(\frac{T}{T_a} - 1 - \ln(\frac{T}{T_a})) + T_a R_L \ln(\frac{P}{P_a})\right] \tag{5.1}$$

Based on the equation, the pressure's contribution to the exergy is compared to the temperature's [2]. At low air pressure (less than 8.3 MPa), the pressure's contribution dominants over that of temperature. At higher pressure, the temperature's contribution becomes dominant.

For an ideal ACAES process, there is no difference between storing the energy in the form of heat (temperature) and kinetic energy (pressure) together and if storing them separately. However, for practical reasons listed below, thermal energy should be stored separately.

- Leakage prevention becomes difficult and expensive for high temperature compressed air. Because of this, operational safety cannot be guaranteed unless the strict material requirement is satisfied.
- Due to low air density at high temperature, large storage devices are needed, which leads to low energy storage density.Furthermore, this causes a large surface to be insulated to prevent energy loss due to heat transfer.

As mentioned in Section 2.2, depending on the air storage temperature, the ACAES system can be classified into high/medium/low-temperature ACAES. For this project, low-temperature ACAES system with a separate TES is selected for the following reasons:

- High air storage temperature means high compressor outlet temperature. Since the high-temperature sealant used in this project is rated up to 200°C, potential leakage could cause safety problems.
- Significant heat loss can occur at the surface of metal tanks chosen as the air storage device.
- For the heat exchanger system in medium/high-temperature ACAES, there is a large difference between the inlet temperature of air and heat transfer fluid. The large temperature difference creates thermal stress on the heat-exchanger material and could lead to mechanical failure caused by fatigue and thermal expansion in the long run.

Based on the reasons mentioned above, the maximum air storage temperature is set to 200°C. The actual air storage temperature is governed by the TES system performance and compressor discharge temperature.

5.1.1 TES System Design, Modelling and Control

TES Concept Selection

From numerous TES concepts proven in solar power plants [28, 29], the single-tank TES configuration with liquid heat transfer medium is selected. Compared to the two-tank TES configuration, as mentioned in Section 2.3, the single-tank design reduces the space and costs for an extra tank and eliminates additional pipelines. In the single-tank configuration, the hot and cold fluids are separated due to the stratification.

Heat Transfer Medium

The most important benefit of choosing low-temperature TES is that pumpable heat transfer medium like heat transfer oil and water can be used. Compared to oil, water's high heat capacity allows the usage of compact TES infrastructure, which leads to a low initial cost of insulation material. Water can be pressurized [27] or mixed with nitrogen gas, which increases the boiling point up to 120°C [25], to prevent vaporization of water.

Heat Exchanger System Design

The heat exchanger system consists of the engine block water jacket, cylinder head with embedded coolant channels, and standard heat exchanger.

In a standard ICE, water jackets inside the engine block allow coolant to flow and dissipate excessive heat through radiators. For this project, since there is no combustion involved, the cylinder temperature is relatively low. Thus, water can be pumped into the water jacket to maintain a safe system temperature and carry out excessive heat (otherwise wasted) to the heat exchanger system. Based on the cylinder head structure previously proposed, a new cylinder head design along with embedded coolant channels is proposed, as shown below in Figure 5.1.

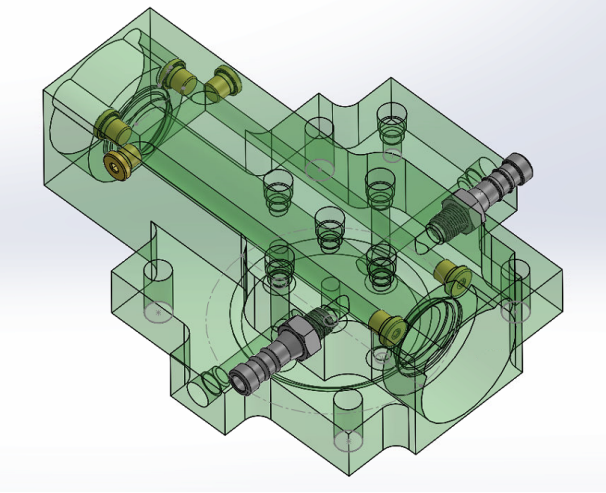

Figure 5.1: Cylinder head design with embedded coolant channels

Water can flow through the U-shape coolant channel and extract heat generated under the AC mode from the cylinder head and rotary valve. Under AM mode, water can be pumped back into the cylinder head to maintain cylinder head temperature. For the heat exchanger, an off-the-shelf heat exchanger can be used since the water/air temperature is considerably low. For this project, a standard counter-flow heat exchanger is selected due to its reliability and efficiency.

5.1.2 TES System Modelling

GT-Suite Modelling

The TES system is modeled in GT-Suite, as shown in Figure 5.2. The flow volume of the cylinder head coolant channels and water jackets is extracted and converted into GT-Suite models using GEM3D. The cylinder head, piston, valves, cylinder are modeled using the parametric finite element method, which is used when the cylinder is connected to coolant and/or oil flow circuits.

The heat exchanger performance is modeled based on the air/water mass flow rate, inlet temperature, pressure, pressure loss, and heat transfer coefficient published by the manufacturer. Table 5.1 shows the partial heat exchanger data used to generate a look-up table of the overall Nusselt number, Nu, as a function of air and water Reynolds number, Re, in GT-Suite. In total, there are more than 200 data entries entered into GT-Suite.

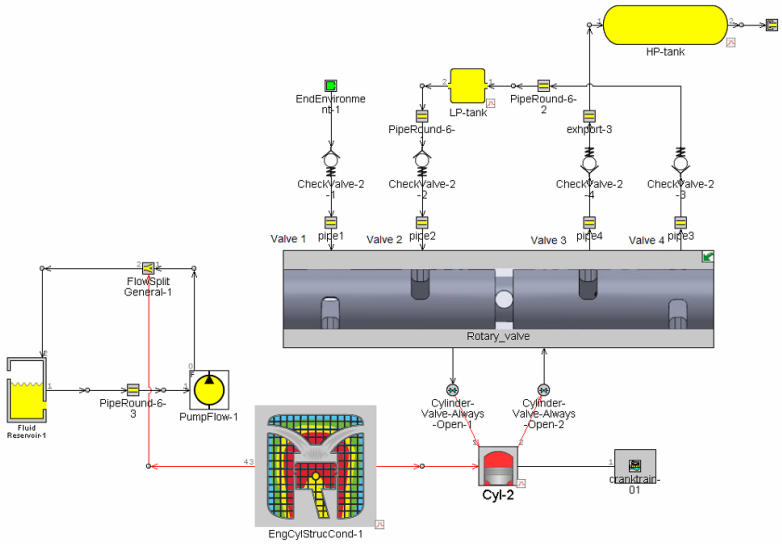

Figure 5.2: Cylinder head modeled in GT-Suite

Simplified Heat Exchanger Model

A simplified heat exchanger model is derived to reduce simulation time. The heat exchanger is modeled using the Number of Transfer Units (NTU) Method [56]. Essentially, the heat exchanger performance is described by the heat exchanger efficiency, which is a function

Table 5.1: Heat exchanger data. The default units are [°C], $[psi, a]$, $[L/min]$ and [W]

$T_{air,in}$	$P_{air,in}$	Q_{air}	$T_{water,in}$	$P_{water,in}$	$Q_{water,in}$	h
50	400	10	100	15	10	239
50	400	30	100	15	10	729
80	400	10	100	15	20	88
80	400	30	100	15	20	267
100	150	10	50	15	10	80
100	150	30	50	15	10	233
100	150	40	50	15	10	306
100	150	50	50	15	10	386
155	200	10	100	23	10	102
155	200	30	100	23	10	298

of air/water mass flow rate, inlet temperature and pressure. Compared to the GT-Suite model, the simplified model assumes the pressure loss of air/water caused by the wall shear stress is relatively small and can be neglected. If there is a large difference between the air inlet temperature and water inlet temperature (larger than 70°C), the potential thermal stress problem is not considered in the simplified model.

5.1.3 TES System Control

The water inside the TES system is driven by a pump. The pump flow rate is updated based on the cylinder outlet air temperature. Under AC mode, the pump flow rate is shown in Figure 5.3. Under AM mode, a higher pump flow rate is used to heat the air before entering the cylinder.

At the pump flow rate of 10 [L/min], the pump power is only 5W under AC mode. Under AM mode, the power generated (engine brake power) is much larger than the pump power. Thus, it is reasonable to neglect the pump power in this analysis.

Using the pump flow rate listed in Figure 5.3, GT-Suite simulation is run with auto shut off when steady state turned on. The result, in Figure 5.4, shows that the HP tank average air inlet temperature under AC mode is maintained at roughly 160°C.

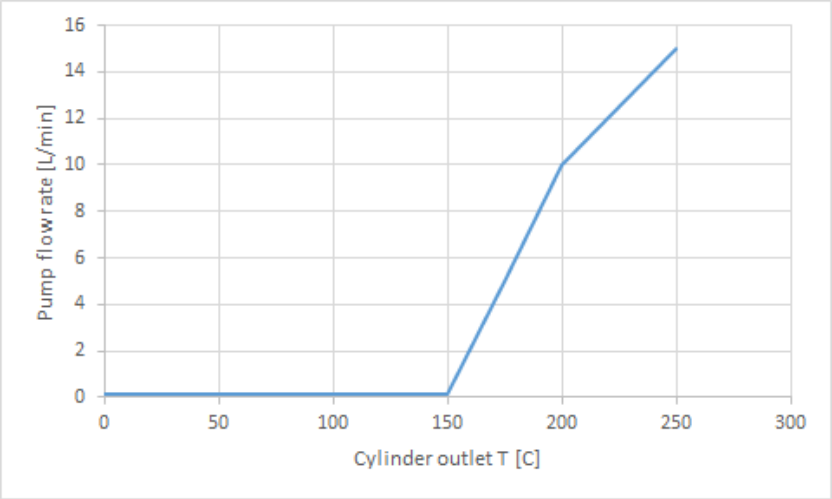

Figure 5.3: Pump flow rate vs cylinder outlet temperature

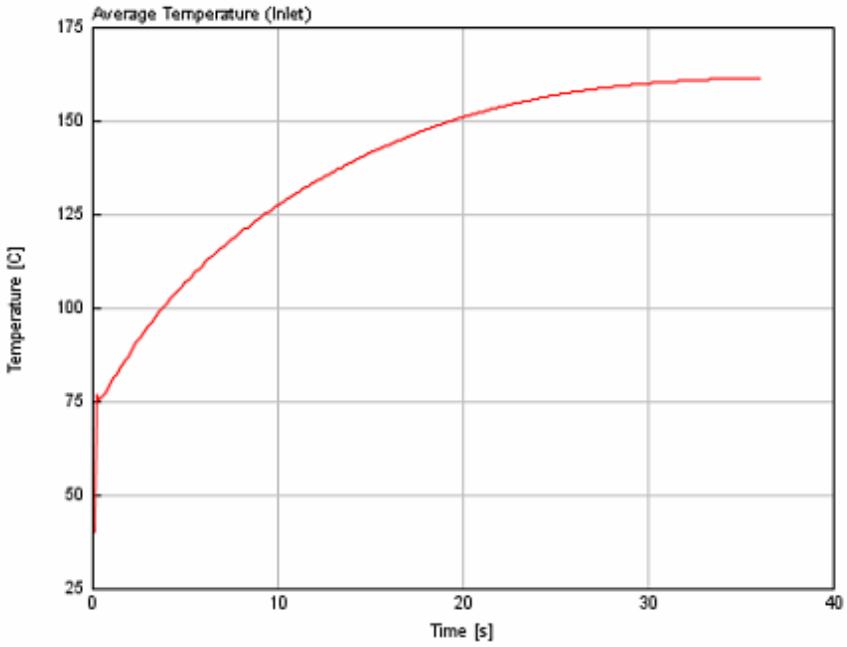

Figure 5.4: HP tank average air inlet temperature

5.1.4 Compressed Air Storage Device

For this project, a steel air tank is used as the compressed air storage device (HP tank). It is assumed that the storage device is built with phase-change material which will absorb the heat generated during the compression process and release the heat later in the expansion process [25]. The air storage process can be assumed to be near-isothermal or isothermal.

5.2 Air Motor Braking Power Control

The indicated power and brake power are key indicators of air motor performance. In this section, an MVM is derived to estimate the system's indicated/brake power under AM mode. A PID controller with lookup table is developed to regulate the brake power.

5.2.1 Mean Value Model

A MVM for a SI engine estimates the engine performance using mapped functions of airflow rate (engine volumetric efficiency), indicated power (indicated mean effective pressure) and exhaust gas energy (exhaust gas temperature). Since there is no combustion involved in the system under AM mode, the engine indicated power is independent of the fueling dynamics and can be estimated using the cylinder flow dynamics and the cranktrain dynamics. Therefore, the system under AM mode can be modeled as a steady-state adiabatic expander receiving air and expanding it based on the expansion ratio. The engine indicated power can be estimated by:

$$P_{indicated} = \eta \ \dot{m}_{eng} C_p T_{inlet} \left[1 - \left(\frac{P_{out}}{P_{in}} \right)^{\gamma - 1/\gamma} \right] \tag{5.2}$$

The efficiency term, η, is added since the system under AM mode doesn't have constant inlet flow rate due to the reciprocating motion. The brake power is defined as :

$$P_{brake} = P_{indicated} - P_{fric} \tag{5.3}$$

The frictional power, P_{fric}, is predicted using the Chen-Flynn engine friction model as mentioned in Equation 3.26. The mass flow rate to the engine, $\dot{m}_{eng}$, is calculated based on inlet manifold pressure and cylinder instantaneous pressure using the orifice equations 3.29

and 3.30. The throttle is modeled as an orifice, and the effective flow area and discharge coefficient are updated based on the steady-state simulation of a throttle in GT-Suite. Compared to the GT-Suite model used in Section 4.3.2, the initial air pressure in this analysis is increased to 195 [psi,a], and an inlet diameter of 10 mm is used to increase the engine brake torque/power.

To verify the MVM developed, a throttle angle signal, shown in Figure 5.5 (a), is applied to the detailed model in GT-Suite and its MVM in Simulink. The MVM parameters such as η and cylinder volumetric efficiency map are obtained from GT-Suite detailed model.

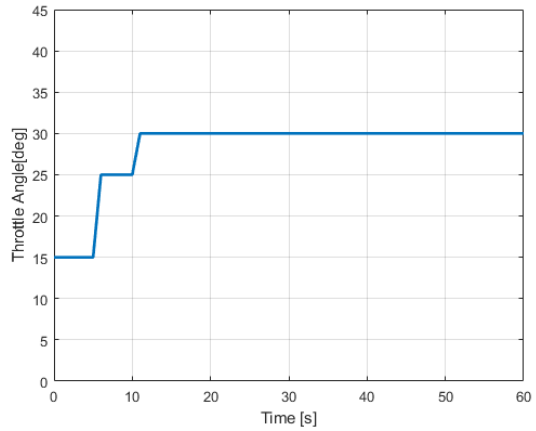

(a) Throttle angle

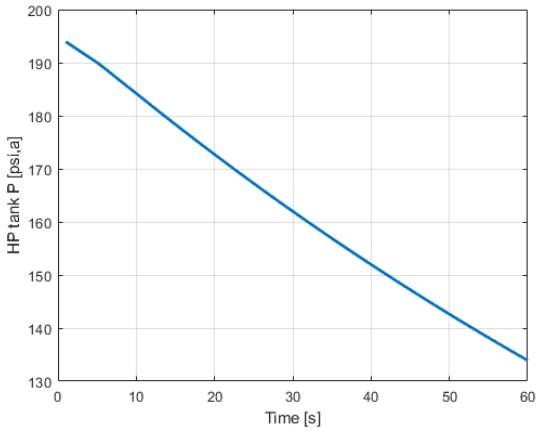

(b) HP tank pressure

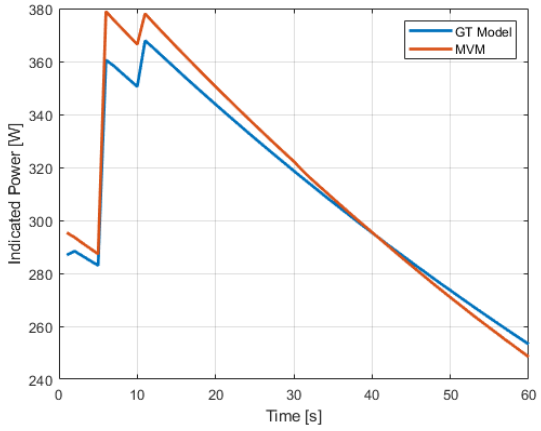

(c) Indicated power

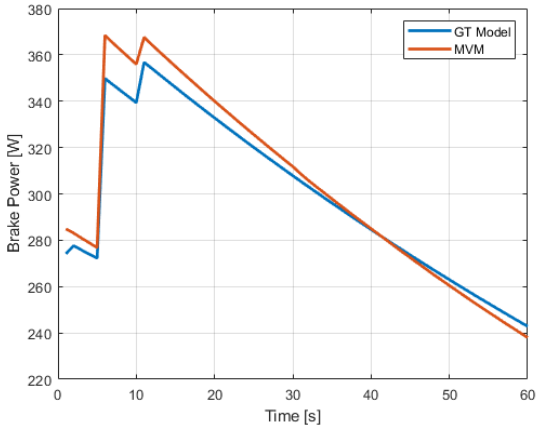

(d) Brake power

Figure 5.5: (a) Throttle angle (b) HP tank pressure (c) Indicated power (d) Brake power

Figure 5.5 (b) shows the HP tank pressure with respect to time. The indicated power and brake power obtained from the MVM are filtered and compared with the average indicated power and brake power reported in the GT-Suite model, as shown in Figure 5.5 (c) and (d). As can be seen, there is a good agreement between the detailed model in GT-Suite and MVM. However, a non-negligible difference between engine indicated/brake power obtained from GT-Suite and MVM can be seen at t=5 and 10 s when the throttle signal changes. The discrepancies between the detailed model and MVM can be explained as follows:

- For the GT model, the engine indicated power is calculated by integrating the P-V diagram. In the MVM, the process is modeled as adiabatic expansion where the power generated or consumed during the compression stroke or when the piston is at TDC/BDC in the actual process is neglected.
- MVM is an average model and instantaneous fluctuations in mass flow rate when the throttle angle changes are neglected.
- The friction power term in MVM is calculated based on the Chen-Flynn model in Equation 3.26. Ideally, friction torque/power should be mapped using crankshaft speed, instantaneous cylinder pressure and inlet manifold instantaneous pressure.

5.2.2 Brake Power Control

Fazeli derived a mean value model (MVM) for the Regenerative Braking in [57]. In order to control the regenerative braking torque, he developed an adaptive sliding mode controller (ASMC) and compared its performance to a smooth sliding mode controller (SMC) and a model-free lookup table/ high gain PID controller [4].

Using the MVM developed, assuming constant engine speed, brake power control is achieved using a tuned PID controller with parameters shown in Table 5.2. Figure 5.6 shows the closed-loop controller structure. For the feed-forward part of the controller, the throttle angle is calculated using the desired average mass flow rate generated from the desired braking power, engine speed, HP tank pressure and temperature. For the feedback part, the brake power error is sent into the PID controller. The desired throttle signal from the PID controller is sent to the throttle dynamics block, and a regulator is used to limit the range and rate of change of the throttle signal.

The controller is set to track a constant brake power of 200 W at an engine rotational speed of 60 RPM. The initial throttle angle is set to 8 °, and the controller is activated

starting at t=1 [s]. The throttle angle, brake torque response along with the HP tank temperature and pressure are shown in Figure 5.7.

Table 5.2: Controller's Parameters

PID controller	Gain Value
Proportional gain	10
Integral gain	3.5
Derivative gain	0.3

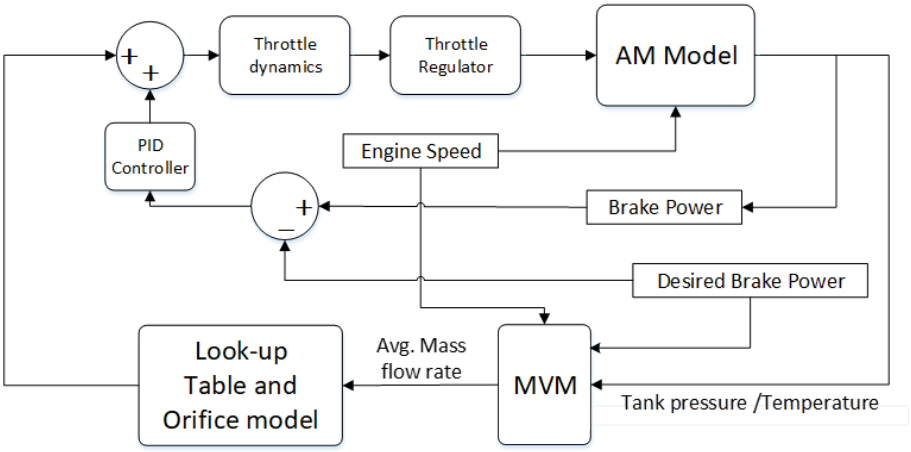

Figure 5.6: Brake power Controller Structure

In Figure 5.7 (a) and (b), HP tank pressure and temperature drop due to airflow from the HP tank to the cylinder as expected. At the beginning of the simulation, large brake power is observed due to high HP tank pressure and temperature. In Figure 5.7 (c) and (d), the PID controller takes these into account and reduces the throttle angle to 7 ° at t=4 [s] which causes the brake power to drop from 233.54 W at t=2 [s] to 200 W at t=10 [s]. After this, the throttle angle increases to compensate for dropping HP tank pressure, temperature and maintains the desired brake power of 200 W.

The tracking error percentage of the PID controller is calculated and shown in Figure 5.8. Despite the large oscillations from t=1 [s] to t=10 [s], overall, the controller is able to maintain the brake power near the desired 200 W. Specifically, the controller's maximum tracking error after t=10 [s] is -0.17 % at t= 30 [s], which corresponds to a difference of 0.34 W.

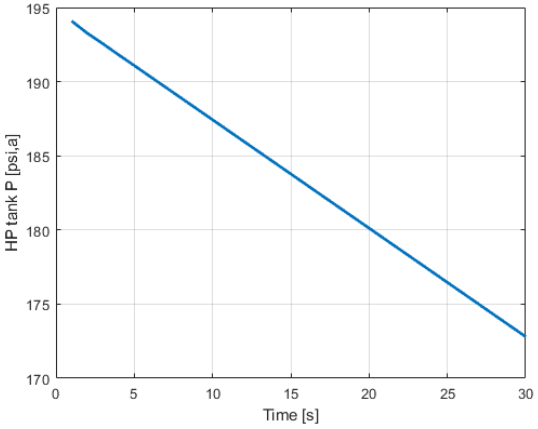

(a) HP tank pressure

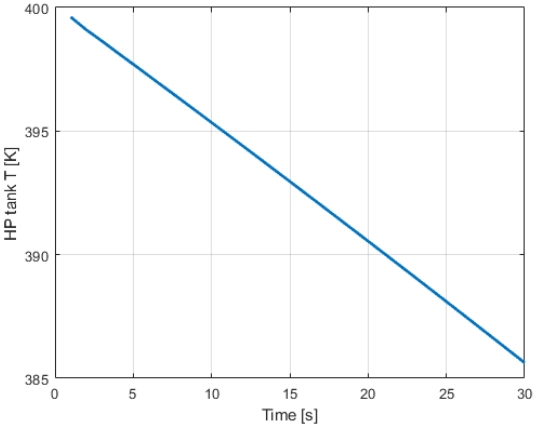

(b) HP tank temperature

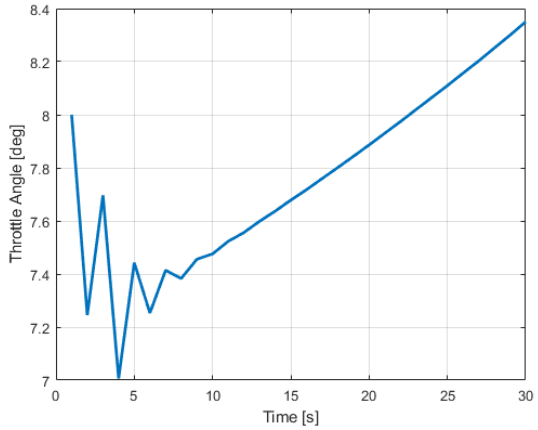

(c) Commanded throttle angle

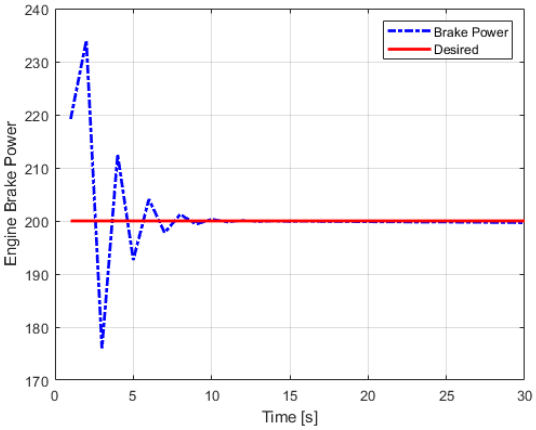

(d) Brake power

Figure 5.7: (a) HP tank pressure(b) HP tank temperature (c) Throttle angle (d) Brake power and desired brake power

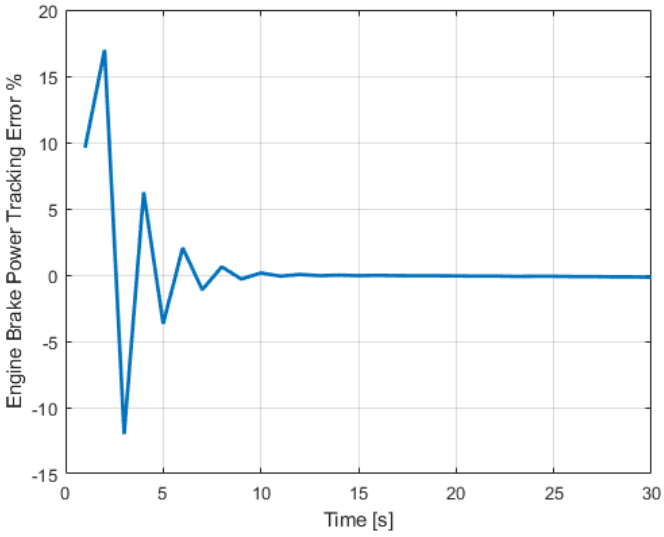

Figure 5.8: Brake power tracking error

The tracking error after t=10 [s] is mostly due to following reasons:

- The instantaneous fluctuations in mass flow rate when the throttle angle changes are neglected.
- In the Chen-Flynn model, friction is a function of the mean piston speed and peak cylinder pressure. The disturbance caused by the reduction of the friction (due to dropping HP tank pressure) leads to uncertainties of the brake power signal sent to the feed-forward part of the controller. In the future, the disturbance can be compensated using a robust controller.

5.3 Summary

In this chapter, a detailed ACAES system with a separate TES was designed in Section 5.1. An MVM was derived to predict the AM brake power, and a PID controller combined with a lookup table was developed in Section 5.2. Based on the simulation results, the PID controller was able to track a desired brake power signal accurately with a maximum tracking error of -0.17%. In the following chapter, the proposed ACAES system is analyzed and optimized.

Chapter 6

Analysis and Optimization

The proposed ACAES system is analyzed and optimized in this Chapter. Section 6.1 introduces the necessary constraints, assumptions, and the definition of the round-trip efficiency used for performance evaluation. The ACAES system under AC and AM mode without the TES system is analysed and optimized in Section 6.2 and 6.3. Section 6.4 evaluates the TES system performance under AC and AM mode. The optimized system is compared with the baseline system in Section 6.5. Section 6.6 summarizes the chapter and provides some concluding remarks.

6.1 Constraints and Performance Evaluation

6.1.1 Constraints and Assumptions

Based on the ACAES system design in Section 5.1, several constraints/assumptions should be clarified before the analysis and optimization.

- Since the system models were derived from the experimental system, the overall system structure should be preserved. This means that the air compression is a single-stage process with the novel double-tank compression strategy. For the expansion stage, the system is run under the AM mode to generate electricity.
- The overall rotary valve structure should remain fixed. The rotary valve timing can be modified, but the same timing is used across all rotational speeds. However, since Fazeli proposed different valve timings for AC and AM mode, the valve timing can be changed.

- The drive motor efficiency is ∼98% and can be assumed to be 100%. For the generator, the efficiency is assumed to be 100% for this analysis.

6.1.2 Performance Evaluation

Since there are many performance indexes for the ACAES system, for this project, the system performance is evaluated based on the efficiencies and defined below:

For the air compression process, the electricity to exergy efficiency, $\eta_{Elect\_to\_Ex}$, is calculated by dividing the exergy change by the total electricity input. Similarly, the air motor exergy to electricity efficiency, $\eta_{\ Ex\_to\_Elect}$, is defined as the ratio of the electricity generated by the change of air exergy. The system round trip efficiency is the product of $\eta_{Elect\_to\_Ex}$ and $\eta_{\ Ex\_to\_Elect}$. Mathematically, the efficiencies can be calculated using the following formulas.

$$\eta_{Elect\_to\_Ex} = \frac{\Delta B_{AC}}{E_{elect,in}} = \frac{B_{air_{final}} - B_{air_{ini}}}{\int P_{BP} dt} \tag{6.1}$$

$$\eta_{Ex\_to\_Elect} = \frac{E_{elect,gene}}{\Delta B_{AM}} = \frac{\int P_{BP} dt}{B_{air_{final}} - B_{air_{ini}}} \tag{6.2}$$

Under AC mode, the heat exchanger performance is governed by the compressor outlet pressure, mass flow rate, and temperature. The heat exchanger under AC mode is evaluated based on the air outlet temperature or HP tank average temperature. Under AM mode, the heat exchanger performance is assessed by the cylinder inlet air temperature.

6.2 AC mode

The ACAES system under AC mode is analyzed and optimized. The effects of LP tank size, compression ratio are studied in Section 6.2.1 and 6.2.2. In Section 6.2.3, the steady-state avoidance and HP tank sizing is presented. The rotary valve timing is optimized in Section 6.2.4.

6.2.1 LP Tank Size

The LP tank steady-state pressure was discussed in [1], but the effect of LP tank size was not included. Thus, the system under AC mode with five standard tank sizes ranging from

0.22L to 2L is simulated in GT-suite. The HP/LP tank pressures from the simulation are shown in Figure 6.1 and 6.2.

The simulation results show that increasing the LP tank size slows the increment of the LP tank pressure. For the HP tank pressure, changing the LP tank size doesn't exhibit a significant impact. Since the final HP pressures/temperatures are in similar ranges for all tank sizes, the LP tank size used in the experimental analysis will remain unchanged at 0.5 L.

6.2.2 Compression Ratio

For a standard compressor, the outlet pressure is related to the inlet pressure by the compression ratio. For the experimental system under AC mode, the compression ratio was reduced from 8.5 to ∼7.2. The effect of the compression ratio on the AC mode efficiency is studied via simulations run in GT-Suite. The simulation result, shown in Figure 6.3 and 6.3 , shows that with a higher compression ratio, the HP tank pressure increases much faster as expected, while the LP tank pressure increases more slowly particularly at a C_r of 20.

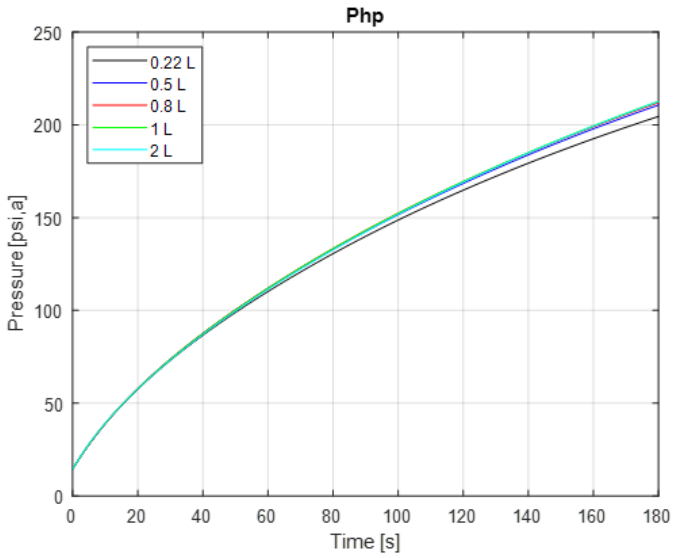

Figure 6.1: HP tank pressures for different LP tank sizes

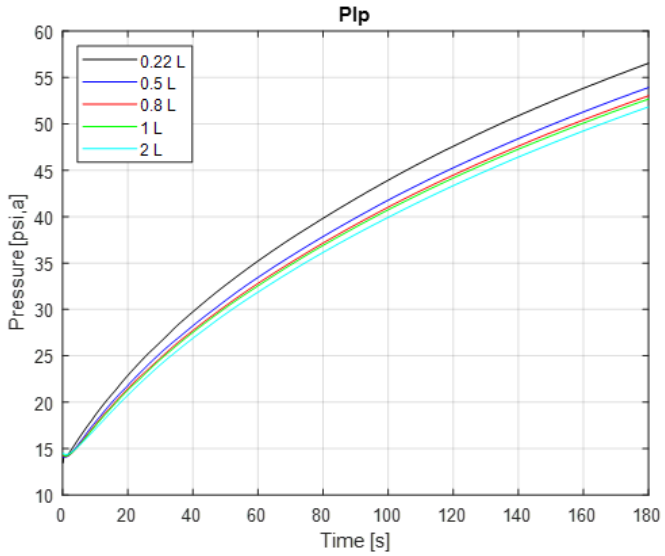

Figure 6.2: LP tank pressures for different LP tank sizes

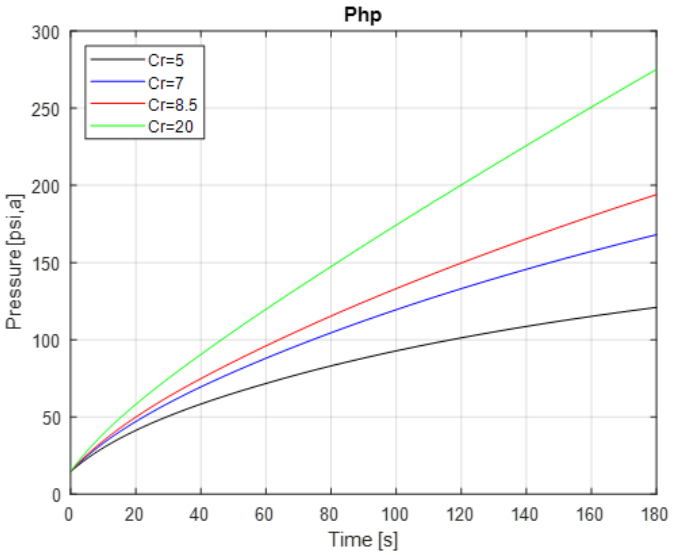

Figure 6.3: HP tank pressures for different compression ratios

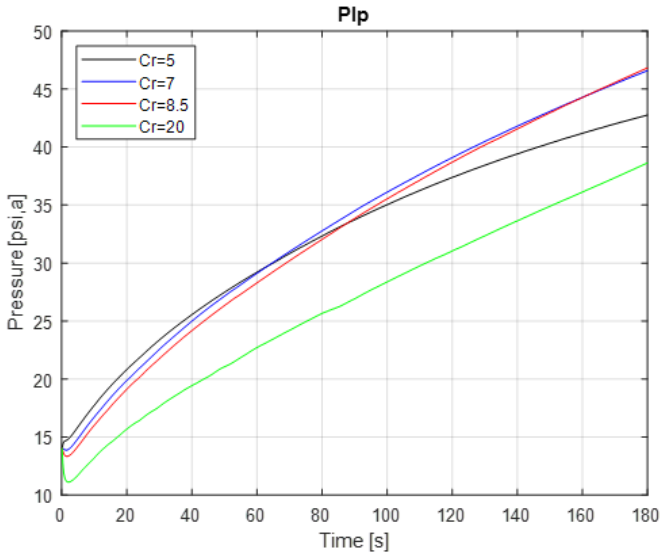

Figure 6.4: LP tank pressures for different compression ratios

The efficiencies of the system with different compression ratios are compared in Table 6.1. Increasing the compression ratio from 5 to 20 improves the exergy efficiency from 19.22 % to 28.07 %. A compression ratio of 8.5 is selected due to higher exergy efficiency and feasibility. The problem with a compression ratio of 20 is that the compressor outlet air temperature can reach 412.48°C, which results in significant energy loss due to heat transfer.

Table 6.1: Compression ratio efficiency calculation

Compression ratio	5	7	8.5	20
Total energy input:	88.56 KJ	121.45 KJ	138.07 KJ	177.75 KJ
HP tank exergy change:	17.03 KJ	26.38 KJ	32.27 KJ	49.90 KJ
AC efficiency:	19.22 %	21.72 %	23.37 %	28.07 %

6.2.3 Steady-state Avoidance

In Fazeli's double-tank compression strategy [51], when the double-tank compression system reaches the steady-state, the steady-state HP and LP tank pressures are:

$$P_{LP} = P_{atm} C_r$$

$$P_{HP} = \frac{P_{atm}V_{cyl} + P_{LP}V_{LP}}{V_{cyl} + V_{LP}} {C_r}^{\gamma}$$

Under steady-state conditions, the HP and LP tanks are full, and no additional air can be stored. This condition should be avoided such that the system can operate efficiently through the compression process. The system under AC mode with different HP tank sizes (10 L and 100 L) are simulated for 3600 [s] and compared below. 6.5 shows the HP/LP tank pressure with an HP tank of 10L. After ∼1000 [s], the LP approximates the steady-state pressure of ∼7.2 bar, and the HP pressure eventually reaches the steady-state pressure of 48 bar. This result matches the steady-state HP/LP tank pressures since the cylinder compression ratio was reduced from 8.5 to ∼7.2 due to the additional volume of the pipe fittings, pipes, and cylinder head.

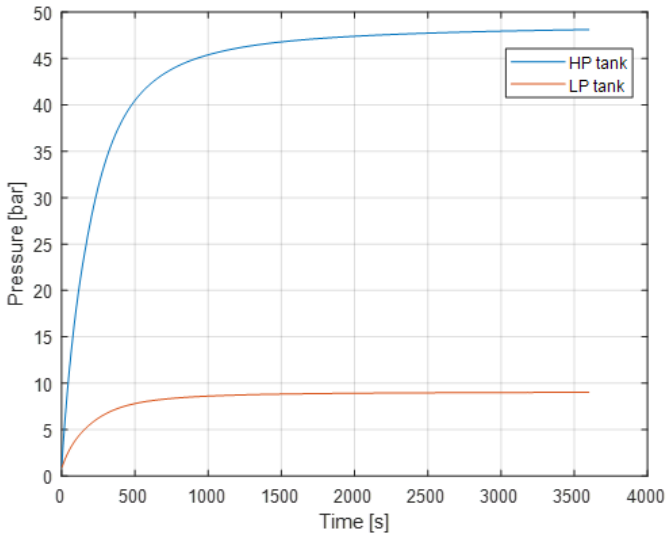

Figure 6.5: Air compression with a 10L HP tank

In Figure 6.6, the HP tank pressure reaches ∼36 bar at t=3600 [s] while the LP tank pressure reaches ∼7 bar at the end of the simulation. By comparing with Figure 6.5, the system with a 100L HP tank doesn't reach the steady-state condition. Since the final steady-state pressure is fixed with a maximum storage temperature of 200°C, the compressed air's energy density can be calculated based on the CAS volume. Depending on the amount of energy to be stored, the HP tank volume can be sized accordingly. In practice, the HP tank can be over-sized by a factor of 1.1 to prevent the system from reaching steady-state during the entire compression process.

In the physical system, real-time steady-state avoidance can be achieved using air flow rate sensors (placed at compressor inlet and outlet). The outlet air should be further cooled using a secondary heat exchanger before measuring the flow rate. This is because the compressed air can reach up to 160°C even after passing the primary heat exchanger, as shown in Figure 5.4.

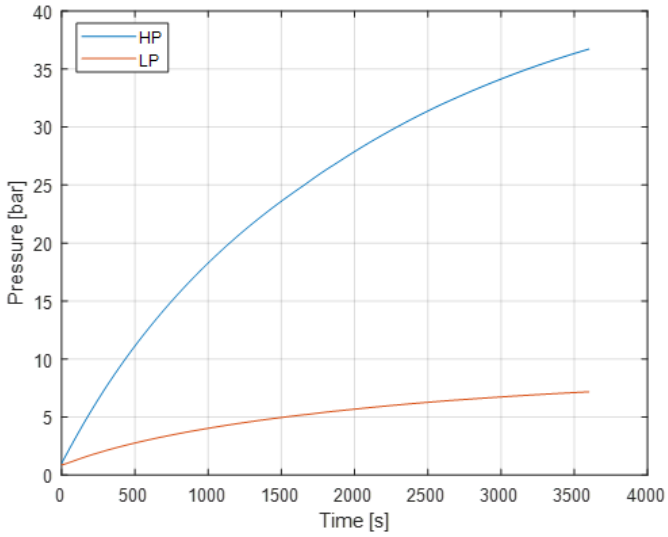

Figure 6.6: Air compression with a 100L HP tank

6.2.4 Muti-Objective Optimization

Background

Genetic algorithm (GA) is a probabilistic global search and optimization method that is analogous to natural evolution [58]. GA performs on a population of feasible solutions (within the constraints), each of which is an encoding string (chromosome), containing the decision variables (genes) by three operators: selection, crossover, and mutation [59].

Optimization

For the ACAES system under AC mode, the valve timing proposed by Fazeli is used up till now. However, after changing the rotary valve's valve timing in the previous prototype (Section 4.1), the final HP tank pressure was improved by 56.52% (from 115 [psi,a] to 180

[psi,a]). This improvement shows that the rotary valve timing has a significant impact on the system performance under AC mode. Therefore, multi-object optimization is used to optimize the rotary valve's timing. Among all the optimization methods available, GA is selected since it represents an intelligent exploitation of a random search in the solution space rather than a conventional gradient-based procedure [58]. The Pareto genetic algorithm is used to deal with multiple objectives [60].

The optimization objectives are to maximize the mass flow rate into the HP tank (similar to the LP to HP tank mass flow rate used in [42]), cylinder volumetric efficiency, and the HP tank pressure. The optimizing factors are the valve opening angles (integers only) of four ports on the rotary valve, which correspond to the Intake/ Cylinder (CY) to HP/ CY to LP/ LP to CY timings. For the sake of simplicity, a constant valve opening duration of 180° is used. The valve closing timings are not optimized in this analysis because the number of simulations would increase from 1600 to 4000. Also, since there is no variable valve timing (VVT) device available for the rotary valve design, valve timing is assumed to be fixed across all rotational speeds. The valves are allowed to advance or delay for up to 15 °CA.

Thus, multi-object optimization using Pareto GA is run in GT-Suite for air compression at 500 RPM with the following constraints:

- HP tank temperature is less than 200°C.
- The end seals are rated for up to 100°C.

Table 6.2 shows the Pareto designs that are considered equally valid based on the objectives. The sensitivity analysis of the optimizing factors on the objectives are listed in Table 6.3 .

By comparing the current valve timing and those generated using Pareto GA, the CY to LP opening angle can be advanced for up to 5° CA. The LP to CY valve can open as early as 15°CA before BDC, while the cylinder to HP valve should open 2-5°CA after BDC. For the intake, the results from the optimization agree with opening the intake at TDC. However, with ten repeated intake opening angles, additional optimizations should be run, and the intake valve should be constrained to open 30°CA before or after TDC.

The sensitivity analysis shows that CY to HP opening angle is the most important factor for HP tank pressure and mass flow rate into the HP tank. For the cylinder volumetric efficiency, the CY to LP and LP to CY timings are relatively more important since the air stored in the LP tank is used to charge the cylinder for the next cycle. For this optimization, the Pareto design case 6 is selected since the steady-state HP tank pressure is the highest among other valve timings listed in Table 6.2. To further optimize the valve timing, the

multi-objective optimization should be repeated across different engine rotational speeds, and the valve closing angles should be optimized.

Table 6.2: Pareto designs of valve opening timing [CA]

Case	Intake open	CY to LP Open	LP to CY open	CY to HP-Open
Current	0	350	180	180
1	0	348	170	183
2	0	346	172	182
3	0	349	170	183
4	0	348	165	185
5	0	344	166	182
6	0	348	165	184
7	0	344	165	185
8	0	348	166	184
9	0	346	171	185
10	0	344	172	182

Table 6.3: Sensitivity analysis of optimizing factors on the objectives

	Intake open	CY to LP Open	LP to CY open	CY to HP-Open
P_{hp}	0.167	0.105	0.226	0.501
Volumetric efficiency	0.140	0.475	0.279	0.103
Mass flow rate	0.266	0.221	0.021	0.492

6.3 AM mode

A steady-state simulation is run in GT-Suite to analyze cylinder pressure and brake torque within a crankshaft revolution. In Section 6.3.2, GA is used to optimize the valve timing to maximize brake power.

6.3.1 Steady-state Simulation

Assuming constant HP tank pressure and temperature, a steady-state AM mode simulation at 60 RPM is run in GT-Suite. Figure 6.7 and 6.8 show the steady-state crank train brake

torque and cylinder pressure in one crankshaft revolution.

For the cylinder pressure, roughly 5° after TDC, the cylinder pressure increases to tank pressure. After BDC, the exhaust valve opens, and the pressure drops to atmospheric pressure at $\sim 5°$ before TDC. For the brake torque, the maximum brake torque is obtained at $\sim 90°$ CA. However, the brake torque drops below 0 from ~ 180 °to ~ 360 ° CA. This issue is expected because the high-pressure air trapped within the cylinder undergoes a compression process from BDC to TDC due to the reciprocation motion. With low HP tank pressure, the cycle average brake torque could drop below zero. This problem can be improved using the methods listed below:

- Adding extra cylinders to the crank train would allow a smooth brake torque profile within a crank train revolution.
- Optimize the valve timings to reduce the trapped air or maximize the average brake torque
- Adding a throttle controller (as mentioned in Section 5.2.2) to regulate the inlet airflow.

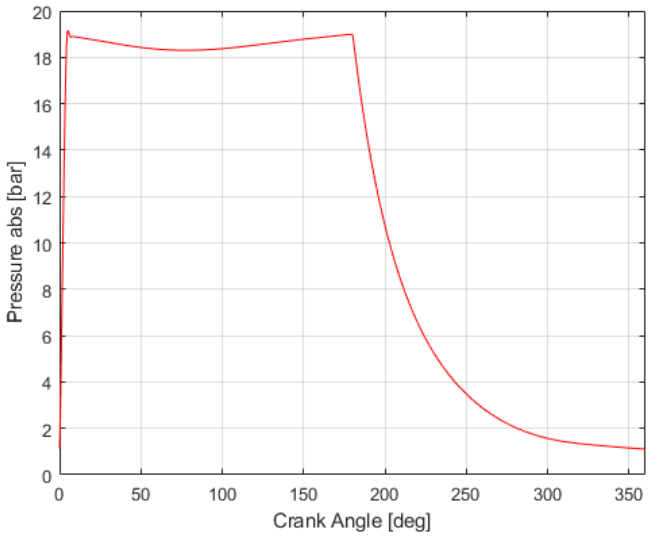

Figure 6.7: Cylinder pressure

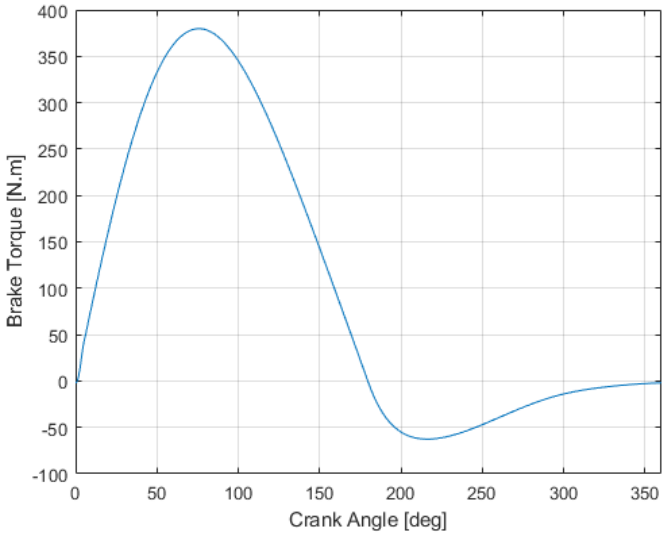

Figure 6.8: Steady-state cranktrain brake torque

6.3.2 Genetic Algorithm

For the AM mode, the rotary valve timing is optimized to maximize brake torque using GA. Since there are essentially only two opening and closing valves, the GA is coded in MATLAB/Simulink, and the brake power is evaluated using the steady-state AM model in GT-Suite. GA parameter and constraints are listed in Table 6.4. The overall structure is similar to the MATLAB-Simulink and GT-Suite coupling model-based GA structure used by Li to optimize valve timings [61, 62].

Table 6.4: GA parameters and constraints

Crossover rate	0.8	Inlet Open [CA]	-20° - 20 °
Population size	16	Inlet close [CA]	160° - 200 °
Number of generations	15	Exhaust Open [CA]	160° - 200°
Mutation rate	0.1	Exhaust close [CA]	-20° - 20 °

The convergence of the CY to atm valve (essentially exhaust valve) opening angle and average brake torque during GA operation are shown in Figure 6.9 and 6.10, respectively. From Figure 6.9, the CY to atm valve opening angle follows the constraint and converges to ∼200° at the end of the optimization.

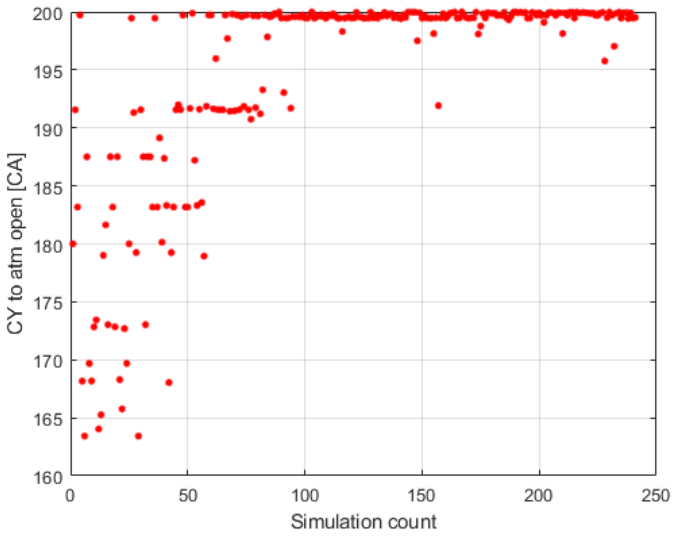

Figure 6.9: Convergence of the CY to atm open angle

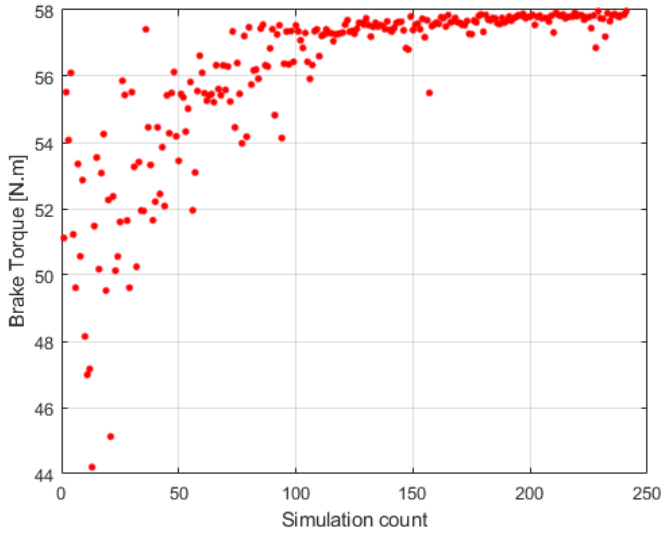

Figure 6.10: Convergence of the average brake torque

The final result of the GA optimization is compared to the original valve timing proposed by Fazeli in Table 6.5. From the optimization, the intake valve opening angle should

advance 8°, and the closing angle should be delayed by 18.5°. For the CY to atm valve, it should open right after the intake valve closes and close 9° after the TDC. Based on this analysis, the AM average brake torque improves by 13.38%, which means the brake power increases by the exact percentage.

Table 6.5: GA result comparison

-	Current	Optimized
Intake open [CA]	0	-8
Intake close [CA]	180	198.5
Exhaust open [CA]	180	199.5
Exhaust close [CA]	0	9
Average brake torque [N.m]	51.12	57.96

6.4 TES System

6.4.1 AC mode

The TES system design is evaluated here. The cylinder head circuit and the heat exchanger circuit are combined and operated by a single pump, as shown in Figure 6.11.

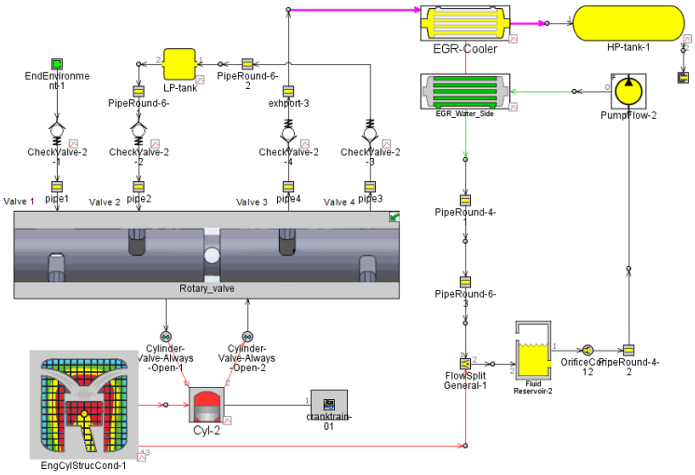

Figure 6.11: TES system layout

Based on simulation result shown in Figure 6.12, the HP tank temperature could reach $\sim$ 135°C, which is within the designed air storage temperature.

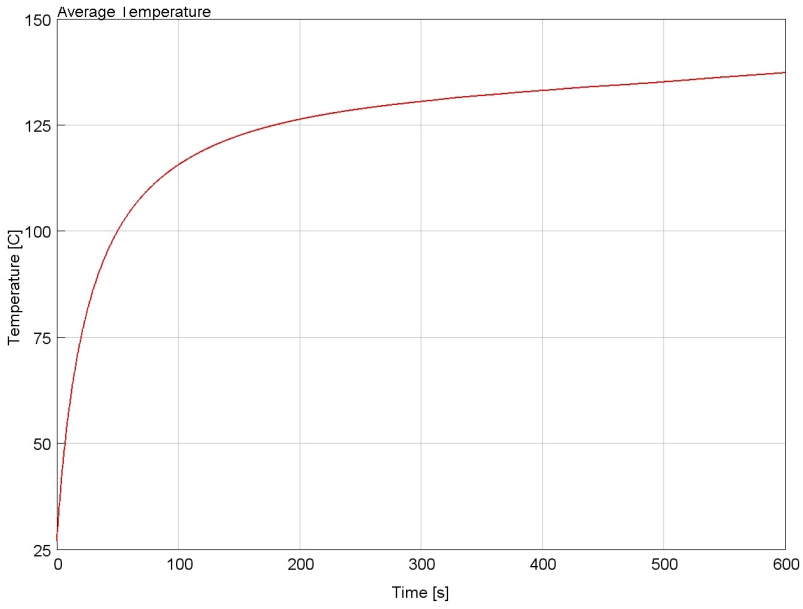

Figure 6.12: HP tank average temperature [°C] v.s Time [s]

6.4.2 AM mode

Under AM mode, if the water temperature is below the inlet air temperature, the heat exchanger will extract heat from inlet air. The simulation results are shown in Figure 6.13 and 6.14. Even though the initial water temperature is only $\sim$40°C in this simulation, the same problem will happen as long as the air inlet temperature is higher than the water temperature. This issue can be solved by disconnecting the heat exchanger from the air circuit to prevent heat loss. A flow control system can be designed to reduce the heat loss by connecting/disconnecting the heat exchanger from the airflow path, adjusting the pump flow rate, and switching the water flow paths. The water flow path can be changed by isolating the head coolant circuit from the TES system using flow control valves.

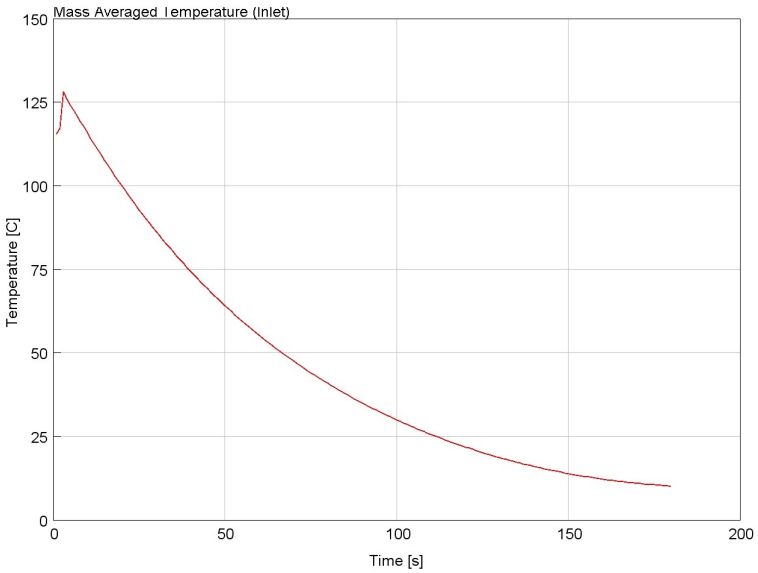

Figure 6.13: Heat exchanger inlet air temperature vs time

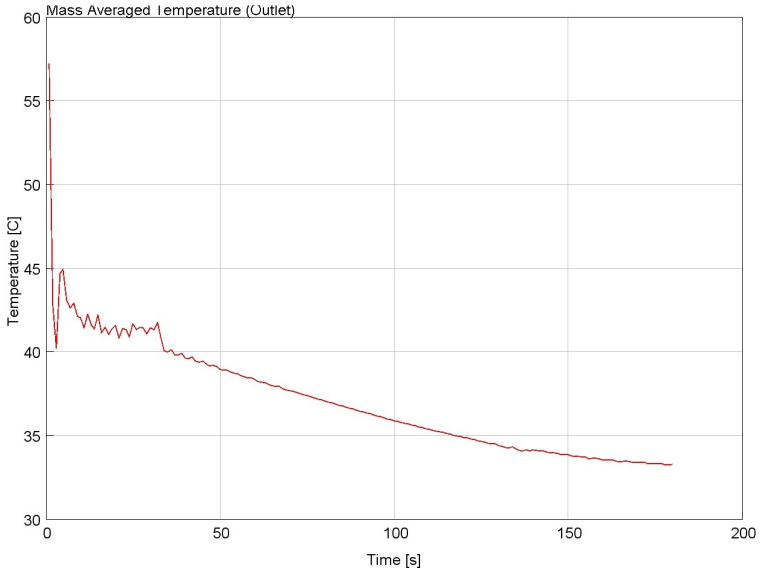

Figure 6.14: Heat exchanger outlet air temperature vs time

6.5 Simulations and Comparison

6.5.1 Drive Cycle Analysis

According to current literature, almost all the existing studies on ACAES drive cycle analysis are based on the assumption of full power compression/expansion. For this project, constant power (1KW) compression causes the crankshaft to accelerate to 3000 RPM and reduces the cylinder volumetric efficiency below 0.1. Thus, for the simulations below, the system under AC or AM mode is held at a constant speed. The system input power is the crank train brake power under AC mode. Under AM mode, the power generated is exactly the crank train brake power.

6.5.2 Baseline System

AC mode

The AC mode simulation is run using the parameters listed in Table 6.6. The HP tank pressure and brake power obtained from the simulation are shown in Figure 6.15 and 6.16. The brake power is integrated numerically to obtain the total energy input to the system. The HP exergy change is calculated based on initial/final pressure and temperature. The AC efficiency is evaluated in Table 6.7.

Table 6.6: Simulation parameters

Parameter	Value
Engine speed	500 RPM
Number of cylinder(s)	1
HP tank volume	30 L
LP tank volume	0.5 L
Compression raito	7.2
Initial Pressure	1 atm
Initial Temperature	300 K
Air intake diameter	6 mm
AC duration	10 mins

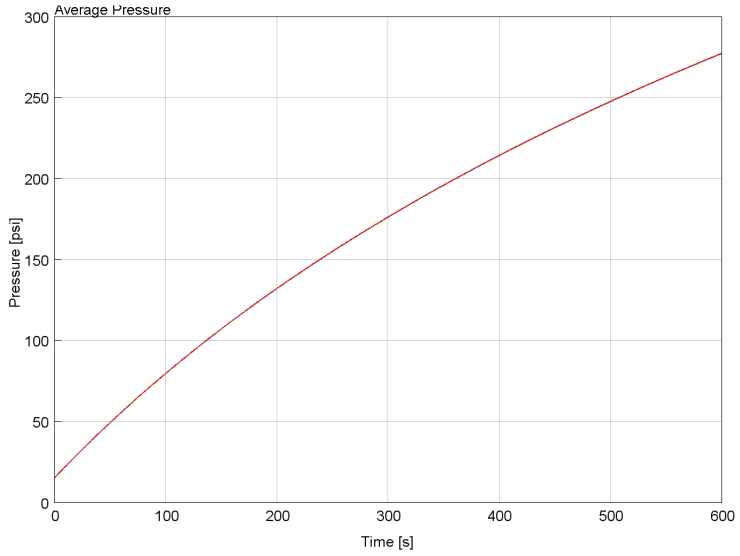

Figure 6.15: AC mode HP tank pressure vs time (baseline system)

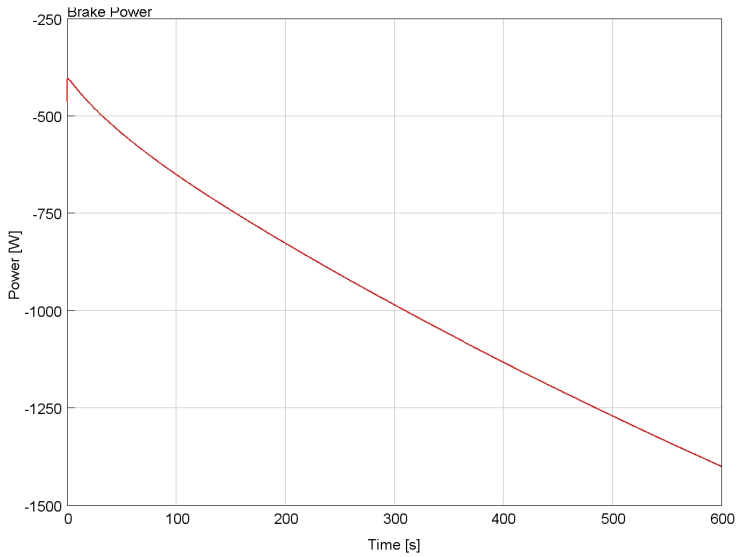

Figure 6.16: AC mode Brake power vs time (baseline system)

Table 6.7: AC efficiency calculation

Total energy applied to the system:	578.67 KJ	-
HP tank exergy change:	131.14 KJ	22.66 %
Energy lost due to friction:	57.10 KJ	9.87%

The electricity to exergy efficiency, $\eta_{Elect\_to\_Ex}$, is 22.66% which is close to the 21% reported by Fazeli in his thesis [1]. $\eta_{Elect\_to\_Ex}$ is relatively low due to the following reasons:

- The cylinder volumetric efficiency remains near 0.3 due to an inlet diameter of 6 mm.
- Exergy is destructed due to heat generated because of friction and irreversibility. Also, air leakage was taken into account in the GT-Suite model developed for the experimental system.
- Since the heat exchanger is always connected to the system, a significant portion of the heat is extracted. For practice, only the excessive heat should be extracted using the flow control system to maintain a mass-averaged air temperature of 150°C at the HP tank inlet.

AM mode

For the AM mode, the simulation parameters are listed in Table 6.8. Compared to the AC mode, the AM simulation is only run for 3 mins, which is reasonable since the expansion phase duration for a standard ACAES system is 2 to 5 times shorter than that of the compression phase.

Table 6.8: Simulation parameters

Parameter	Value
Engine speed	60 RPM
Number of cylinder(s)	1
HP tank volume	30 L
Initial air pressure	276.94 psi,a
Initial air temperature	137.27°C
Air intake diameter	6 mm
Water initial temperature	37.5 °C
AM duration	3 mins

Similarly, the HP tank pressure, and the cranktrain indicated power are shown in Figure 6.17 and 6.18. Air pressure and indicated power drop as a function of time. The final pressure is ∼50 [psi,a], and the final indicated power is ∼70 W.

The engine brake power is calculated and numerically integrated. The AM mode energy and efficiency calculation are included in Table 6.9. From Table 6.9, the AM mode efficiency, $\eta_{Ex\_to\_Elect}$, is 17.84% which is lower than the ∼30 reported in Fazeli's experimental results [1]. This is expected since Fazeli' intake valve size was 40 mm and he used solenoid valve to further reduced the air leakage issue. The overall efficiency of 4.04% is very low but it is near the 5.0% obtained from Fazeli's simulation results using a V8 engine with combustion turned off. $\eta_{Ex\_to\_Elect}$ is relatively low due to the following reasons:

- Due to the air leakage modeled between the rotary valve and cylinder head, the air motor efficiency is lower than its actual value.
- Heat exchanger under AM mode is taking energy out from high-temperature air initially, as mentioned in Section 6.4.2.
- When the piston rises from BDC to TDC, the trapped air undergoes a compression process causing the instantaneous brake torque dropping below zero. This reduces the average brake torque.

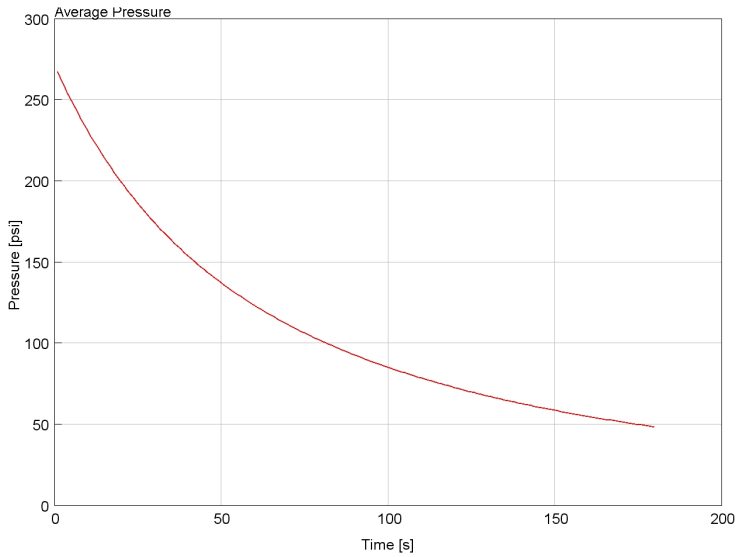

Figure 6.17: AM mode HP tank pressure vs time (baseline system)

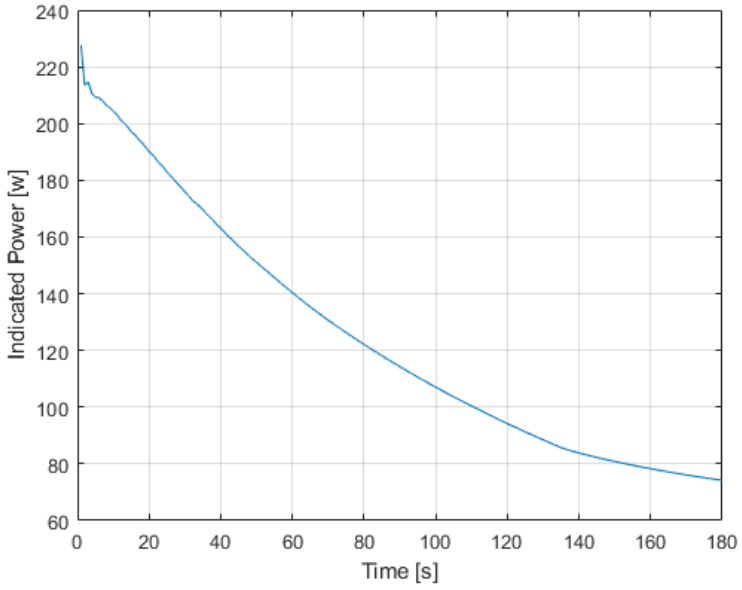

Figure 6.18: AM mode indicated power vs time (baseline system)

Table 6.9: AM efficiency calculation

AM mode Initial HP tank exergy:	131.14 KJ
Energy generated under AM mode:	22.24 KJ
AC efficiency:	22.60 %
AM efficiency:	17.84 %
Overall efficiency:	4.04 %

Despite the relatively low efficiency, the TES system designed guarantees a cylinder inlet air temperature of 33°C and prevents freezing that could damage the rotary valve and end seals. The cylinder temperature within the last crankshaft revolution is shown in Figure 6.19. As can be seen, the minimum air temperature is still above the room temperature.

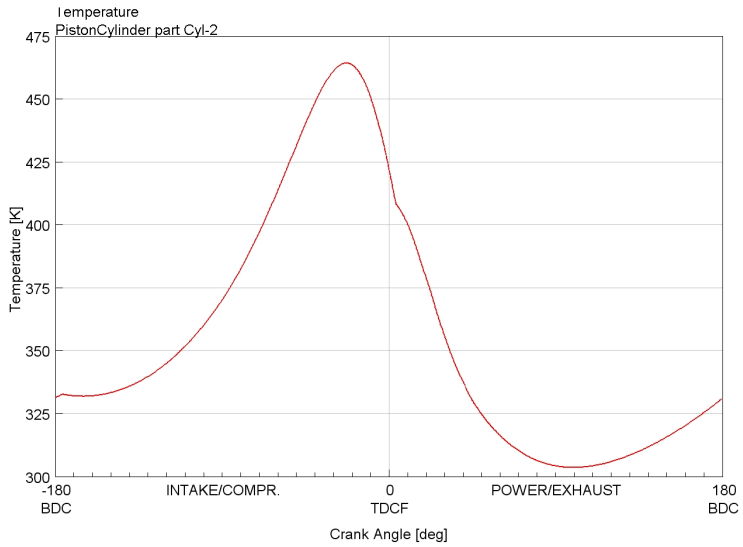

Figure 6.19: Cylinder temperature within the last crankshaft revolution

6.5.3 Optimized System

AC mode

The optimized system parameters are listed in Table 6.10. The HP tank size and air intake diameter are increased.

Table 6.10: Simulation parameters

Engine speed	500 RPM
HP tank volume	100 L
LP tank volume	0.5 L
Compression raito	8.5
Air intake diameter	10 mm
AC duration	10 mins

The valve timing mentioned in Section 6.2.4 is implemented. HP tank pressure and crank train brake power are shown in Figure 6.20. The engine brake power is negative

since the energy is supplied to the crank train to compress the air. The system efficiency is calculated in Table 6.11

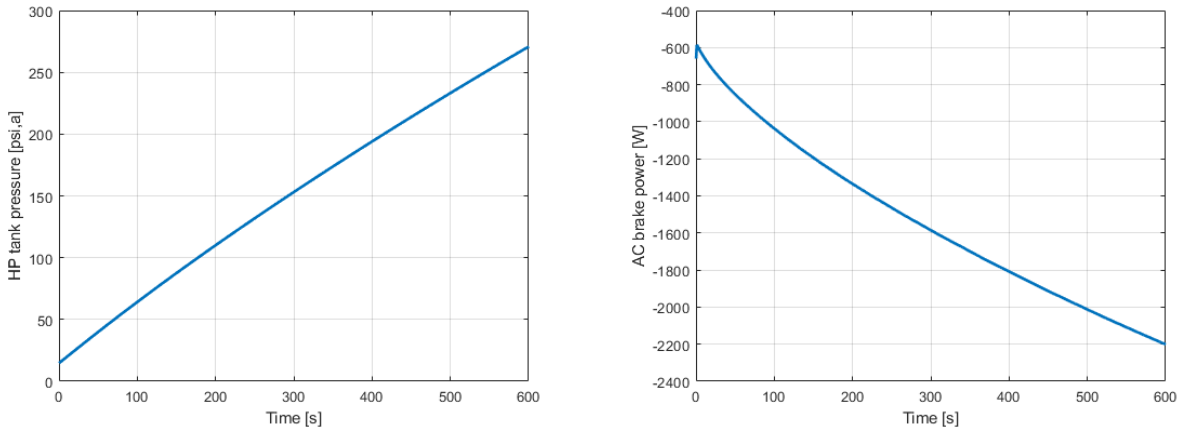

(a) HP tank pressure (b) Cranktrain brake power

Figure 6.20: (a) HP tank pressure (b) Cranktrain brake power

Table 6.11: AC efficiency calculation

Total energy input under AC mode :	922.75 KJ
Final air pressure	270.71 psi,a
Total exergy change:	433.58 KJ
AC efficiency:	46.99 %

AM mode

For the optimized system under AM mode, the optimized valve timing developed in Section 6.3.2 is implemented. The system parameters are listed in Table 6.12.

Table 6.12: Simulation parameters

Engine speed	60 RPM
HP tank volume	100 L
Initial air pressure	270.71 psi,a
Initial air temperature	394.21 K
Air intake diameter	10 mm
Water initial temperature	100 °C
AM duration	3 mins

HP tank pressure and engine brake power are shown in Figure 6.21. The system efficiency calculations are summarized in Table 6.13.

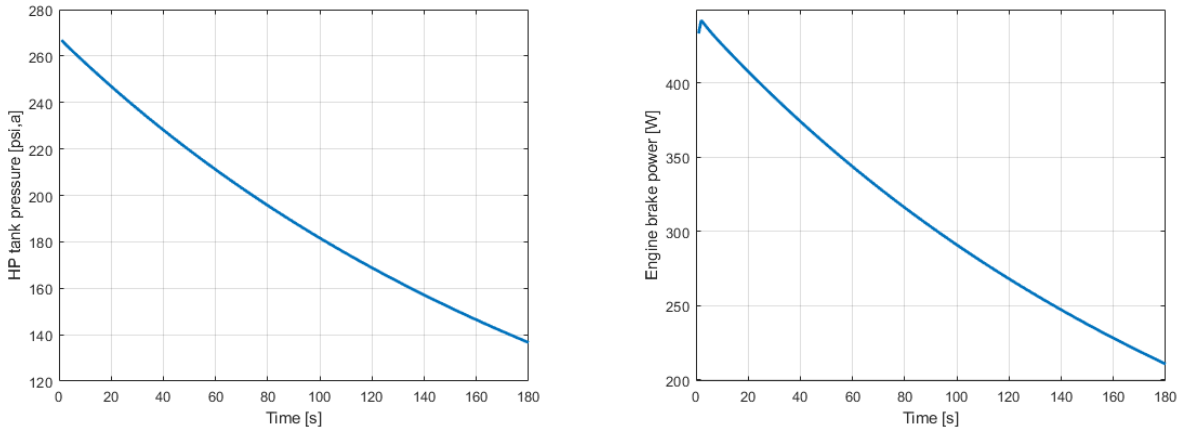

(a) HP tank pressure

(b) Cranktrain brake power

Figure 6.21: Optimized AM mode (a) HP tank pressure (b) Cranktrain brake power

Table 6.13: AM efficiency calculation and comparison

Parameter	Optimized system
AM final air pressure	136.62 psi,a
AM mode HP tank exergy change:	239.33 KJ
Energy generated under AM mode:	55.59 KJ
AC efficiency:	46.99 %
AM efficiency:	23.23 %
Overall efficiency:	10.91 %

6.5.4 Discussion

By comparing the optimized system to the baseline system in Table 6.9, the overall system energy to energy efficiency nearly tripled from ∼4% to ∼11%. AC efficiency improved by 108% from 22.60 % to 46.99 %, which is mostly because of the larger HP tank size, higher cylinder compression ratio, optimized valve timing, and larger intake. The TES system keeps the HP tank temperature around 120°C, as shown in Figure 6.22.

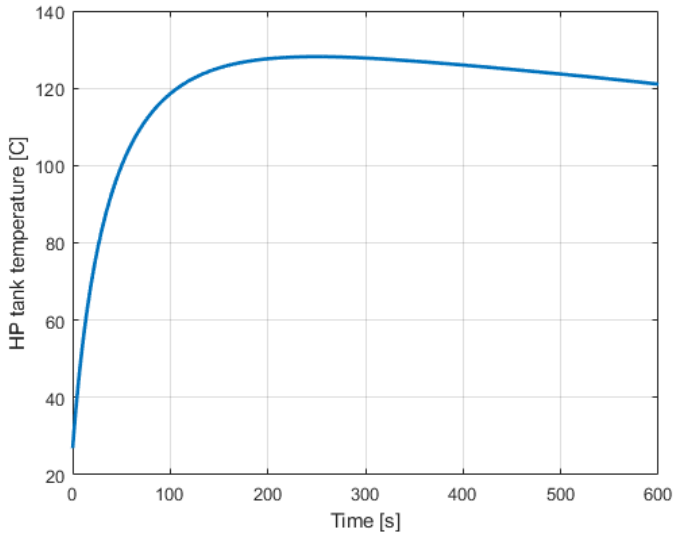

Figure 6.22: HP tank temperature [°C] vs Time [s]

Despite the improved efficiency, for the optimized system, a significant portion of the total exergy is destructed due to the following factors:

- Friction loss due to pipes, valves, orifices
- LP tank heat generation
- Cylinder, heat exchanger, and HP tank heat transfer

For the exergy destruction due to friction loss, additional cylinder(s) can be added in parallel with a larger intake, allowing more consistent airflow into the HP tank. To compensate for the space needed for a larger intake and preserve the rotary valve concept, a V-shape cylinder head with two rotary valves can be used. This cylinder head design allows the ports to have direct access to the cylinder, which further improves the cylinder volumetric efficiency.

For the LP tank heat generation, an intercooler (IC) can be added between the CY to LP valve and LP tank inlet, which extracts heat from LP tank inlet air to reduce exergy destruction. The IC can be connected to or separated from the TES system depending on the LP tank inlet air temperature. For exergy destruction due to cylinder and heat exchanger heat transfer, the compression ratio can be reduced to 5 such that the outlet air temperature is close to the designed storage temperature. Lastly, the heat exchanger can be insulated to reduce convective heat transfer with the environment.

AM mode

The AM efficiency improved by 30.20% from 17.84% to 23.23%. As mentioned in Section 6.3.2, the optimized valve timing improves the steady-state brake power by 13.38%. One possible reason for the low AM mode efficiency is the low engine rotational speed, which reduces the average crank train brake power. After running multiple simulations with different engine speeds and AM mode durations, the AM efficiencies are summarized in Table 6.14.

Table 6.14: AM mode efficiencies comparison with different engine speeds and AM mode durations

Case	Engine RPM	Efficiency (60s)	Efficiency (120s)	Efficiency (180s)
1	60	22.50 %	23.08 %	23.23 %
2	100	23.65 %	24.51 %	25.11 %
3	200	26.08 %	27.08 %	-
4	300	27.79 %	-	-
5	400	28.78 %	-	-
6	500	30.38 %	-	-

At an engine speed of 500 RPM, the system AM mode efficiency improved from 23.23% to 30.38%, which increases the round trip efficiency from 10.91% to 14.27%. This shows that engine speed is an important factor in AM mode efficiency. However, at higher engine speeds (>750 RPM), the HP tank pressure and temperature drop too fast, reducing the engine brake power with current system parameters.

Another possible reason for the low AM mode efficiency is the small HP tank size. With constant inlet temperature, pressure, and expansion ratio, the system under AM mode can be modeled as an open system. The steady-state exergy flow is shown in Figure 6.23.

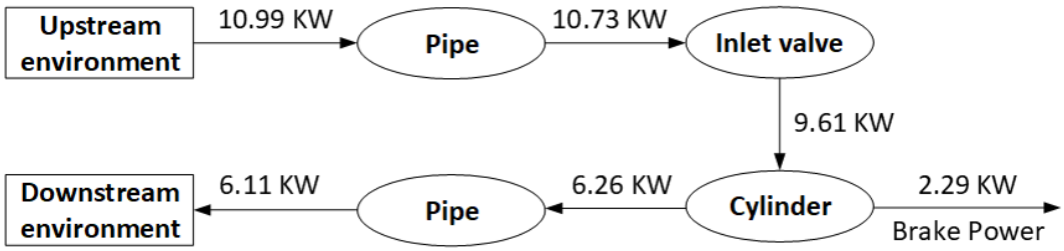

Figure 6.23: Open system steady-state exergy flow

The inlet pipe friction and heat transfer reduce the exergy flow rate from 10.99 KW to 10.73 KW. The inlet valve reduces the exergy flow rate by 1.12 KW. This is because the inlet valve only opens 180° per crankshaft revolution, which causes the average throat pressure and temperature to be lower than those of the upstream environment. For the cylinder, the difference between the exergy inlet and outlet flow rates is 3.35 KW, and the brake power generated is 2.29 KW. When only considering the cylinder exergy input and output, an exergy efficiency of 68.36% could be reached, which is close to the exergy efficiency of a turbine . When considering the losses due to the pipes and inlet valve, the AM mode overall efficiency is 46.93%. It should be noticed that the system outlet air still has an exergy flow rate of 6.11 KW, meaning that additional power can be generated. This can be accomplished by adding an extra cylinder connected in series or mixing the outlet air with inlet air using an injector [39].

Compared to a turbine, the system's low efficiency under AM mode is due to the following reasons:

- Turbine's inlet mass flow rate is independent of the crankshaft angle. For a piston-type expander, the air inlet mass flow rate is greater than zero only if the intake valve opens.

- When the piston goes from BDC to TDC, crank train instantaneous brake power drops below zero, which reduces the average brake power in a single crankshaft revolution.
- HP tank pressure drops during the expansion process. Thus, engine mass flow rate and inlet air pressure drop, reducing the average engine brake power.

From Figure 6.20 and 6.21, it is observed that the maximum brake power during the AC and AM mode is 2200 W and 430 W, respectively. Further simulation results indicate that the maximum brake power during the AM mode could reach 4KW. For the system under AM mode, when the tank pressure/temperature are low, the power produced by the air expander is mainly used to overcome the cranktrain friction. If the system is run at much higher power, higher efficiency could be expected since the effect of the cranktrain friction becomes less significant. For the AC mode, higher input power leads to higher engine RPM and higher air mass flow rate. With an optimized TES system, higher efficiency and shorter system star-up time could be expected.

6.6 Summary

In this chapter, the ACAES system under AC mode and AM mode is analyzed and optimized. The TES system performance is evaluated under both modes. The GA was used to optimize the AM mode valve timing, and the steady-state simulation showed a 13.38% improvement of engine brake power. The baseline system was simulated and compared with the optimized system in Section 6.5.3. The AC mode efficiency of the optimized system improved by 108%, and the AM mode efficiency improved by 70.3%.

Chapter 7

Conclusions and Future Work

7.1 Conclusions

The new ACAES system concept and layout were introduced, and the mathematical models were developed for the AC and AM mode. Model evaluation was conducted for different modes and the models were proved to be accurate and reliable compared with those in GT-Suite.

The experimental system with the rotary valve and the cylinder head design was modeled in GT-Suite. Specifically, a CFD analysis in ANSYS Fluent was conducted to convert the rotary valve into an equivalent model. The experimental result collected using the dSPACE system validated that the GT-Suite models can be used for further analysis and optimization. In addition, the final HP tank pressure under AC mode was able to reach 180 [psi,a], which is a 28.85% improvement compared to the previous experimental result.

The TES system, which consists of the water jacket, cylinder head embedded coolant channels and heat exchanger, was introduced. Water was selected as the heat transfer medium, and the vaporization prevention was achieved by pressurizing the water and adding nitrogen gas into the flow circuit. The TES system and CAS device were modeled in GT-Suite and MATLAB/Simulink. Simulation results showed that the designed TES system was able to maintain an air storage temperature of 150°C.

An MVM was derived to predict the AM mode brake power and validated using simulation results. A PID controller combined with a lookup table was used to regulate the AM mode engine brake power. The simulation results showed that the controller tracked a desired brake power signal accurately with a maximum percent error of 0.17%. By com-

bining the mathematical models with the TES system model and MVM, a lumped model was developed to estimate the ACAES system's behavior and reduce the simulation time.

The baseline ACAES system under AC and AM mode were analyzed and optimized. The effect of the compression ratio on the AC mode efficiency was studied. It was shown that a higher compression ratio led to higher AC mode efficiency. However, due to the constraint on the compressor outlet temperature, the compression ratio was designed to be 8.5 to prevent significant exergy destruction. GA optimization was developed considering all the constraints to identify the optimal rotary valve timing for improving the steady-state engine brake power under AM mode at constant engine speed. With the optimized valve timing, it was observed that the engine brake torque enhanced by 13.38%.

A comparison study of the baseline ACAES system and the optimized system showed that the AC and AM mode efficiency improved by 108% and 70.3%, respectively. The round-trip efficiency was nearly tripled from 4% to 11%. Further analysis showed that the low round-trip efficiency was due to the slow engine speed and the small HP tank size. Increasing the engine speed to 500 RPM further improved the system round-trip efficiency to 14.3%. The HP tank pressure and temperature under AM mode decreased too fast at higher engine speed, reducing the round-trip efficiency under current simulation parameters.

An exergy flow analysis assuming constant inlet temperature and pressure was conducted for the system under AM mode. It showed that the system can reach an AM mode efficiency of 68.36%, and additional power can be generated. Despite the relatively low round-trip efficiency, simulation results demonstrated that the system was capable of storing the energy and regenerating it later when needed. A higher efficiency could be expected if the proposed ACAES system is further studied and optimized.

7.2 Recommendations/Future Work

Mode Switching

Currently, the mode switching is done manually, which could lead to a safety problem. The mode switching can be achieved using some motorized ball valves.

Air leakage and sealing

Through this project, air leakage remains a challenging problem. With the current end seals, air is still leaking slowly, as shown in Figure 7.1. To reduce this leakage, rod-sealing

wiper seals can be added. Double-acting O-Ring seals (such as TG3100200-T40N) can be used to reduce the damage caused by the V-shape spring to the rotary valve and cylinder head.

Gasket (similar to the cylinder head gasket) can be used to replace the rubber end seals in order to compensate for the high air temperature during the compression process.

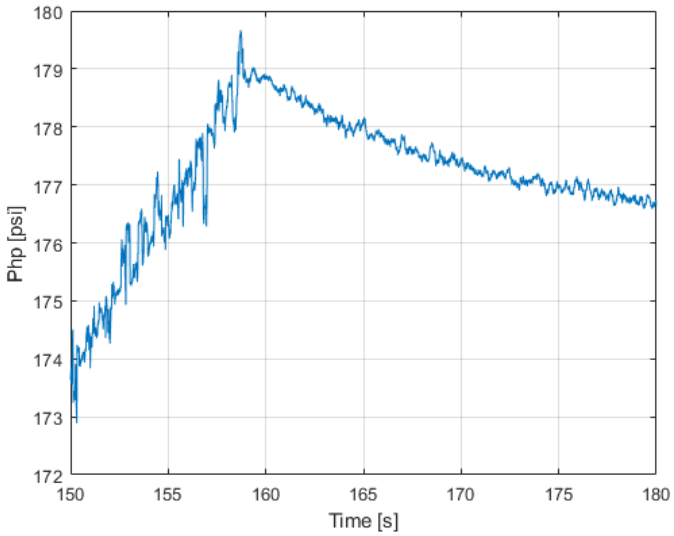

Figure 7.1: Minor air leakage after the compression stops at t=158.3 [s]

Rotary valve and cylinder head design

The current intake valve/port diameter is 6 mm. To obtain a higher volumentric efficiency at higher engine RPM, a V-shape cylinder head can be designed with dual rotary valves. For the rotary valve design, four ports can be isolated from each other and sealed independently. The major advantage of this design (see Appendix D) is that each port on the cylinder head can have direct access to the cylinder.

TES system design

The current TES system design worked well based on simulation results and achieved an HP tank average temperature of 120°C. The final air storage temperature can be improved by actively controlling the heat exchanger circuit or disconnecting the heat exchanger (airside) from the airflow path.

Valve timing

For the system under AC mode, the rotary valve opening angles are optimized under constant rotational speed. The closing angles are assumed to be 180° after the valve opens. Optimizing all valve opening/closing angles can potentially further improve AC mode efficiency.

For the AM mode, the optimized valve timing was able to improve the steady-state brake torque/power by 13.84%. Since the intake valve closing angle and exhaust valve opening angle are near the constraints imposed, GA optimization should be repeated with valve opening/closing constraints set to 130° to 230°.

AC efficiency

An intercooler can be added before the LP tank inlet, which can extract heat from inlet air and reduce the compressor discharge temperature. Additionally, the heat exchanger should be insulated to reduce convective heat transfer with the environment.

AM efficiency

The AM mode efficiency can be improved by running the expansion process at higher engine RPM. Also, larger HP tank size and higher initial pressure allow the system to operate at higher AM mode efficiency. To utilize the outlet air exergy flow rate, an extra cylinder can be connected to the system in series.

References

[1] A. Fazeli, *Development of a novel air hybrid engine*. PhD thesis, 2011.

[2] M. Budt, D. Wolf, R. Span, and J. Yan, "A review on compressed air energy storage: Basic principles, past milestones and recent developments," *Applied Energy*, vol. 170, pp. 250–268, 2016.

[3] G. Grazzini and A. Milazzo, "Exergy analysis of a caes with thermal energy storage," *Università di Firenze, Italy*, 2008.

[4] A. Fazeli, M. Zeinali, and A. Khajepour, "Application of adaptive sliding mode control for regenerative braking torque control," *IEEE/ASME Transactions On Mechatronics*, vol. 17, no. 4, pp. 745–755, 2011.

[5] M. Pournazeri, *Development of a new fully flexible hydraulic variable valve actuation system*. PhD thesis, 2012.

[6] M. Chermesnok, "Hydraulic variable valve timing testing and validation," Master's thesis, University of Waterloo, 2016.

[7] J. B. Heywood, *Internal combustion engine fundamentals*. New York, 1988.

[8] D. Liu, J. Guo, Y. Huang, and W. Wang, "An active power control strategy for wind farm based on predictions of wind turbine's maximum generation capacity," *Journal of Renewable and Sustainable Energy*, vol. 5, no. 1, p. 013121, 2013.

[9] H. Chen, T. N. Cong, W. Yang, C. Tan, Y. Li, and Y. Ding, "Progress in electrical energy storage system: A critical review," *Progress in natural science*, vol. 19, no. 3, pp. 291–312, 2009.

[10] A. Cavallo, "Controllable and affordable utility-scale electricity from intermittent wind resources and compressed air energy storage (caes)," *Energy*, vol. 32, no. 2, pp. 120–127, 2007.

[11] T. Bourgeois, F. Ammouri, M. Weber, and C. Knapik, "Evaluating the temperature inside a tank during a filling with highly-pressurized gas," *International Journal of Hydrogen Energy*, vol. 40, no. 35, pp. 11748–11755, 2015.

[12] H. Lund, G. Salgi, B. Elmegaard, and A. N. Andersen, "Optimal operation strategies of compressed air energy storage (caes) on electricity spot markets with fluctuating prices," *Applied thermal engineering*, vol. 29, no. 5-6, pp. 799–806, 2009.

[13] F. S. Barnes and J. G. Levine, *Large energy storage systems handbook*. CRC press, 2011.

[14] Y. S. Najjar and M. S. Zaamout, "Performance analysis of compressed air energy storage (caes) plant for dry regions," *Energy conversion and management*, vol. 39, no. 15, pp. 1503–1511, 1998.

[15] F. Crotogino, K.-U. Mohmeyer, and R. Scharf, "Huntorf caes: More than 20 years of successful operation," in *SMRI Spring Meeting*, vol. 2001, 2001.

[16] S. Succar, R. H. Williams, *et al.*, "Compressed air energy storage: theory, resources, and applications for wind power," *Princeton environmental institute report*, vol. 8, p. 81, 2008.

[17] H. Lund and G. Salgi, "The role of compressed air energy storage (caes) in future sustainable energy systems," *Energy conversion and management*, vol. 50, no. 5, pp. 1172–1179, 2009.

[18] G. Grazzini and A. Milazzo, "Thermodynamic analysis of caes/tes systems for renewable energy plants," *Renewable energy*, vol. 33, no. 9, pp. 1998–2006, 2008.

[19] J. Wang, L. Ma, K. Lu, S. Miao, D. Wang, and J. Wang, "Current research and development trend of compressed air energy storage," *Systems Science & Control Engineering*, vol. 5, no. 1, pp. 434–448, 2017.

[20] C. Qin and E. Loth, "Liquid piston compression efficiency with droplet heat transfer," *Applied Energy*, vol. 114, pp. 539–550, 2014.

[21] S. Lemofouet-Gatsi, "Investigation and optimisation of hybrid electricity storage systems based on compressed air and supercapacitors," tech. rep., EPFL, 2006.

[22] B. Bollinger, "Demonstration of isothermal compressed air energy storage to support renewable energy production," 1 2015.

[23] V. De Biasi, "Fundamental analyses to optimize adiabatic caes plant efficiencies," *Gas Turbine World*, vol. 39, no. 5, pp. 26–28, 2009.

[24] D. Wolf, *Methods for design and application of adiabatic compressed air energy: storage based on dynamic modeling*. Laufen Oberhausen, 2011.

[25] S. Mei, J. Wang, F. Tian, L. Chen, X. Xue, Q. Lu, Y. Zhou, and X. Zhou, "Design and engineering implementation of non-supplementary fired compressed air energy storage system: Ticc-500," *Science China Technological Sciences*, vol. 58, no. 4, pp. 600–611, 2015.

[26] J. Xiang and C. Ning, "Ticc-500 energy storage phase of modeling and thermal properties," *Energy Storage Science and Technology*, vol. 6, no. 1, p. 135, 2017.

[27] D. Wolf and M. Budt, "Lta-caes–a low-temperature approach to adiabatic compressed air energy storage," *Applied Energy*, vol. 125, pp. 158–164, 2014.

[28] A. Gil, M. Medrano, I. Martorell, A. Lázaro, P. Dolado, B. Zalba, and L. F. Cabeza, "State of the art on high temperature thermal energy storage for power generation. part 1—concepts, materials and modellization," *Renewable and Sustainable Energy Reviews*, vol. 14, no. 1, pp. 31–55, 2010.

[29] M. Medrano, A. Gil, I. Martorell, X. Potau, and L. F. Cabeza, "State of the art on high-temperature thermal energy storage for power generation. part 2—case studies," *Renewable and Sustainable Energy Reviews*, vol. 14, no. 1, pp. 56–72, 2010.

[30] L. Szablowski, P. Krawczyk, K. Badyda, S. Karellas, E. Kakaras, and W. Bujalski, "Energy and exergy analysis of adiabatic compressed air energy storage system," *Energy*, vol. 138, pp. 12–18, 2017.

[31] N. Hartmann, O. Vöhringer, C. Kruck, and L. Eltrop, "Simulation and analysis of different adiabatic compressed air energy storage plant configurations," *Applied Energy*, vol. 93, pp. 541–548, 2012.

[32] E. Jannelli, M. Minutillo, A. L. Lavadera, and G. Falcucci, "A small-scale caes (compressed air energy storage) system for stand-alone renewable energy power plant for a radio base station: A sizing-design methodology," *Energy*, vol. 78, pp. 313–322, 2014.

[33] G. Grazzini and A. Milazzo, "A thermodynamic analysis of multistage adiabatic caes," *Proceedings of the IEEE*, vol. 100, no. 2, pp. 461–472, 2011.

[34] E. Barbour, D. Mignard, Y. Ding, and Y. Li, "Adiabatic compressed air energy storage with packed bed thermal energy storage," *Applied energy*, vol. 155, pp. 804–815, 2015.

[35] H. Mozayeni, M. Negnevitsky, X. Wang, F. Cao, and X. Peng, "Performance study of an advanced adiabatic compressed air energy storage system," *Energy Procedia*, vol. 110, pp. 71–76, 2017.

[36] S. W. Freund, M. Finkenrath, C. Botero, C. S. Belloni, M. A. G. Salazar, and S. M.-N. Hoffmann, "Adiabatic compressed air energy storage system with liquid thermal energy storage," May 5 2011. US Patent App. 12/609,449.

[37] K. E. Stahlkopf, S. E. Crane, E. P. Berlin Jr, A. P. ABKENAR, *et al.*, "Compressed air energy storage system utilizing two-phase flow to facilitate heat exchange," May 7 2013. US Patent 8,436,489.

[38] A. Bannari, "Compressed air energy storage and recovery," Jan. 3 2019. US Patent App. 15/911,830.

[39] Z. Guo, G. Deng, Y. Fan, and G. Chen, "Performance optimization of adiabatic compressed air energy storage with ejector technology," *Applied Thermal Engineering*, vol. 94, pp. 193–197, 2016.

[40] M. M. Schechter and M. B. Levin, "Camless engine," tech. rep., SAE Technical Paper, 1996.

[41] M. M. Schechter, "New cycles for automobile engines," tech. rep., SAE Technical Paper, 1999.

[42] M. Andersson, B. Johansson, and A. Hultqvist, "An air hybrid for high power absorption and discharge," tech. rep., SAE Technical Paper, 2005.

[43] C.-M. Liu, J.-J. You, C.-K. Sung, and C.-Y. Huang, "Modified intake and exhaust system for piston-type compressed air engines," *Energy*, vol. 90, pp. 516–524, 2015.

[44] Y.-H. Hung, Y.-M. Tung, and H.-W. Li, "A real-time model of an automotive air propulsion system," *Applied energy*, vol. 129, pp. 287–298, 2014.

[45] Q. Xu, M. Cai, and Y. Shi, "Dynamic heat transfer model for temperature drop analysis and heat exchange system design of the air-powered engine system," *Energy*, vol. 68, pp. 877–885, 2014.

[46] Y.-T. Shen and Y.-R. Hwang, "Design and implementation of an air-powered motorcycles," *Applied Energy*, vol. 86, no. 7-8, pp. 1105–1110, 2009.

[47] C. J. Sancken and P. Y. Li, "Optimal efficiency-power relationship for an air motor-compressor in an energy storage and regeneration system," in *ASME 2009 Dynamic Systems and Control Conference*, pp. 403–410, American Society of Mechanical Engineers Digital Collection, 2009.

[48] A. T. Rice and P. Y. Li, "Optimal efficiency-power tradeoff for an air motor/compressor with volume varying heat transfer capability," in *ASME 2011 Dynamic Systems and Control Conference and Bath/ASME Symposium on Fluid Power and Motion Control*, pp. 145–152, American Society of Mechanical Engineers Digital Collection, 2012.

[49] M. Terpstra, "Hydraulic variable valve actuation system: Development & validation," Master's thesis, University of Waterloo, 2019.

[50] J. Heywood, *Internal Combustion Engine Fundamentals 2E*. McGraw-Hill Education, 2018.

[51] A. Fazeli, A. Khajepour, and C. Devaud, "A novel compression strategy for air hybrid engines," *Applied energy*, vol. 88, no. 9, pp. 2955–2966, 2011.

[52] M. Zhu and X. Wang, "An integral type μ synthesis method for temperature and pressure control of flight environment simulation volume," in *Turbo Expo: Power for Land, Sea, and Air*, vol. 50916, p. V006T05A006, American Society of Mechanical Engineers, 2017.

[53] M. Elhaj, F. Gu, A. Ball, A. Albarbar, M. Al-Qattan, and A. Naid, "Numerical simulation and experimental study of a two-stage reciprocating compressor for condition monitoring," *Mechanical Systems and Signal Processing*, vol. 22, no. 2, pp. 374–389, 2008.

[54] G. Woschni, "A universally applicable equation for the instantaneous heat transfer coefficient in the internal combustion engine," tech. rep., SAE Technical paper, 1967.

[55] C. E. Brennen, "An internet book on fluid dynamics," *INDEX for INTERNET BOOK ON FLUID DYNAMICS*, 2006.

[56] T. L. Bergman, F. P. Incropera, D. P. DeWitt, and A. S. Lavine, *Fundamentals of heat and mass transfer*. John Wiley & Sons, 2011.

[57] A. Fazeli, A. Khajepour, C. Devaud, and N. L. Azad, "A new air hybrid engine using throttle control," tech. rep., SAE Technical Paper, 2009.

[58] Y. Huang, *Anti-idling systems for service vehicles with A/CR units: modeling, holistic control, and experiments*. PhD thesis, 2016.

[59] D. Whitley, "A genetic algorithm tutorial," *Statistics and computing*, vol. 4, no. 2, pp. 65–85, 1994.

[60] J. Horn, N. Nafpliotis, and D. E. Goldberg, "A niched pareto genetic algorithm for multiobjective optimization," in *Proceedings of the first IEEE conference on evolutionary computation. IEEE world congress on computational intelligence*, pp. 82–87, Ieee, 1994.

[61] Y. Li, A. Khajepour, C. Devaud, and K. Liu, "Power and fuel economy optimizations of gasoline engines using hydraulic variable valve actuation system," *Applied Energy*, vol. 206, pp. 577–593, 2017.

[62] Y. Li, *Power and Fuel Economy Optimization of Unthrottled Spark-Ignition Engines Using Highly Flexible Hydraulic Variable Valve Actuation System*. PhD thesis, 2018.

[63] Z. Meiyin, W. Xi, D. Zhihong, S. Zhang, and P. Xitong, "Two freedom linear parameter varying μ synthesis control for flight environment testbed," *Chinese Journal of Aeronautics*, vol. 32, no. 5, pp. 1204–1214, 2019.

[64] S. R. Turns and L. L. Pauley, *Thermodynamics: concepts and applications*. Cambridge University Press, 2020.

[65] E. W. Lemmon, R. T. Jacobsen, S. G. Penoncello, and D. G. Friend, "Thermodynamic properties of air and mixtures of nitrogen, argon, and oxygen from 60 to 2000 k at pressures to 2000 mpa," *Journal of physical and chemical reference data*, vol. 29, no. 3, pp. 331–385, 2000.

[66] I. H. Bell, J. Wronski, S. Quoilin, and V. Lemort, "Pure and pseudo-pure fluid thermophysical property evaluation and the open-source thermophysical property library coolprop," *Industrial & Engineering Chemistry Research*, vol. 53, no. 6, pp. 2498–2508, 2014.

APPENDICES

Appendix A

Air Properties Calculation

There methods used to calculate air properties are summarized in the sections below. Air properties calculated using three methods for air temperature ranging from 200 K to 2200 K are compared.

GT-Suite (GT)

The air properties (specific enthalpy and specific heat under constant pressure) obtained from GT-Suite air2 can be calculated using the equations in the form of:

$$h = h_{ref} + \sum_{n=1}^{5} a_n (T - T_{ref})^n \tag{A.1}$$

$$\frac{\partial h}{\partial T} = C_p = \sum_{n=1}^{5} n a_n (T - T_{ref})^{n-1} \tag{A.2}$$

Equations generated from curve fitting (Zhu)

Similarly, the air properties equations generated by curve fitting was provided by Meiyin Zhu [63]. The equations have the form of:

$$T_z = T/1000 \tag{A.3}$$

$$h = 10^6 \left[A_0 T_z + \sum_{n=1}^{8} \frac{A_n {T_z}^{n+1}}{n+1} \right] \tag{A.4}$$

$$\frac{\partial h}{\partial T} = C_p = 10^3 \left[A_0 + \sum_{n=1}^{8} A_n {T_z}^n \right] \tag{A.5}$$

Lookup Tables (book)

Lookup tables were generated using the air properties table included in the book *Thermodynamics: concepts and applications* [64]. For temperature between data points, requested h and C_p were calculated using interpolation. The three methods to calculate air properties are compared in Figure A.1 and A.2.

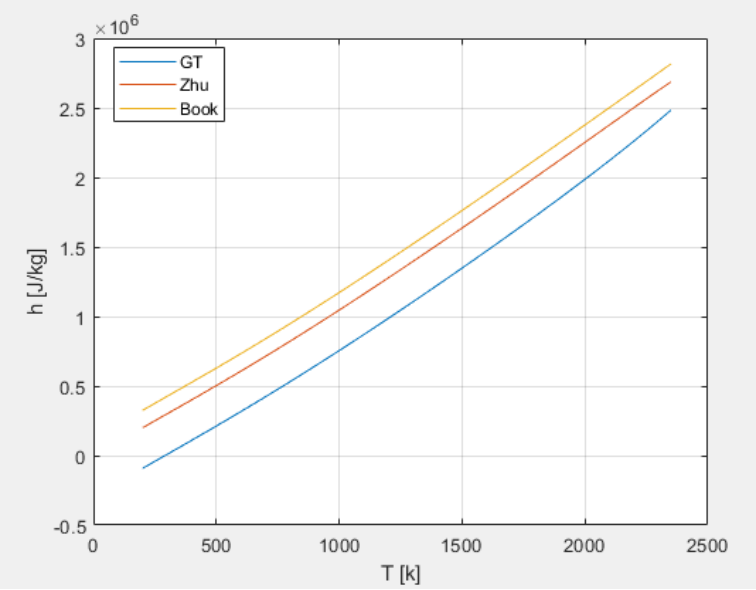

Figure A.1: h Comparison

For the specific enthalpy, h, three methods yield similar curve but the offsets are clearly different. This is expected since enthalpy and entropy are relative properties which means the differences in the enthalpy or entropy are more important than the absolute values of the enthalpy or entropy.

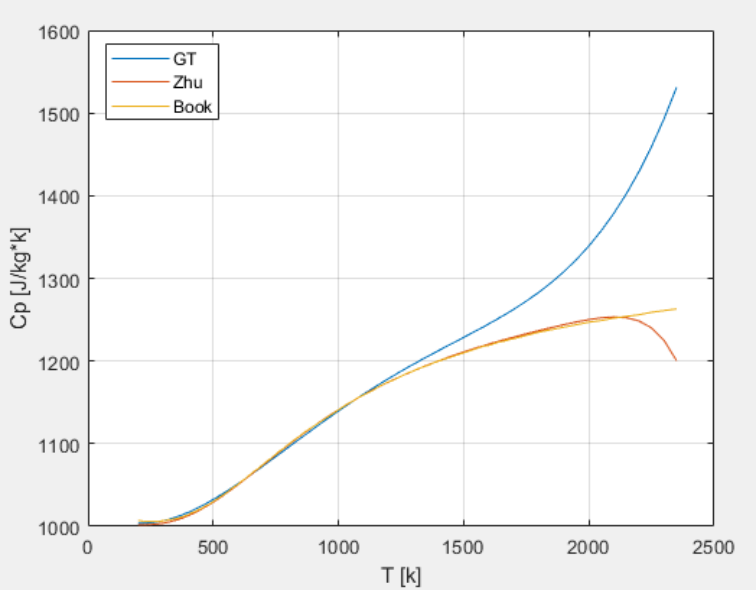

Figure A.2: C_p Comparison

For the specific heat at constant pressure, C_p, significant differences are present between the value calculated using GT method and the results from other methods when the temperature is above 1200 K. However, for this project, the differences are negligible for the ACAES system since the maximum operational temperature is far below 1000 K. After comparing three methods, the Lookup Tables (book) method was selected to calculate the air properties in this project.

In the future, air properties can be calculated by using more advanced air properties models [65] or open-source air properties calculator like CoolProp [66].

Appendix B

Engine and Rotary Valves Specifications

B.1 Engine Specifications

Bore	90 mm
Stroke	67 mm
Engine displacement	450 cc
Connecting rod length	125 mm
Valve diameter	6 mm
TDC clearnace	3 mm
HP tank volume	3 L
LP tank volume	0.5 L
Valve discharge coefficient	0.7 (only used in in the mathmatical model)
Compression ratio	8.5 (reduce to 7.2 for experimental system)

B.2 Rotary Valve Specifications

Center flow area diameter	6 mm
Center flow length (distance between the first and fourth port)	125 mm
Opening angle	90°(actual angle)
Width of the port	6 mm

Appendix C

Parts Lists

C.1 Mechanical Parts lists

Part Description	Manufacturer	Part Number
shaft diameter 20 mm seals	TRELLEBORG	TVM200200-T40SM
20mm 416 Stainless Steel Rod	Mcmaster	3821T201
Brass pipe fitting	Mcmaster	50785K611
Gasket, cylinder head	Kohler Engines	1204110-S
Ball Bearing 20x47x14	Canada Bearings	6204ZZC3-BEARING
Steel Clamp Shaft Coupling	Fastenal	0403128
High-Temperature Thread Sealant	Fastenal	0150214
1/4 NPT pipe cross	Fastenal	0464204
Pressure Gauge	Fastenal	0490545

C.2 Electrical Parts List

Part Description	Manufacturer	Part Number
Torque Transducer	HBM	T40B 500Q
Absolute pressure sensor (0-1000 psi)	Omega	PX309-1KA5V
Thermocouple	Omega	TC-K-NPT-E-72-SMP

Appendix D

Cylinder Head Design

The new V-shape cylinder head design is shown in Figure D.1. There are four ports (diameter of 10 mm) directly connected to the cylinder,increasing the cylinder volumetric efficiency at higher engine rotational speed. Two NPT-1/4" ports are designed on the top surface for sensor mounting. Four coolant channels are embedded into this design, as shown in Figure D.2 (Two channels sit directly above the cylinder while the others are used to cool the rotary valves). The valve timings are controlled by two shorter rotary valves, which the airflow from and into LP tank is separated from the intake and CY to HP valve. Compared to the current cylinder head, this design reduces the weight by roughly 50%. To further improve the sealing, high-temperature gasket maker can be applied to the cylinder gasket. For accurate gasket/cylinder head placement, locating pins can be added to the cylinder head design.

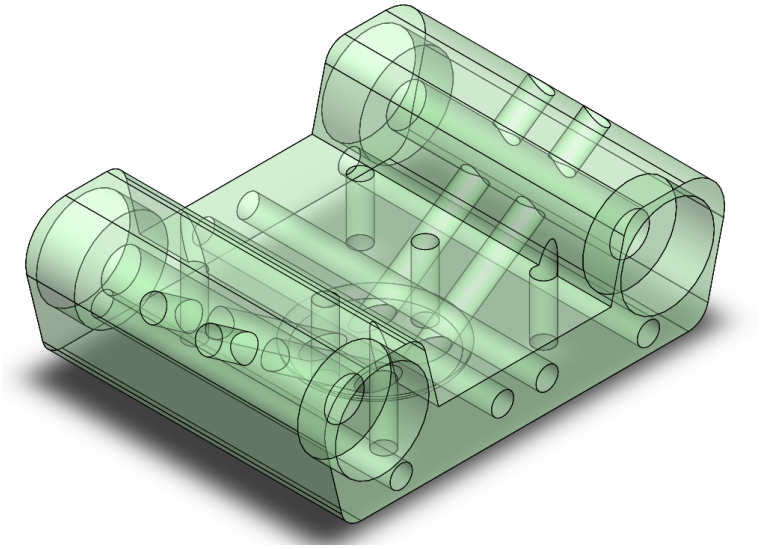

Figure D.1: New cylinder head design isometric view

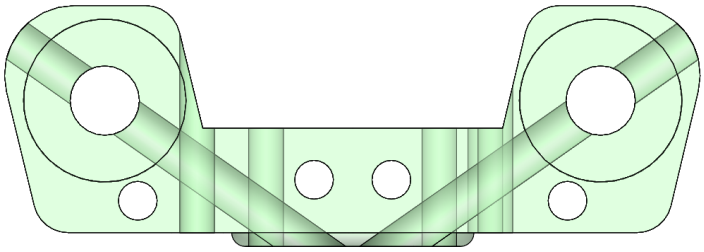

Figure D.2: Right view